CHARACTERIZING THE SEISMOTECTONICS OF THE YORBA LINDA TREND BY EARTHQUAKE RELOCATION

A Project

Presented to the

Faculty of

California State Polytechnic University, Pomona

In Partial Fulfillment

Of the Requirements for the Degree

Master of Science

In

Geological Sciences

By

Kyle P. Macy

2020

SIGNATURE PAGE

THESIS: CHARACTERIZING THE SEISMOTECTONICS OF THE YORBA LINDA TREND BY EARTHQUAKE RELOCATION

AUTHOR: Kyle P Macy

DATE SUBMITTED: 2020

Department of Geological Sciences

Dr. Jascha Polet _____

Thesis Committee Chair

Geological Sciences

Dr. Nick Van Buer _____

Geological Sciences

Dr. Stephen Osborn _____

Geological Sciences

ACKNOWLEDGEMENTS

This thesis was especially difficult for me and I would like to take some time in acknowledging the people that supported me and assist me. First and foremost I would like to thank my friends and family, particularly my mother for being my rock. She is someone who always supports any endeavor that I would set my eyes on, within reason, but never shy about providing me with some criticisms on my writing, thought process, or my behavior (something she never forgets to tell me that I have a bit of one).

I greatly appreciate all of the new friends that I have made during my time in the graduate program at Cal Poly Pomona, with great emphasis on Stacey Petrashek, Anisha Tyagi and Raul Contreras. These three always stood by my side and were willing to lend an ear to help and try to understand my frustrations and milestones. A great many thanks to my roommates: Lisa Boquist, Ulysse Holingue and Nicole Gage, who reminded me that it was okay to relax and have fun once in a while. These people were always understanding to push me when I did not want to do any work, but were always welcoming when it came time to relax and take a breather.

I would also like to give a special thank you to my advisor, Dr. Jascha Polet. She always pointed out my golden achievements, with a little reminder of my flaws. The knowledge she has provided me is nothing short of priceless. One thing that I particularly thank her for is to stand at my side, but never overextending her assistance, allowing me to push myself forward and figure things out on my own, but never being too far as to know if I'm doing something wrong (which she was never afraid to do). This allowed me to gain the knowledge of programming and seismology that I never thought I would obtain. I would also like to give out a special thank you to Rachel Hatch, for assistance in understanding the GrowClust program and give me hints and steer me in the right direction for the relocation process.

ABSTRACT

The Yorba Linda Trend is a proposed NE-SW alignment of earthquakes near the western edge of the Los Angeles Basin in southern California first described by Egill Hauksson in the early 1990s (Hauksson, 1990). Most earthquakes in this area exhibit a strike-slip mechanism, but they do not fall on or near any mapped fault traces. More recent events and earthquake sequences have occurred within the boundaries of the Yorba Linda Trend since its conception: the 2002 Yorba Linda and 2008 Chino Hills earthquakes. These two sequences may now be considered part of this trend. Both of these sequences have a northeast-southwest striking orientation. The 2014 La Habra earthquake sequence located nearby follows a parallel orientation. The largest events of each of these sequences all exhibit a strike slip or oblique mechanism. The aftershock sequences, combined with the mechanisms, suggest previously unmapped left-lateral strike-slip faults may be responsible, but their exact geometry is unclear. Bookshelf faulting within the Chino Hills, potentially produced by the tectonic movement of the Whittier Fault and the Chino Fault may provide an explanation to the origin of some of these earthquakes.

Because a majority of these earthquakes are small, they are poorly located. Seismic relocation using waveform cross-correlation allows for these small events to be relocated with a relatively high accuracy and for possible fault structures to be revealed. In this study, we utilized the GISMO cross correlation MATLAB toolbox (Thompson & Reyes, 2018) to determine correlation values and lag times of similar earthquakes in order to improve the arrival time measurements of the P- and S-waves of these earthquakes. We then entered these improved arrival times in the GrowClust relative relocation algorithm (Trugman & Shearer, 2017). In this relocation procedure, we used three 1-D velocity models: the IASP91 velocity model (Kennett & Engdahl, 1991), the smoothed southern California velocity model (Shao et al., 2012), and the Los Angeles Basin velocity model determined from the 1987 Whittier Narrows Earthquake (Hauksson et al., 2008) under a 0.2 sec RMS differential travel time residual, as well as a 0.6 sec differential travel time

residual to successfully relocate earthquakes in the region of the YLT from 1989 to 2018.

Each of the results for the six relocation attempts reveals two distinct clusters of earthquakes that are relatively planar centered around the 2008 Chino Hills Earthquake and the 2002 Yorba Linda Earthquakes. A noticeable gap is present between these two sequences. Relocation of the 2014 La Habra Sequence has aligned these earthquakes to form a northwest dipping planar structure, with many events clustered around the Coyote Hills Fault System. Other clusters of seismicity that were revealed by the GrowClust relocation show a system of earthquakes within the Los Angeles Basin just north of the Peralta Hills and El Modeno Faults, which may be anthropogenically induced by oil extraction within the Richfield Oil Field.

None of the relocation results show a clear through-going planar structure connecting the Yorba Linda and Chino Hills Sequences. In addition, we do not see any seismicity trends that imply the presence of bookshelf faulting that connect the two sequences. The Yorba Linda Sequence may be situated along a high angle fault structure to the Whittier Fault. The orientation of this fault structure in combination with the focal mechanisms is indicative of a left-lateral strike slip fault. The Chino Hills Sequence is situated along a similarly oriented fault. Relocations of the La Habra Sequence consistently reveal that these events are oriented along a northeast-southwest striking fault, beginning at the Whittier Fault and extending towards the Coyote Hills Fault System. This orientation, in combination with the focal mechanisms of this sequence, would imply the existence of a steeply dipping or near vertical left-lateral strike-slip fault.

Contents

List of Tables

List of Figures

1 Introduction

The Yorba Linda Trend (YLT) is a linear trend of earthquakes originally identified in the early 1990s by Egill Hauksson (Hauksson, 1990). This Trend (Figure 1) extends from the center of the Puente Hills in southern California towards the southeast corner of the Los Angeles Basin (Hauksson, 1990) (Figure 1). As defined by Hauksson, this trend of events is composed primarily of small to moderate sized strike-slip events. More recently two relatively large events and subsequent earthquake sequences: the 2002 Yorba Linda and 2008 Chino Hills earthquakes, may now be considered part of this trend. These two recent earthquake sequences are unusual in that they do not follow any known major fault traces, rather they trend at high angles to major faults, particularly the Whittier Fault. In order to better understand the potential presence of this proposed Trend, we will cover how the Puente Hills and surrounding faults were formed, and describe their context in terms of the major tectonics of Southern California.

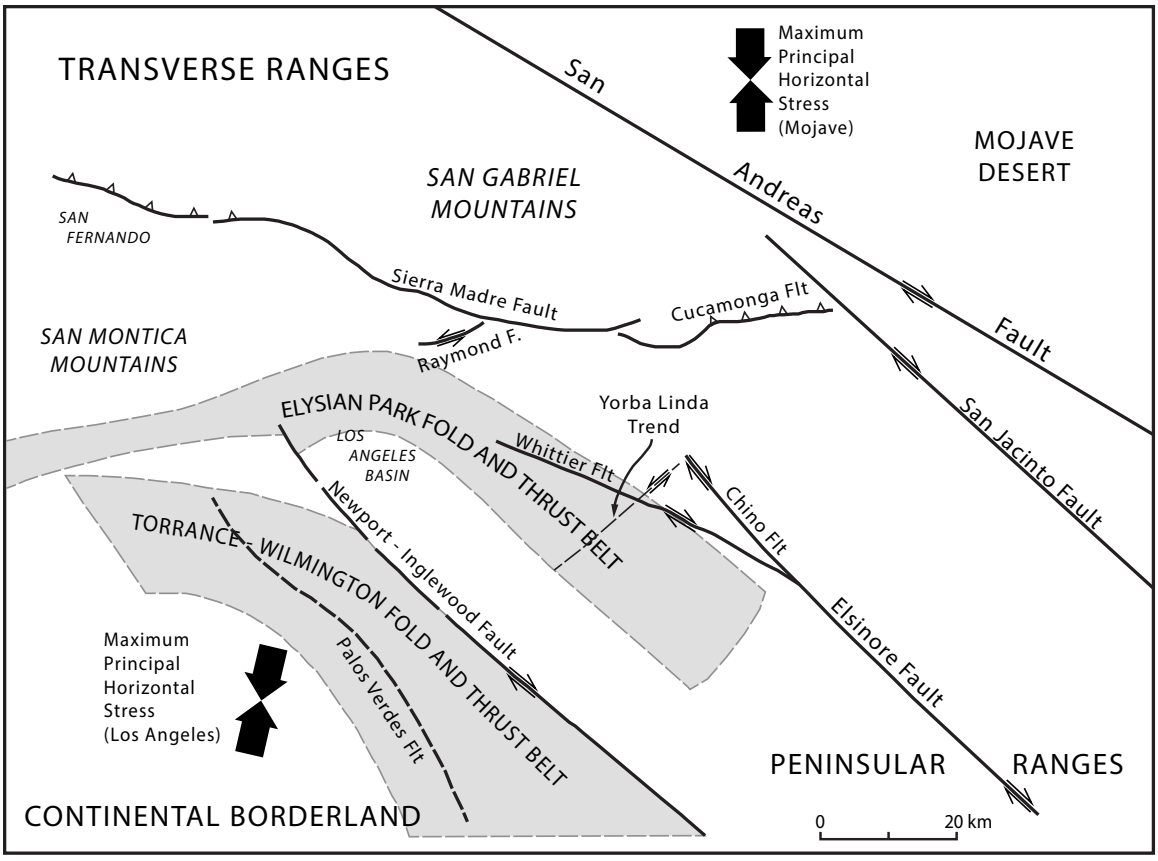

Figure 1: Simplified tectonic map of southern California. The black solid and dashed lines denote major fault traces, labeled with their name and the type of motion. The shaded gray areas indicate major thrust belts within southern California. The YLT is shown as a thin dashed line near the center of the map, beginning near the northern end of the Chino Fault and transecting the Whittier Fault. Based on its orientation, the YLT is assumed to possess a left-lateral strike-slip motion, comparable to faults that contribute to escape tectonics within southern California. The large arrows near the top right and bottom left corners of the image illustrate the principal horizontal stresses within the localized areas. Map from (Hauksson, 1990).

1.1 Tectonic Setting

Southern California's geologic/tectonic provinces were formed primarily through a period of extensive Miocene crustal extension and block rotation, Pliocene contraction and Plio-Quaternary transpression (Luyendyk et al., 1980; Luyendyk, 1991; Atwater, 1998; Bjorklund & Burke, 2002; Bjorklund et al., 2002). The "Big Bend" segment of the San Andreas Fault (SAF), which is a direct result of this mid-Miocene crustal rotation, is a primary contributor to many of the tectonic processes of southern California that formed these regimes. This is primarily due to the trace of this segment of the SAF trending in a

direction that contrasts with the principal tectonic stresses (σ_1) (Luyendyk, 1991; Walls et al., 1998) (Figure 1, Figure 2). Major geologic and tectonic regimes in this area include the Peninsular and Transverse Ranges, and the Chino and Los Angeles Basins (Figure 2). These regions are subdivided by major northwest-southeast trending right-lateral strike-slip faults such as the San Jacinto, Elsinore and Newport-Inglewood Fault Systems, whereas thrust faults, such as the Cucamonga and Sierra Madre Fault Systems are dominant along the foothills of the Transverse and San Gabriel Mountains (Walls et al., 1998; Hauksson, 1990; Yeats, 2004) (Figure 2). Portions of the San Jose and Raymond Fault Systems are left-lateral strike-slip faults with a northeast-southwest strike (Walls et al., 1998; Hauksson, 1990; Astiz et al., 2000) (Figure 2). The orientation of these left-lateral faults suggest escape tectonics contribute to the east-west extension in the area (Walls et al., 1998; Yeats, 2004).

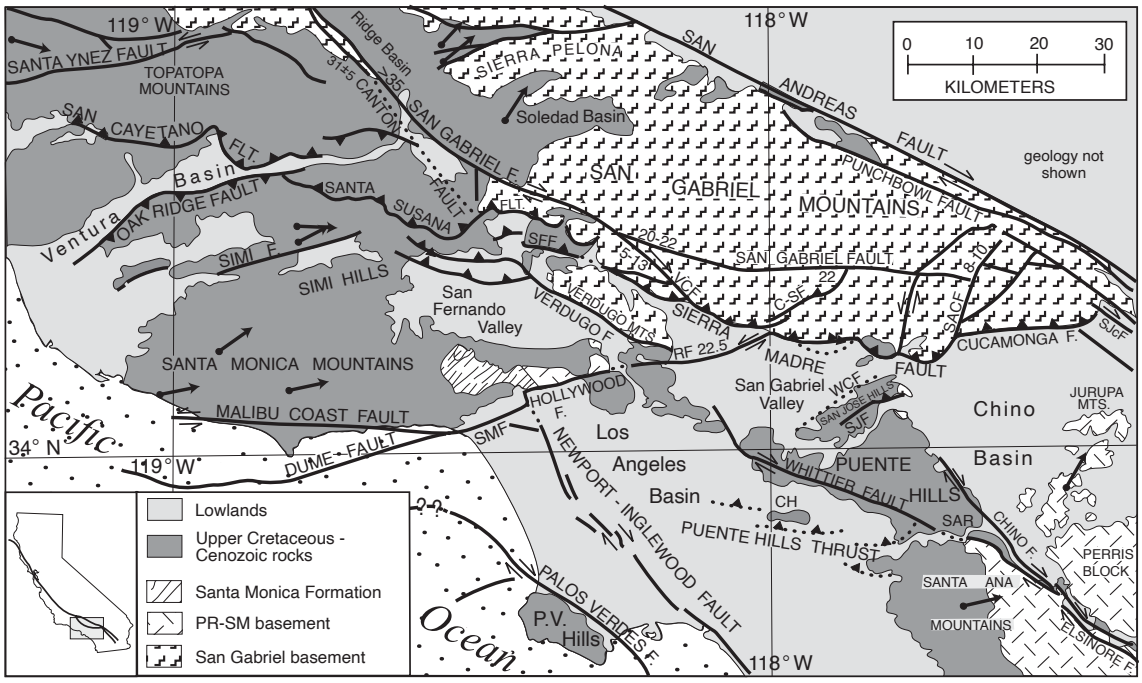

Figure 2: Overview map of the geographic and tectonic regimes of southern California. Each of the black lines represents known surface traces of major faults. Dotted lines indicate proposed fault traces, with the Puente Hills Thrust the most prominent. Arrows denote the magnetic declination of that particular area during the Miocene Epoch. Abbreviations: C-SF: Clamshell-Sawpit fault; CH: Coyote Hills fault, PV Hills: Palos Verdes Hills; RF: Raymond fault; SACF: San Antonio Canyon fault; SFF: San Fernando fault; SJF: San Jose fault; SJcF: San Jacinto fault; SMF: Santa Monica Fault; WCW: Walnut Creek fault. Image modified from (Yeats, 2004).

A closer inspection of the Puente Hills shows a complex tectonic feature bounded by the Whittier Fault system on the west, the Chino and Central Ave Faults on the east, and the San Jose and Walnut Creek Faults towards the north (Figure 3). The Puente Hills half-graben is a feature produced by Miocene extension as a result of transrotation, with the originally normal faulting Whittier Fault as the western boundary to the Puente Hills (Bjorklund & Burke, 2002; Bjorklund et al., 2002). The evolution of the Puente Hills half-graben to the Puente Hills anticline and resulting inversion of the normal Whittier Fault into an oblique motion was likely a result of changing tectonic stresses due to the San Andreas Fault formation (Bjorklund et al., 2002). Throughout the Puente Hills is a network of pre-Quaternary faults, with some extending from the Whittier and Chino Faults (Figure 3). These pre-Quaternary faults may be a result of a smaller scale tectonic block rotation within the Chino Hills.

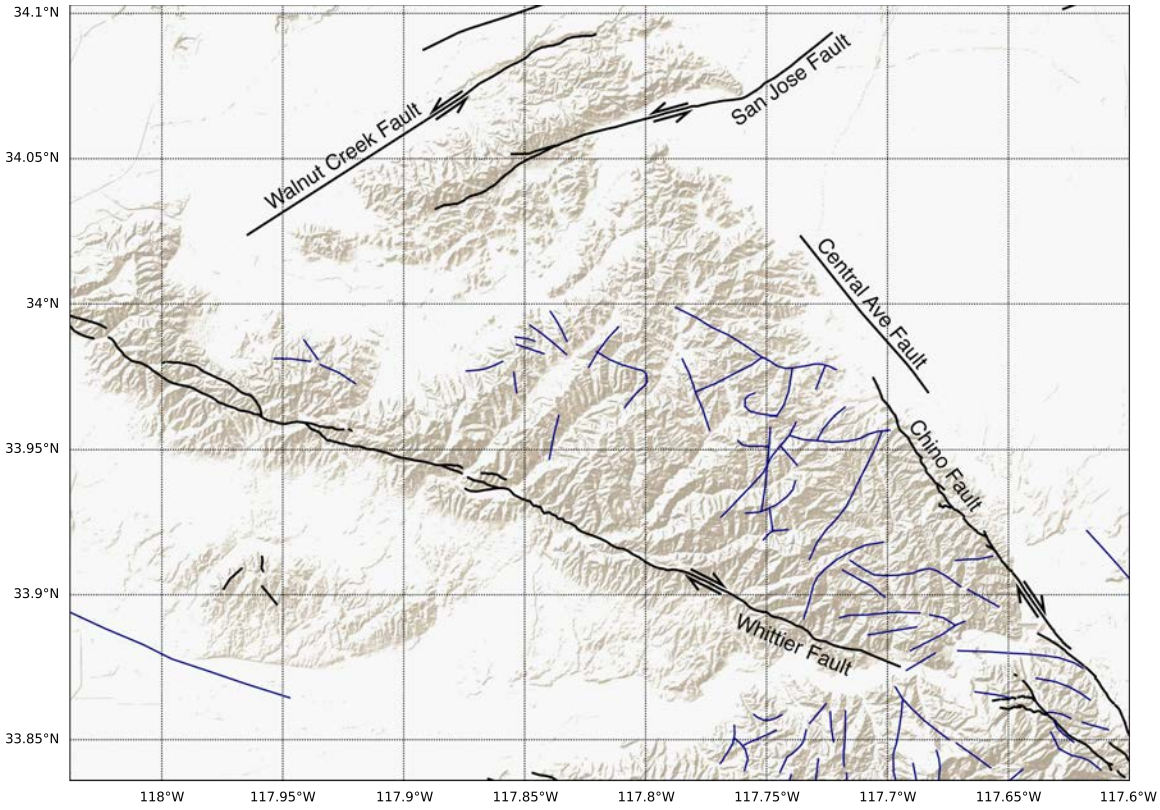

Figure 3: Shaded relief map of the Puente Hills and surrounding areas. Quaternary faults are indicated by the black lines. Pre-Quaternary lines are indicated by the blue lines. Quaternary and pre-Quaternary fault files provided by the California Geologic Survey (CGS). Major faults are labeled with their names. Each of the major faults surrounding the Puente Hills is annotated with its type of motion, with the Whittier and Chino Faults exhibiting right-lateral strike-slip motions, while the Walnut Creek and San Jose Faults have a left-lateral strike-slip motion.

Extensive block rotation has occurred throughout southern California and has caused the formation of faults between two dextral or sinstral faults. Primary examples of this include areas near the Cajon Pass between the SAF and the San Jacinto Fault (SJF) and along the southern end of the SAF near the Salton Sea, making up the Brawley Seismic Zone (Nicholson et al., 1986; Darin & Dorsey, 2013). If a large tectonic block is situated between two strike-slip faults with parallel trends, the block will experience significant stress perpendicular to that of the trends of these faults (Figure 4). As a result, these planes of failure are likely candidates of future fault traces to alleviate internal stress within these blocks (Luyendyk, 1991; Nicholson et al., 1986; Darin & Dorsey, 2013). These faults, also known as bookshelf faults or domino faults, will possess a strike slip

motion opposite to that of the major boundary faults. An example of this model is shown by a block schematic produced by Nicholson et al. (1987) in their analysis of orthogonal trends in seismicity between the SAF and the SJF (Figure 4). It has been suggested that the YLT may be a sinstral bookshelf fault trending perpendicular to the northwest-southeast trending right-lateral Whittier and Chino Faults (Hauksson, 1990) (Figure 1). A highly precise relocation of the earthquake distribution of the YLT may help determine whether this trend of earthquakes is situated on a single structural feature or along a series of bookshelf faults.

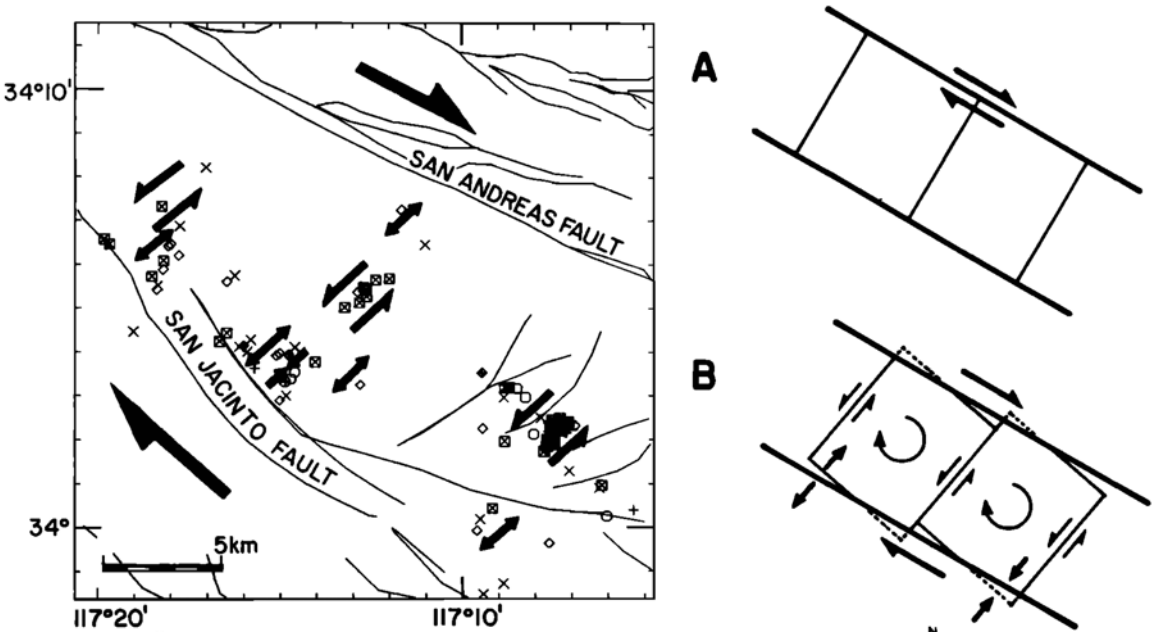

Figure 4: Schematic block model of bookshelf faulting. The example provided by Nicholson et al. (1987) details this type of faulting near the Cajon Pass between the SAF and the SJF. These faults were interpreted to exist within this area mainly due to the presence of northeast-southwest trends of earthquakes in an area that is expected to produce northwest-southeast seismicity trends. Figure 4A illustrates this type of environment prior to the block rotation. This example shows two right lateral faults with what will eventually be left-lateral faults acting as the block boundaries. Figure 4B illustrates the geologic setting post block rotation, where the blocks within the faults have rotated clockwise.

1.2 Seismicity

Southern California experiences a significant amount of seismic activity, with its proximity to the ”Big Bend” segment of the SAF producing a unique environment of tectonic stresses that results in a complex system of various types of faulting throughout southern California (Walls et al., 1998). A significant portion of this seismic activity occurs along the outer edges of the Los Angeles Basin, i.e. along the Newport-Inglewood and Elsinore Fault complexes (Figure 5), both right-lateral strike-slip systems.

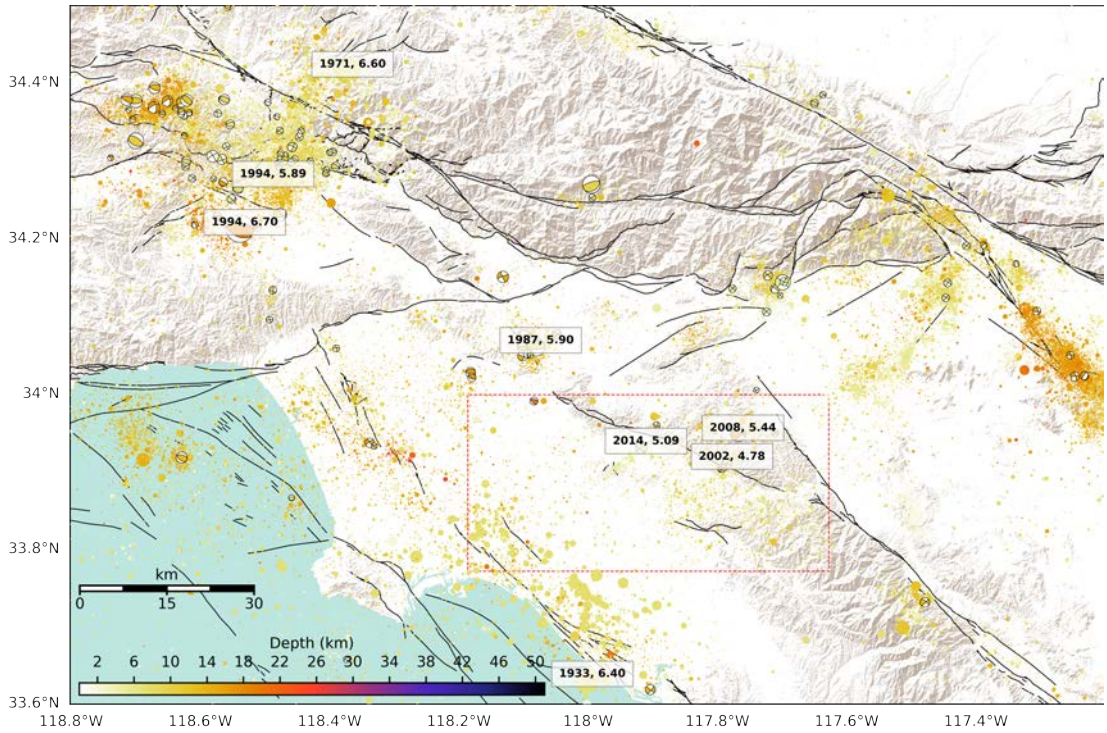

Figure 5: Shaded relief map of the seismicity throughout Southern California from 1932 to 2018, as located by the Southern California Seismic Network. Major faults are shown as black lines. Each event is represented by a single circle scaled by the magnitude of the event and colored by hypocentral depth. Historic events (pre 2000) with a magnitude > 5.8 are labeled by the year of occurrence and the magnitude of the event. More recent events (post 2000) with a magnitude > 4.75 are noted by the year of occurrence and the magnitude of the event. Events of magnitude 4.0 or higher are represented by their focal mechanism, if available. The dashed red box near the center of the map indicates the extent of the catalog used for this particular study. Earthquake catalog obtained from the Southern California Seismic Network (SCSN) (Hutton et al., 2010). Focal mechanism solutions were obtained from (Yang et al., 2012). Fault traces were obtained from the California Geological Survey (CGS) (Jennings et al., 2010).

The largest event within the Los Angeles Basin since 1900 was the 1933 M_L 6.4 Long Beach Earthquake that ruptured the southern segment of the Newport-Inglewood Fault off

the coast of Huntington Beach, CA (Figure 5). Other large events that have impacted the Los Angeles Basin, and to a larger extent southern California, include the 1971 M_W 6.6 Sylmar Earthquake, known colloquially as the San Fernando Earthquake, the 1994 M_W 6.7 Northridge Earthquake, and the 1989 M_W Whittier Narrows Earthquake, all reverse faulting earthquakes (Hauksson & Jones, 1989; Hauksson, 1990) (Figure 5). The 1971 Sylmar Earthquake and 1994 Northridge earthquake both struck the San Fernando Valley, with the 1971 event rupturing along the San Fernando segment of the Sierra Madre Fault System and the Northridge event occurring on a previously unknown blind thrust fault now known as the Northridge Hills Fault (Hauksson, 1990; Baldwin et al., 2000). The 1987 Whittier Narrows Earthquake occurred along a gently north-dipping fault that is commonly associated with the Elysian Park Fold and Thrust Belt, a series of thrust faults throughout the northeastern portion of the Los Angeles Basin (Hauksson & Jones, 1989) (Figure 5).

A closer observation of the seismicity near the eastern boundary of the Los Angeles Basin (Figure 5, Figure 6) indicates a lack of seismicity on strike with the Whittier Fault; instead, the trends of local earthquakes appear to be perpendicular to this fault. These trends are dominated by three major event sequences: 2002 Yorba Linda, 2008 Chino Hills and 2014 La Habra (Figure 6).

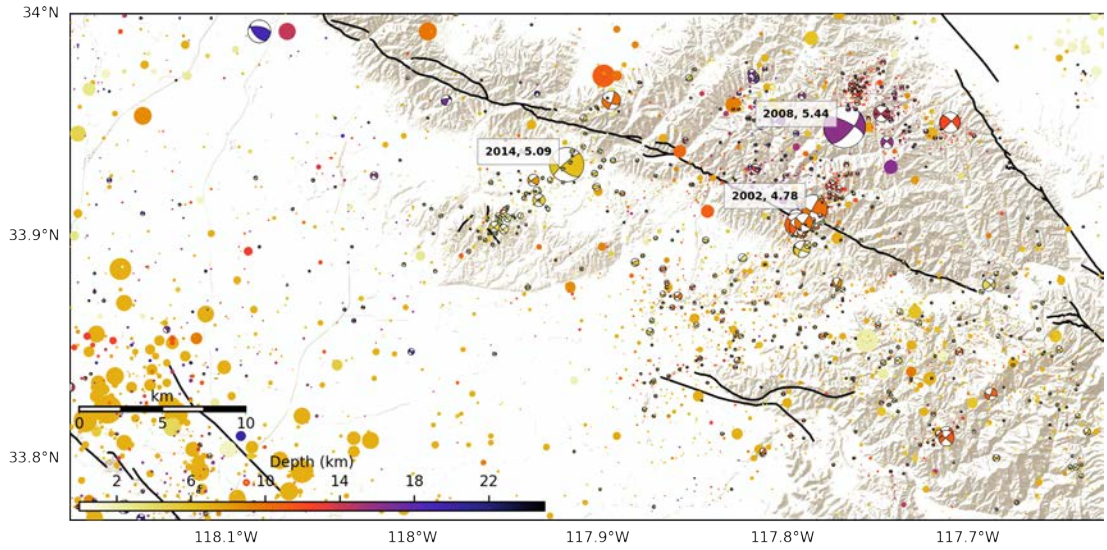

Figure 6: Seismicity of the eastern portion of the Los Angeles Basin. The location of this figure is shown in Figure 5 as a dashed red box. The majority of the seismicity shown in the figure is contained within three different seismic clusters: the 2002 Yorba Linda sequence, the 2008 Chino Hills sequence, and the 2014 La Habra sequence. Symbols and colors as in Figure 5. Event location and magnitudes were obtained from the Southern California Seismic Network (SCSN) (Hutton et al., 2010). Focal mechanism solutions were obtained from (Yang et al., 2012)

.

The region of the YLT may be characterized as a series of mainly small earthquakes trending in a northeast-southwest fashion, now dominated by two major event sequences: the 2002 Yorba Linda sequence and the 2008 Chino Hills sequence. The events within this trend show mostly strike-slip mechanisms, with few exhibiting a reverse motion (Figure 6). However, as with all focal mechanisms, there is uncertainty of the identification of the fault plane for these events. Of the two nodal planes that exist for each of these mechanisms, the northwest-southeast striking plane fits with the overall tectonic regime of the Puente Hills, aligning with the Whittier Fault. The northeast-southwest striking plane of these events however fits with the overall trend of earthquakes (Figure 6). Another sequence located towards the west of the YLT, known as the La Habra Sequence, contains earthquakes with similar mechanisms and the overall sequence is oriented in a similar direction as the proposed YLT trend (Figure 6). Potential candidates for the fault planes on which these events may have occurred are discussed in detail in Section 1.2.1 (Yorba Linda Sequence) and Section 1.2.2 (Chino Hills Sequence). In addition to these

three sequences, numerous events in the area are not associated with any known mainshock nor do they seem to be obviously related to any known fault trace (Figure 6).

1.2.1 Yorba Linda Sequence

The Yorba Linda earthquake sequence is dominated by a M_L 4.8 mainshock that occurred on September 3, 2002. This mainshock was preceded by two smaller foreshocks, each below a M_L 3.0, and was followed by more than 50 recorded aftershocks with local magnitudes ranging from 0.9 - 3.0, with 23 of these aftershocks occurring within the first 9 hours (Hauksson et al., 2002; Chen et al., 2005). The mechanism of the mainshock on first glance suggests that the earthquake occurred along the main trace of the Whittier Fault. However, the aftershock sequence does not follow that trend, but rather trends perpendicular to the Whittier Fault (Figure 7). Examination of earthquake depths also reveals that the aftershocks follow a near vertical orientation, matching a potential fault plane orthogonal to the Whittier Fault. Events shown in cross section A-A' appear to be loosely consolidated along a steeply dipping feature towards the northwest (Figure 8).

More recent events along this portion of the YLT include the 2012 Yorba Linda sequence that contains three events with magnitude $>$ 4.0, the largest of these a 4.6. This sequence of events presents similar focal mechanisms to those of the 2002 Yorba Linda mainshock and all of the larger events occur at similar depths (Figure 7, Figure 8). The 2012 events however occur just south of the Whittier Fault and have a more compact aftershock sequence as seen in Figure 8. The 2012 aftershocks also appear to have a tighter depth constraint compared to the 2002 sequence, with the 2002 sequence reaching towards greater depths (Figure 8).

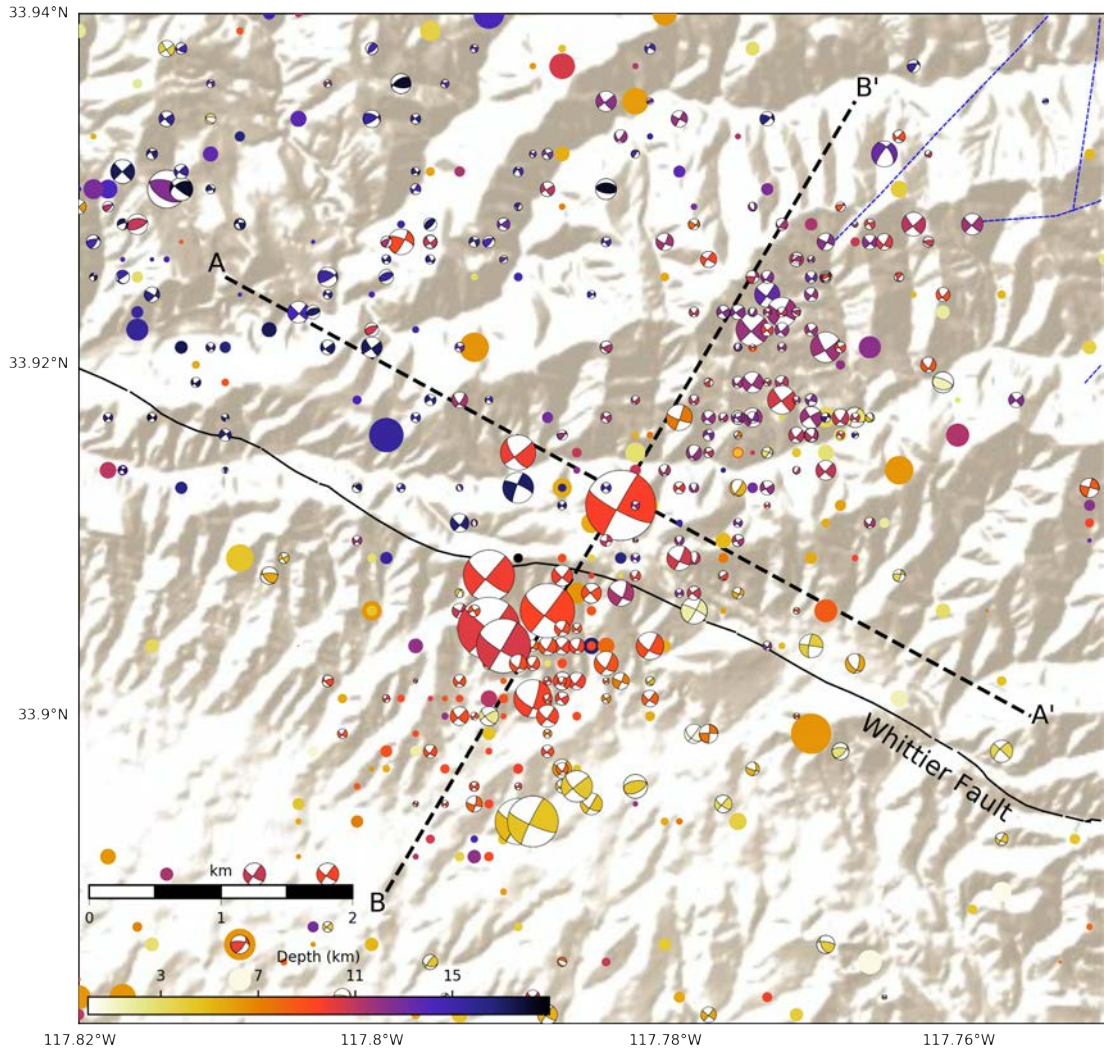

Figure 7: A shaded relief map of the Yorba Linda Sequence. Symbols, lines and colors as in Figure 6. The large dashed black line annotated as A-A' and B-B represent cross sections shown in Figure 8. The majority of the events making up this sequence have strike slip mechanisms of similar orientations. The larger events are clustered towards the southwest, close to the traces of the Whittier fault, while the smaller events extend towards the northeast. The events are increasing in depth towards the northwest, as shown in the cross-sections of Figure 8.

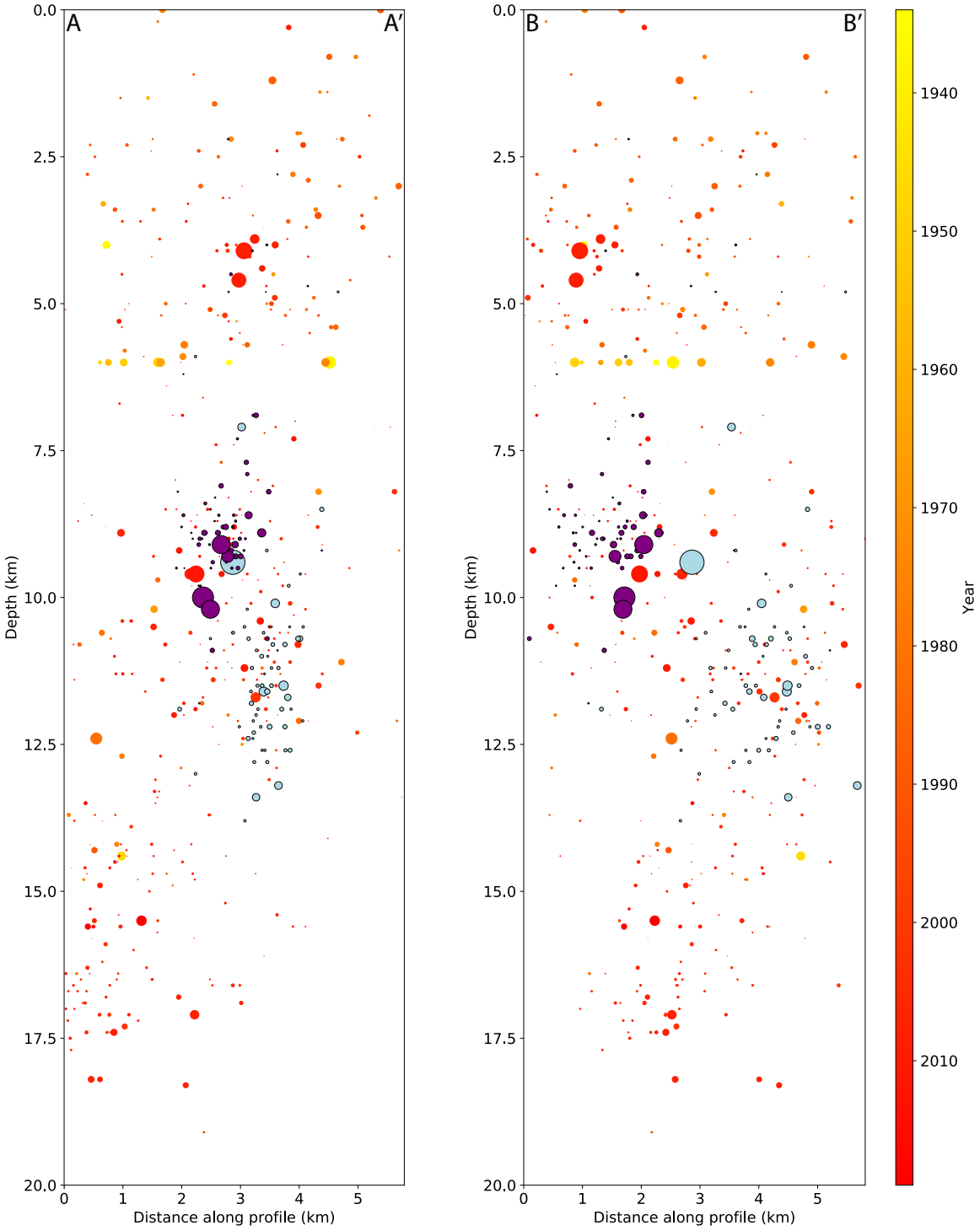

Figure 8: Cross section views of the Yorba Linda Sequence. The transect of each cross section is shown on the map in Figure 7. Each event for both cross sections is denoted by a single dot. The color of each dot is defined by the year of occurrence as shown by the colorbar. The outlined light blue events represent the 2002 Yorba Linda mainshock and its aftershock sequence for the first four months after the mainshock, whereas the outlined purple dots show the 2012 Yorba Linda mainshock and aftershock sequence. The 2002 sequence appears to have a larger horizontal and vertical extent, while the 2012 sequence is more consolidated around the mainshock.

The distribution of aftershocks towards the northeast of the 2002 mainshock appears to confirm that this was a left-lateral rupture on a previously undetermined geologic structure (Figure 8). Previous attempts at determining the orientation of the fault of this earthquake sequence have been carried out (Chen et al., 2005, 2010). The utilization of Green's Functions to determine directivity (Chen et al., 2005) for the 2002 Yorba Linda Earthquake concluded that this event likely ruptured along a northeast-southwest trending left-lateral strike-slip structure. Relocation of these earthquake sequences will clarify the structure(s) involved.

1.2.2 Chino Hills Sequence

The 2008 Chino Hills Sequence is dominated by the 2008 M_W 5.4 Chino Hills mainshock near the center of the Chino Hills (Hauksson et al., 2008). The mechanism of the 2008 mainshock shows a combination of a strike-slip and reverse motion along either a northeast-southwest trending or east-west trending nodal plane (Hauksson et al., 2008). The east-west nodal plane has a similar trend to the Whittier Fault located southwest of the mainshock, however, the dip of the Whittier Fault does not match with this nodal plane (Hauksson et al., 2008). There have been attempts to determine the causative fault of the 2008 Chino Hills Earthquake with various methods including synthetic seismograms (Olsen & Mayhew, 2010), Coulomb static stress changes (Hauksson et al., 2008), and finite fault inversions (Shao et al., 2012) with mixed results. Many of these publications cite that the wide distribution of the aftershock sequence complicates this analysis. Therefore, earthquake relocation may help illuminate the fault(s) involved.

The 2008 Chino Hills earthquake produced approximately 150 aftershocks $\geq$ M 1.0 with a M 3.6 and a M 3.8 as the largest of these events (Hauksson et al., 2008). The magnitude range of these aftershocks is unusual, given that Bath's Law predicts that the largest aftershock would be approximately 1.2 magnitude units lower than the mainshock, while the difference between these aftershocks and the mainshock are 1.8 and 1.6,

respectively. Very few of these aftershocks were found to be in the near vicinity of the mainshock, with the majority at larger distances (Hauksson et al., 2008) (Figure 9). (Hauksson et al., 2008) pointed out that the abundance of events at large distances from the mainshock might indicate that these aftershocks were statically or dynamically triggered. The aftershock distribution at depth shows that the majority of the events are situated at similar depths to the mainshock. However, when the dip of each mainshock nodal plane is considered, the trend of the aftershock sequence fails to correlate to either nodal plane orientation, thus adding more ambiguity to the determination of the causative fault (Figure 9).

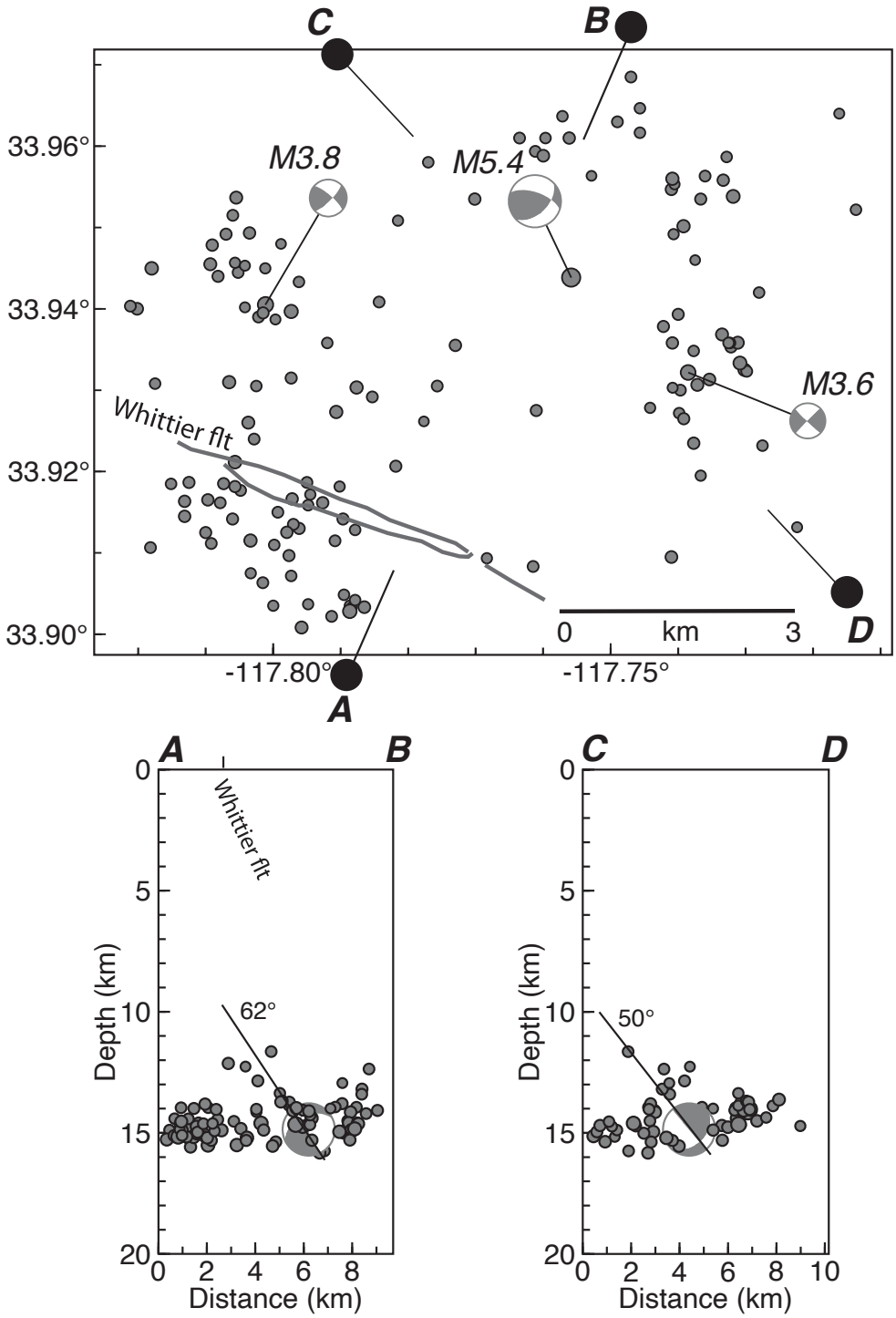

Figure 9: Simplified map and cross sections of the 2008 Chino Hills earthquake and aftershock sequence. The event locations shown within this map were relocated using HypoDD. Image originally published in (Hauksson et al., 2008). The mainshock and largest aftershocks of the sequence are represented by their mechanisms. Each dot represents a single aftershock. The map shows that the area surrounding the mainshock is relatively sparse of aftershocks, with many of the events occurring outside a 1.5 km radius. These events have a tight depth distribution around 15 km depth. The projected focal mechanism at depth show the dip of each nodal plane of the mainshock, showing that the distribution of aftershocks does not agree with either nodal plane.

The remainder of the seismicity in the Chino Hills area consists of events that have occurred periodically throughout recorded history, particularly from the late 1990s to early 2000s. These events are clustered towards the northwest and east in relation to the 2008 main event (Figure 10). These events, like the 2008 earthquake, do not follow any previously known late-Quaternary fault traces nor do they appear to line up with any identified pre-Quaternary fault traces. The focal mechanisms for most of these events show primarily a strike-slip movement with a slight oblique component. The majority of these events possess similar nodal plane orientations with the northeast-southwest nodal plane congruent with the orientation of the overall trend of the seismicity, which may indicate that this northeast-southwest nodal plane may be the fault (Figure 10). The presence of these events dotting the Puente Hills may also be an indicator of cross faults throughout the hills, as witnessed in the 2019 Ridgecrest Earthquake.

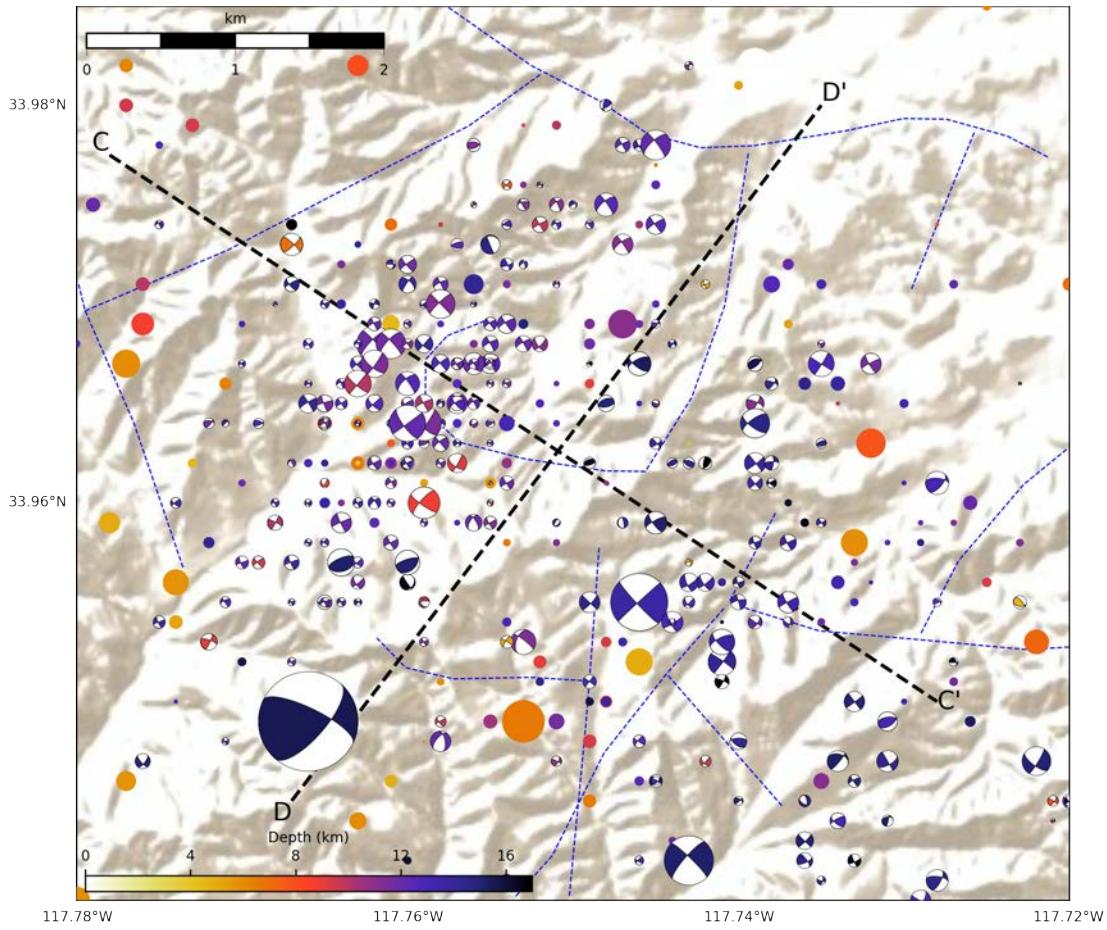

Figure 10: Shaded relief map of the Chino Hills earthquake sequence of the Yorba Linda Trend. An event is portrayed by its mechanism solution if its magnitude is ≥ 2.0. Symbols, colors and lines as in Figure 7. The thick dashed lines transecting the map define transects of cross sections C-C' and D-D' shown in Figure 11. The 2008 M_W 5.4 Chino Hills Earthquake is shown in the bottom left corner as the large navy-colored focal mechanism solution.

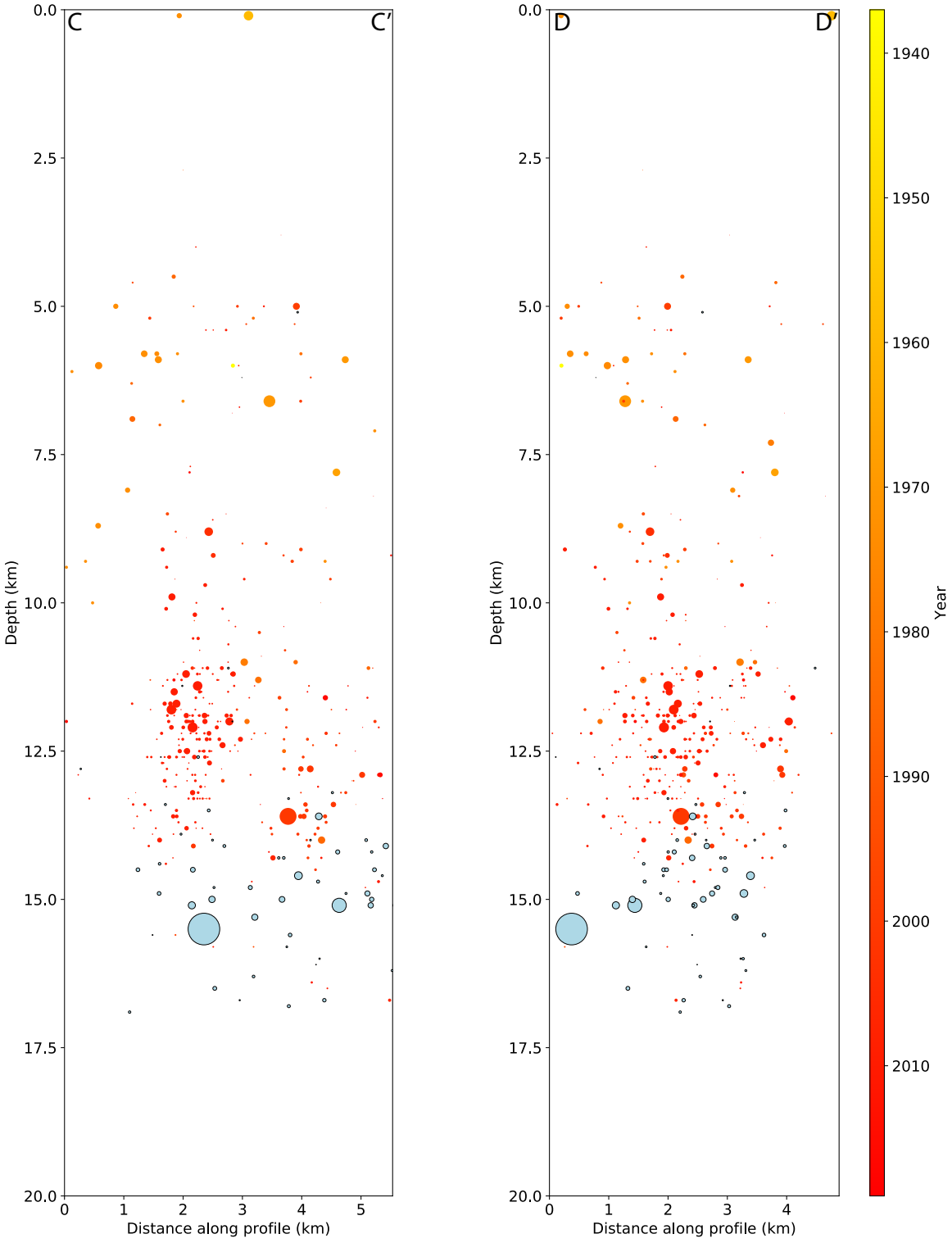

Figure 11: Cross sections of the Chino Hills seismicity of the YLT. The transects of C-C' and D-D' are displayed on the map in Figure 10. Symbols displayed as seen in Figure 8. The outlined blue dots are aftershocks after the first four months in close proximity to the mainshock, shown as the largest blue dot.

An observation with depth reveals that the majority of these events occur at relatively great depths with a range between 10 and 16 km. C-C' shows what appear to be two collections of events at depth with the more northwesterly cluster forming a near vertical trend, which includes the 2008 Chino Hills mainshock, while the eastern cluster is more scattered and does not appear to follow any trend or linear feature (Figure 11). If we observe the 2008 Chino Hills event and its aftershocks on both C-C' and D-D', it does not appear to be biased to either of these previous clusters, rather it follows a more horizontal trend around 15 km, agreeing with aftershocks that occur at larger distances, which also present themselves at similar depths (Figure 9, Figure 11).

1.2.3 La Habra Sequence

While the 2014 La Habra Sequence is not directly located along the YLT as defined by Hauksson, it does have similarities, particularly the orientation of the trend and the type of earthquakes it contains (Hauksson, 1990). If these earthquakes were located on one particular fault structure, it would agree with the left-lateral escape tectonics within the LA Basin (Walls et al., 1998; Hauksson, 1990; Donnellan et al., 2015). Previous geodetic analyses have concluded that the mainshock of this sequence occurred along a left-lateral strike slip fault dipping towards the northwest (Donnellan et al., 2015).

The aftershock sequence of the M_W 5.1 La Habra Earthquake trends in an orientation similar to that of the YLT, which would imply a left lateral strike slip fault (Figure 12). Many of these events are clustered around the Coyote Hills Fault System towards the south of the mainshock. The largest aftershock was a M_W 4.1 earthquake that occurred towards the northeast within the Puente Hills, at a greater depth than the majority of the aftershocks (Donnellan et al., 2015) (Figure 12). A significant portion of the focal mechanism solutions of the La Habra Sequence exhibit a northeast-southwest oriented nodal plane that matches well with the orientation of the proposed causative fault (Figure 12). Earthquakes exhibiting a reverse motion, particularly small events along the

F-F' transect, possess similar northeast-southwest oriented nodal planes to that of the strike-slip events in the La Habra Sequence (Figure 12). The combination of reverse and strike-slip earthquakes may imply that the causative fault of the La Habra Sequence is a left-lateral northeast-southwest striking fault with a steep dip towards the northwest. A significant number of reverse faulting earthquakes southeast of the La Habra Sequence could be related to the Puente Hills Thrust System (Walls et al., 1998; Yeats, 2004). Because the La Habra Earthquake sequence occurred near many major oil fields, there has been some debate regarding the possibility that this earthquake sequence was of an anthropogenic origin rather than a tectonic origin (Hauksson et al., 2015). However, aftershock statistics have suggested otherwise. (Donnellan et al., 2015; Hauksson et al., 2015).

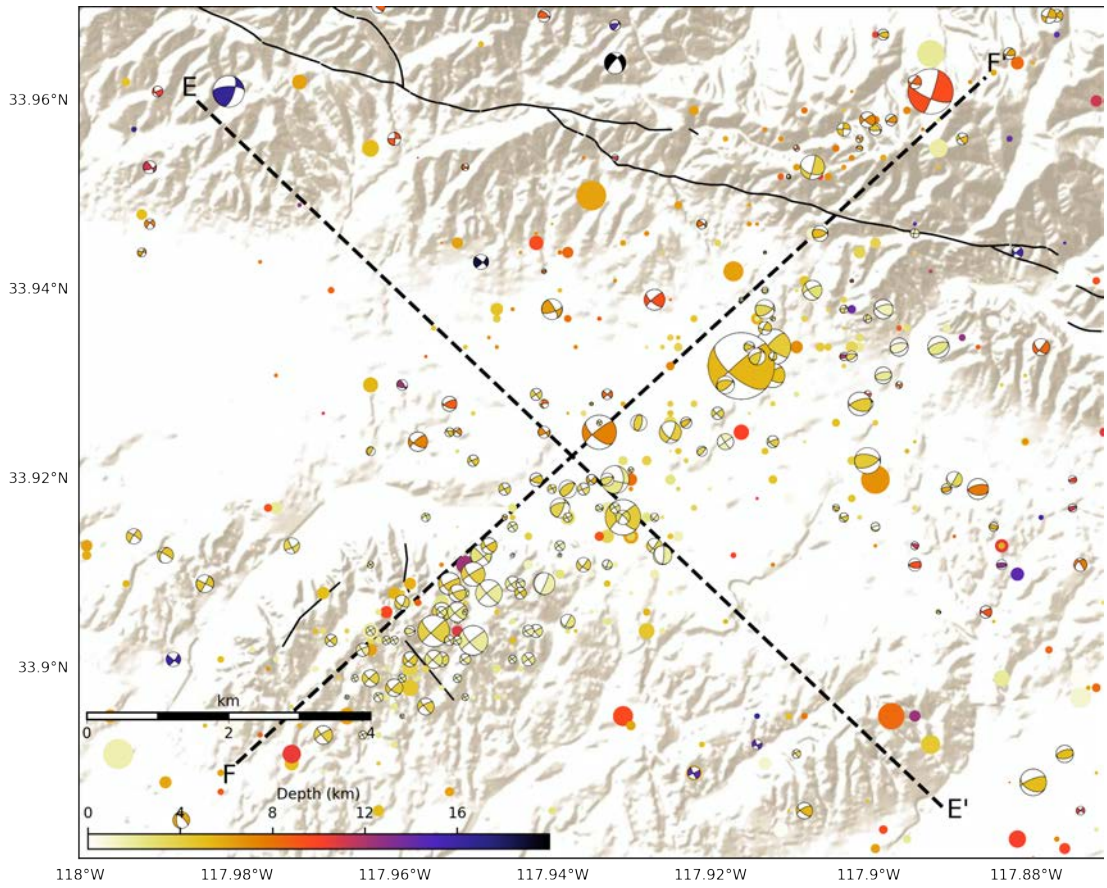

Figure 12: Shaded relief map of the La Habra Sequence. Earthquakes are denoted by either a single dot or a focal mechanism. Events $\geq$ 2.0 are represented by the focal mechanism of that event if the solution was determined. The depth of each event is characterized by the color of the dot as presented by the colorbar in the bottom left corner. The solid black lines indicate traces of known Quaternary faults, with traces of the Whittier Fault in the top right corner. The dashed black lines denote cross sections for the La Habra Sequence shown later in Figure 13.

Cross section E-E' reveals that the La Habra Sequence followed a near vertical feature at approximately 6-8 km along the cross section (Figure 13). The aftershocks affiliated with the 2014 mainshock are fairly tightly constrained along this near vertical feature, however the remainder of the events seem to be more dispersed along the cross section. The mainshock occurred at a depth of approximately 5 km, with most aftershocks at shallower depths. The largest aftershock, however, occurred at a greater depth than the majority of the aftershocks (Figure 13). F-F' shown in map view in Figure 12 and cross section view in Figure 13 both validate that many of the aftershocks are situated around the Coyote Hills Fault, at relatively shallow depths.

As is the case for the YLT, the earthquakes composing the La Habra Sequence in this northeast-southwest orientation may indicate the presence of an orthogonal fault, similar as seen in the 2019 Ridgecrest Earthquakes, the southern segment of the San Jacinto Fault System, and near the Cajon Pass (Nicholson et al., 1986; Mori, 1993; Ross et al., 2019). Each of these sequences presents itself as a trend of earthquakes along a previously unknown fault structure that is perpendicular to known fault traces. The utilization of seismic event relocation can help illuminate these previously unknown faults or fault structures.

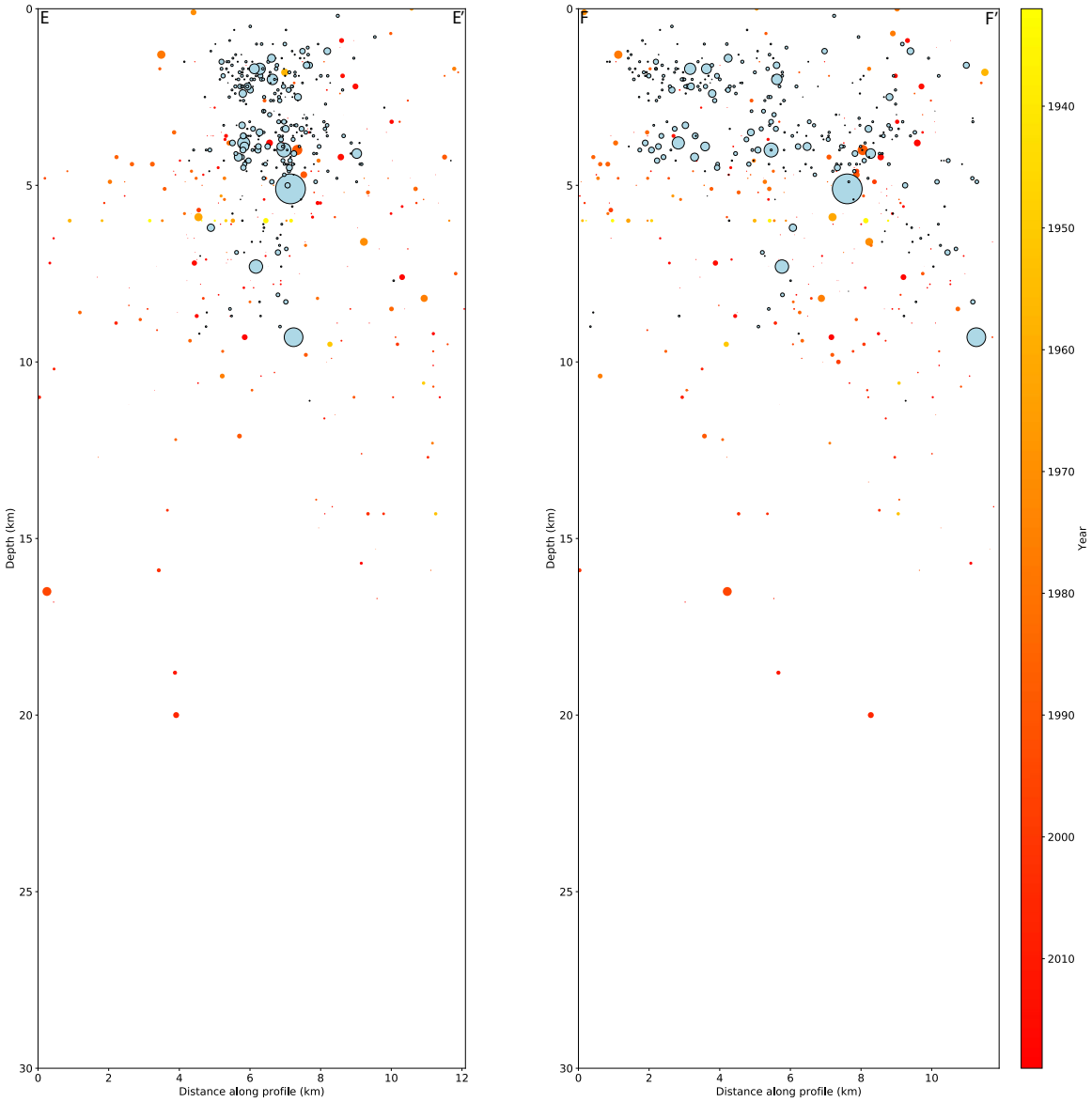

Figure 13: Cross Sections of the La Habra Sequence. The transects of E-E' and F-F' are displayed on the map in Figure 12. Each event in both cross sections is represented by a single dot where the year of the events is defined by the color as indicated by the colorbar. The outlined blue dots show events making up the aftershock sequence of the 2014 M_W 5.1 La Habra Earthquake.

2 Methodology

In order to determine whether the YLT is an existing fault trace that these events rupture along, we applied a cross correlation analysis on P-Wave and S-Wave waveforms for every event within the research area in order to improve arrival times of the events. We then proceeded to apply a relative relocation algorithm in association with three different velocity models and various different RMS differential residual travel time values to determine new improved locations for these events.

2.1 Waveform Collection

Over 2,000,000 waveforms of the 4434 events within the research area were gathered through the utilization of the Seismic Transfer Program (STP) ((SCEDC), 2013) (Figure 6). We collected all waveform data for each event dating back to 1932 up to 2018 from the Southern California Seismic Network (CI network) (Caltech, 1926) (Figure 14). Not all of these events possesses a recorded waveform for every station, likely due to the size of the event, the age of the event, or the distance from the station.

These events varied in size ranging from M 0 to M 5.4 and a depth range of 0 to 26 km. Each of these waveforms was then put through various preprocessing methods in preparation for the cross correlation. Within the CI network, SEED channels [HH-] (high sampling rate broadband seismometer) and [EH-] (short period seismometer) had priority over all other channels. The remaining channels: broadband low sampling rate [BH-], gravimeter [HG-], and accelerometer [HL- and HN-] channels were ignored. Each of the east, north, and vertical channels were used.

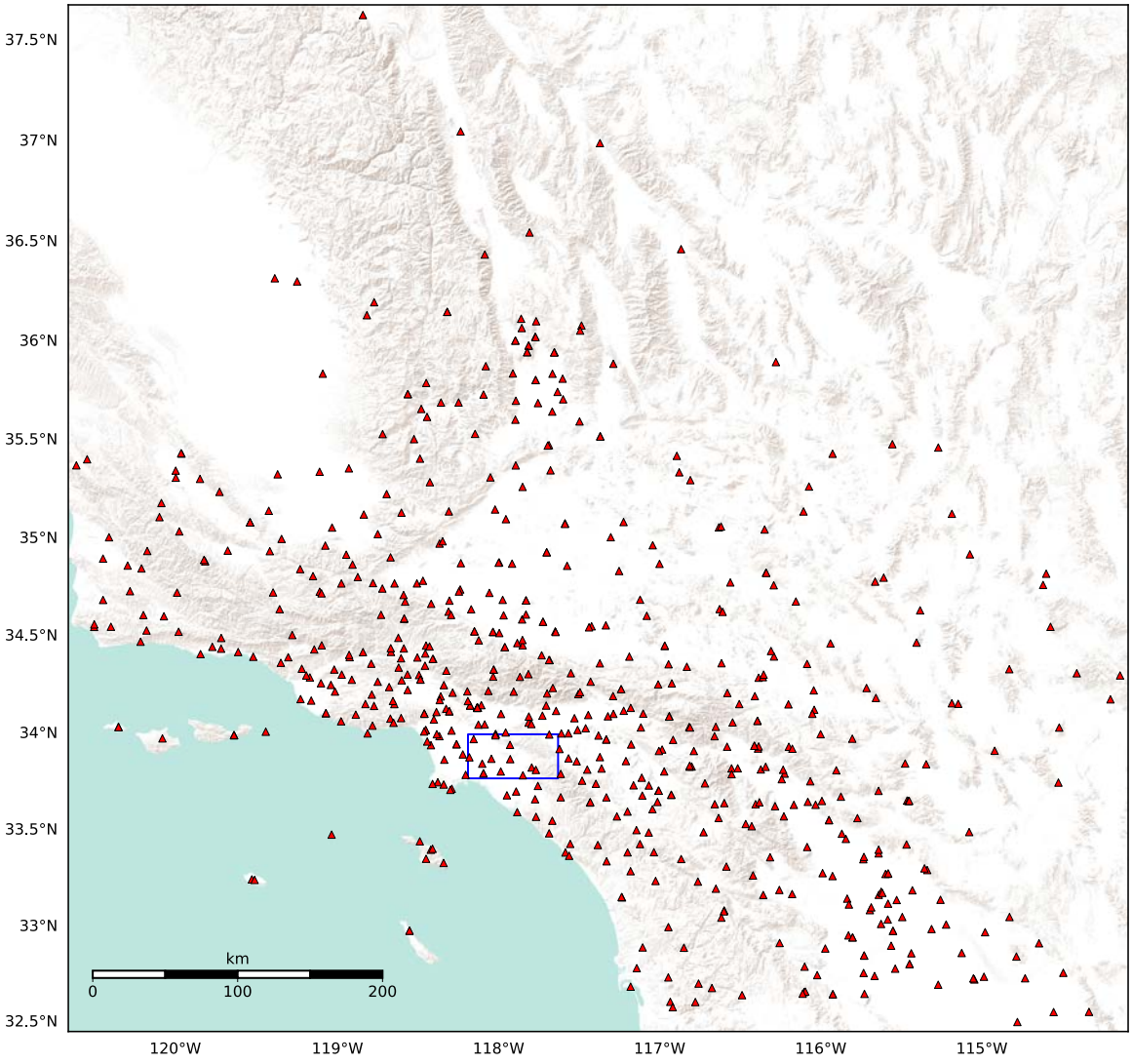

Figure 14: Shaded relief map of the CI network stations. Each of the red triangles indicates a single station that contained a waveform of any event within the research area (the blue box) that was obtained for the preprocessing and cross correlation process. Station locations were provided by the SCEDC (SCEDC, 2013).

2.2 Waveform Processing

The Southern California Seismic Network has used various sampling rates throughout its establishment, which means that waveforms for different events, stations and channels have different sampling rates throughout our catalog ((SCEDC), 2013). Because the earliest event in the catalog dates back to 1932, which means there are a myriad of different sampling rates, all waveforms within the acquired catalog were resampled to a uniform sampling rate of 100 Hz (Astiz et al., 2000; Richards-Dinger & Shearer, 2000;

Hauksson & Shearer, 2005; Schaff & Waldhauser, 2005; Lin et al., 2007; Hauksson et al., 2012). Resampling is done in order minimize the error of modified arrival times determined through cross correlation (Schaff & Waldhauser, 2005; Waldhauser & Schaff, 2008). A bandpass filter with cutoff frequencies of 1 Hz and 15 Hz was then applied to the waveforms to provide reliable results for the cross correlation (Schaff & Waldhauser, 2005; Waldhauser & Schaff, 2008).

Many of the waveforms obtained from the SCEDC did not have picked P-Wave or S-Wave arrival times. In order to accurately cross correlate the waveforms and relocate the events, theoretical P- and S- Wave arrival times were calculated for all waveforms that do not have arrival time picks. The 'setsac' function from the TauP Toolkit was used to mark arrival times (Crotwell et al., 1999). We used the IASP91 velocity model in order to calculate theoretical P-Wave and S-Wave arrival times (Kennett & Engdahl, 1991) (Figure 15). Theoretical P-Wave arrival times were only marked on the vertical components, whereas the theoretical S-Wave arrival times were marked on the horizontal components.

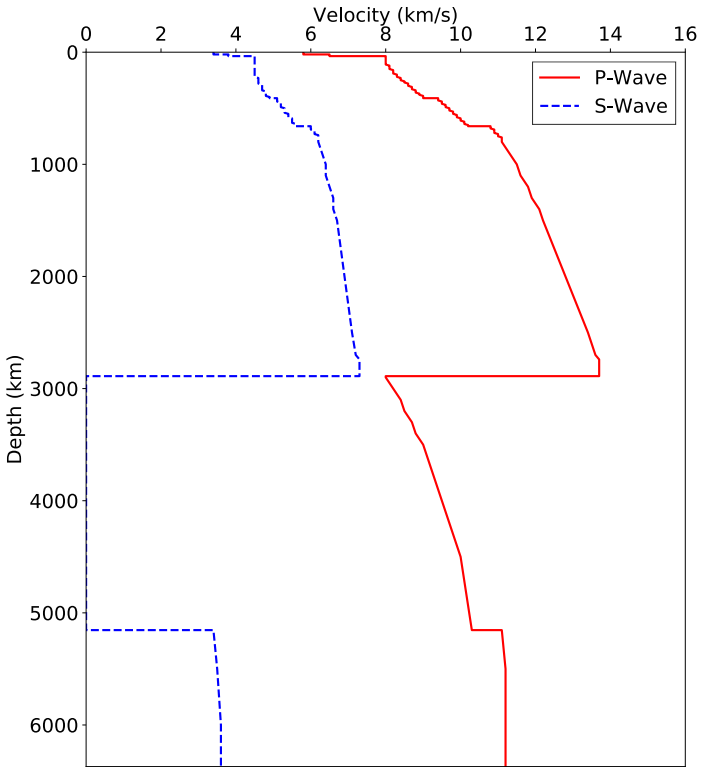

Figure 15: IASP91 velocity model that was used to mark theoretical P-Wave and S-Wave arrival times. The solid red line traces out the P-wave velocity with increasing depth while the dashed blue does the same for the S-wave. Velocity model from (Kennett & Engdahl, 1991).

Once arrival times were determined, the waveforms were cut in order to accurately correlate the waveforms around the P-wave and S-wave arrivals. The vertical waveforms are cut 1 second before and 1.5 seconds after the P-Wave arrival time and the north and east waveforms are cut 1 second before and 3 seconds after the S-Wave arrival time. This is done to capture the entire waveform without interference from other waves or unnecessary noise before or after the arrival (Waldhauser & Schaff, 2008). Because the cross correlation is station based, the waveforms were reorganized from event to station based datasets.

2.3 Cross Correlation

Cross correlation is a method used to compare the similarity of waveforms. The process involves adjusting a single earthquake waveform with respect to time in relation to a second earthquake waveform (Figure 16). As this waveform is adjusted in time, it is compared on

similarity to the static waveform. Its similarity is determined quantitatively from 0 to 1, with a value of 1 being a perfect match between the two waveforms. This value is defined as a waveform's cross correlation coefficient (C_C). In tandem with the correlation value an optimum lag time is obtained, or the amount of time a waveform has been adjusted or shifted to obtain the maximum C_C. This cross correlation process provides an improvement to an inaccurate P-Wave or S-Wave arrival times, thus improving the eventual location of the earthquake. This cross correlation analysis eliminates the bias of different people picking different arrival times in that it adjusts arrival times for a particular waveform based on the similarity with other waveforms and their arrival times.

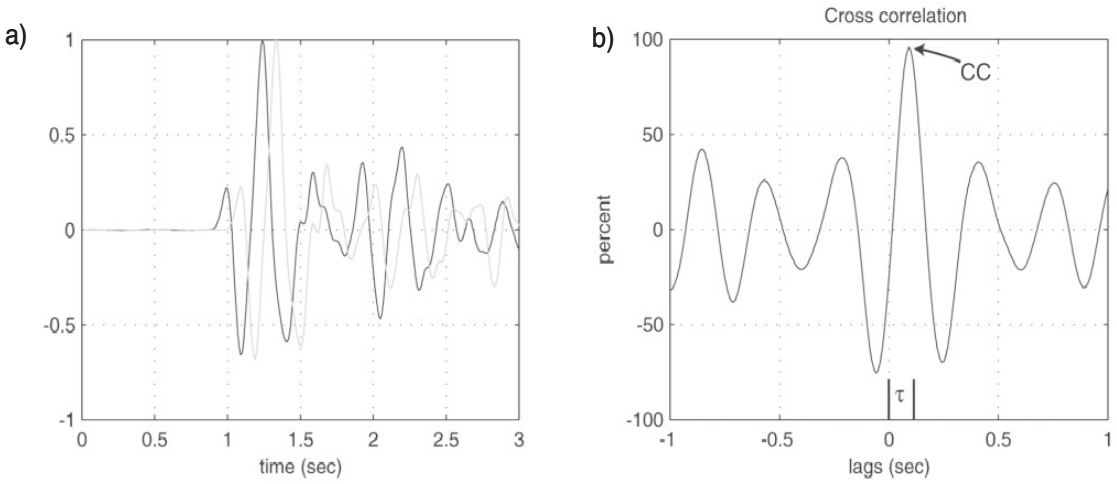

Figure 16: An example of the cross correlation process. Figure 16a illustrates the process of adjusting a single waveform (light gray) in relation to a static waveform (black) in order to obtain the maximum cross correlation value (CC). Figure 16b shows the varying CC values recorded with varying lag times. The maximum lag time adjustment (τ) to obtain the maximum CC is shown as an adjustment from 0, its initial time, to its final time where the CC is at its maximum value. Image from (Schaff & Waldhauser, 2005).

We utilized the Matlab toolbox package GISMO (Geophysical Investigation in Seismology with Matlab Objects) in order to carry out the cross correlation process (Thompson & Reyes, 2018). An example of cross-correlation of waveforms from this study using GISMO is shown in Figure 17 where we see 85 S-Wave waveforms, before and after application of a time shift based on the lag times corresponding to the maximum C_C of the cross-correlation. The adjustments of these waveforms result in a clear

alignment of the S-Wave arrivals between 1 and 2 seconds(Figure 17b).

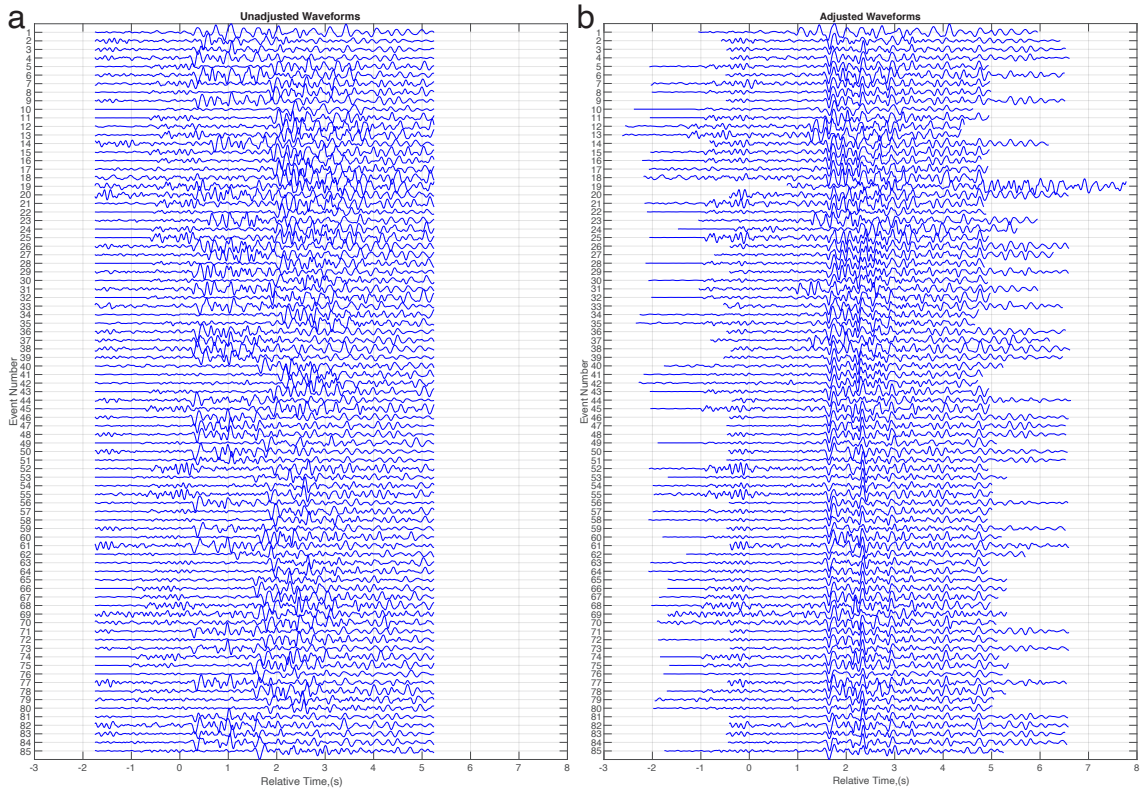

Figure 17: Image of the effect of lag time adjustment of 85 S-Wave waveforms from station CI.OLI based on the maximum C_C. Waveforms are organized by time of occurrence with earliest events at the top and most recent at the bottom. Figure 17a shows these 85 waveforms before alignment, with the upper and lower bounds 1 second before and 3 seconds after the S-Wave arrival time. Figure 17b shows these waveforms adjusted by the lag times determined by the cross correlation process. This adjustment is determined by the cross correlation values obtained from the highest average column from the cross correlation matrix in Figure 18 and associated lag time adjustments from Figure 19.

We cross correlated every event waveform from each individual seismic station within the CI network. Furthermore, we only cross correlated P-Waves with other P-Waves in order to improve the P-Wave arrival times (vertical components) and carried out the same process for S-Waves (horizontal components). However, we only kept waveforms and associating lag times that had a $C_C \geq 0.5$. Most relocation studies use a C_C of 0.6 or greater, however in order to relocate the highest amount of earthquakes possible, we chose to use 0.5. A correlation matrix displays how well each waveform is correlated with each other waveform (Figure 18). Similarly, a lag time matrix can be generated by utilizing the correlation matrix, and shows the values of lag times needed to adjust the waveform in

order to obtain the highest C_C (Figure 19). These values are then compiled into a list with the Event ID of the waveform, the other Event ID of the other waveform with which it was cross-correlated, the optimum lag time, the C_C, and the type of wave to be used by the relocation program (Table 1). The same method is applied to the P-wave arrivals for all of the stations within the network.

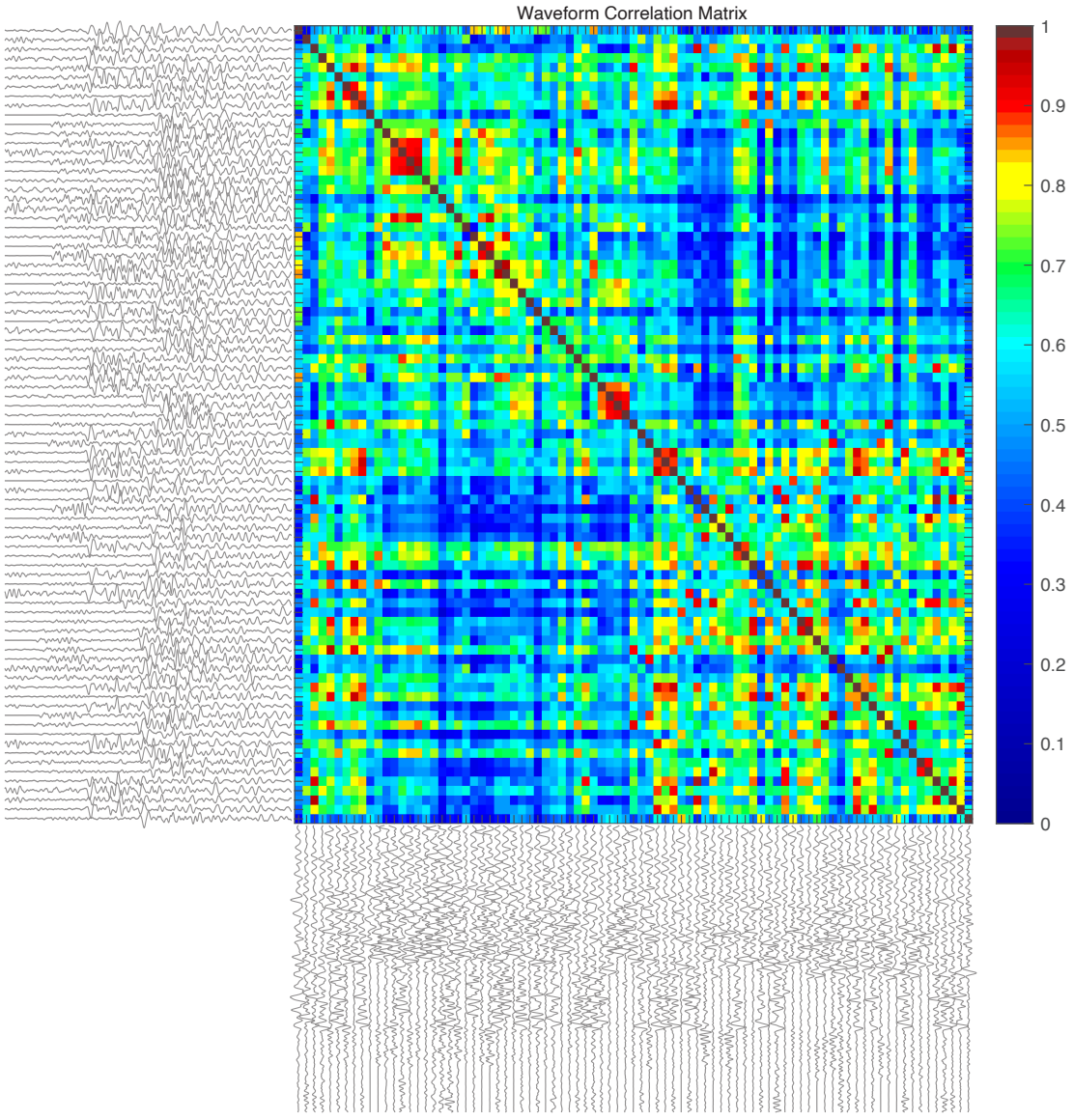

Figure 18: Correlation matrix of 85 waveforms that contain a minimum C_C threshold of 0.5 to at least one other waveform. The topmost waveform along the y-axis is the same waveform as the leftmost waveform along the x-axis. The value of the C_C is represented by the color bar to the right. Note the presence of values lower than 0.5 in this matrix. These values are present because the waveform is not well correlated to that corresponding waveform. That waveform is still selected because it has a C_C of 0.5 or greater with at least one other waveform.

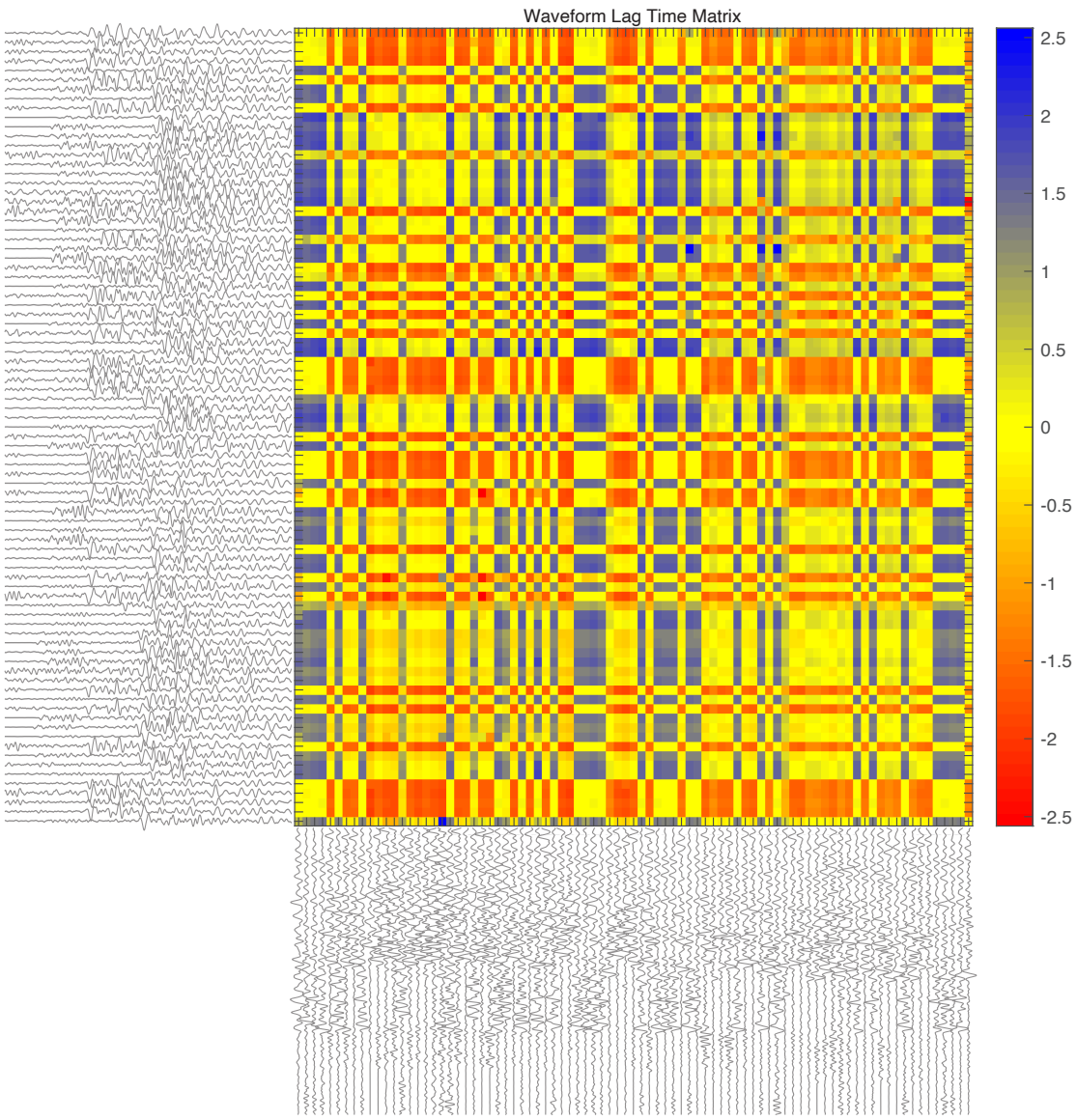

Figure 19: Lag time matrix of 85 waveforms representative of the correlation matrix in Figure 18. The topmost waveform along the y-axis is the same waveform as the leftmost waveform along the x-axis. Lag time adjustment (in seconds) is represented by the color bar on the right. The diagonal line of lag time values from top left to bottom right show waveforms being compared with itself, resulting in an optimum adjustment of 0 sec.

Table 1: Table of an example of waveform correlation data obtained from the correlation and lag matrices similar to that shown in Figure 18 and Figure 19. It is important to note that only waveforms with a C_C of 0.5 or greater are kept for this analysis.

Event ID 1	Event ID 2	Station	Lag Time in seconds	C_C	Wavetype
10000913	10005169	CI.OLI	0.78999	0.70441	P
10000913	10006369	CI.OLI	0.69	0.51097	P
10005169	10006369	CI.OLI	-0.08999	0.55026	P
10000913	10006809	CI.OLI	0.77999	0.65293	P
10005169	10006809	CI.OLI	-0.01	0.77406	P
10010437	10010481	CI.OLI	0.18	0.96783	S
10023817	10025329	CI.OLI	0.22	0.50777	S
10006809	10026233	CI.OLI	0.11	0.59111	S
10023817	10026233	CI.OLI	0.84	0.52639	S
10036069	10055701	CI.OLI	0.18	0.51848	S

2.4 Earthquake Relocation

In order to relocate earthquakes, it is essential to understand how the initial locations of earthquakes are determined. Once an earthquake occurs, the P-waves and S-waves radiate outwards from the hypocenter with varying velocities depending on the medium through which the waves propagate (Stein & Wysession, 2009). Once that wave arrives at a seismic station, a waveform is recorded for that event (Figure 20). Absolute arrival times are then picked by human operators. The arrival times of these waveforms are then put through a velocity model and the absolute hypocenter of the earthquake is determined through triangulation. If two earthquakes contain waveforms of high similarity, then it is likely that those two events occurred within close proximity towards one another, simply because the seismic waves would have to travel through the same medium along their paths towards the station (Shearer, 1997). Arrival time picks, however can be inaccurate. The use of cross correlation can improve inaccurate picks by comparing waveforms to each other and adjusting the arrival time measurements based on their similarity to each other.

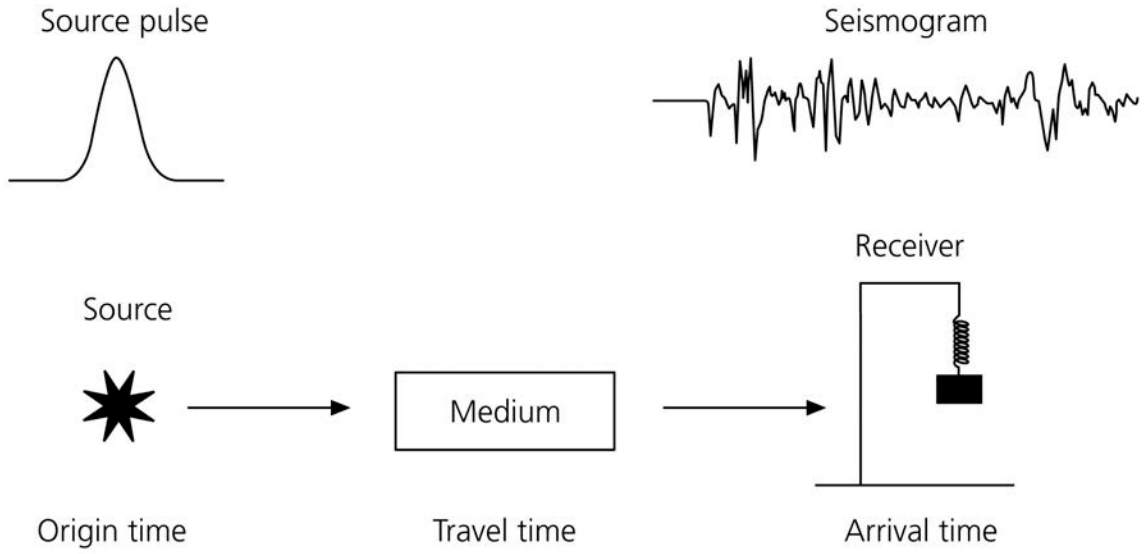

Figure 20: A simple schematic of the path that a waveform takes from a seismic source, through a medium. and eventually arriving at a seismic receiver. Image from (Stein & Wysession, 2009).

When cross-correlations have been calculated and all of the measurements are

compiled into various files, this data can then be used in a relocation program. We chose to use the GrowClust program to perform the earthquake relocation. GrowClust is a relocation algorithm that utilizes the differential travel times (lag times) and cross correlation values that were determined in the cross correlation process and applies them to a hierarchical clustering algorithm (Trugman & Shearer, 2017). Essentially, it compares waveforms that have been cross correlated and their calculated differential arrival times determined from the lag times, and groups these waveforms and corresponding earthquakes into clusters and subsequently relocates them based on these linked events (Trugman & Shearer, 2017). This differs from other relocation programs in that this combines the cluster analysis from the correlation values and lag times and then relocates the earthquakes, whereas other relocation codes only (directly) relocate the events. GrowClust also isolates itself from other relocation algorithms by placing more weight on higher correlated events in the relocation process (Trugman & Shearer, 2017).

Another advantage of the GrowClust algorithm over, for example, double difference relocation algorithms is that it uses the L1 norm (least absolute value, the median in one-dimensional problem) as opposed to the L2 norm (conventional least squares, the mean in one dimensional problem) (Shearer, 1997; Trugman & Shearer, 2017). This is advantageous because the utilization of the L1 norm makes the relocation of the earthquakes in a cluster less affected by outliers within the cluster. Various studies have shown that the utilization of the L1 method has shown improved locations compared to those that use the L2 norm (Shearer, 1997; Matoza et al., 2013; Trugman & Shearer, 2017).

An example of the advantage of using the GrowClust algorithm as opposed to other relocation programs is shown in Figure 21. This figure details the 2014 Sheldon Sequence in northwestern Nevada and the results of a relocation of these initial events using two different algorithms: GrowClust and HypoDD. The relocations show a tighter distribution for the GrowClust relocations than the HypoDD relocations, with the GrowClust results

showing a clear splay branching off from the main sequence trend that is not as clearly seen with the HypoDD relocation (Figure 21b). The GrowClust algorithm separated events into clusters and relocated them in relation to each other. The GrowClust relocations are tighter, likely due to the weighing of pairs with higher correlation values and the lack of dependence on outliers, which is something the the HypoDD algorithm does not consider.

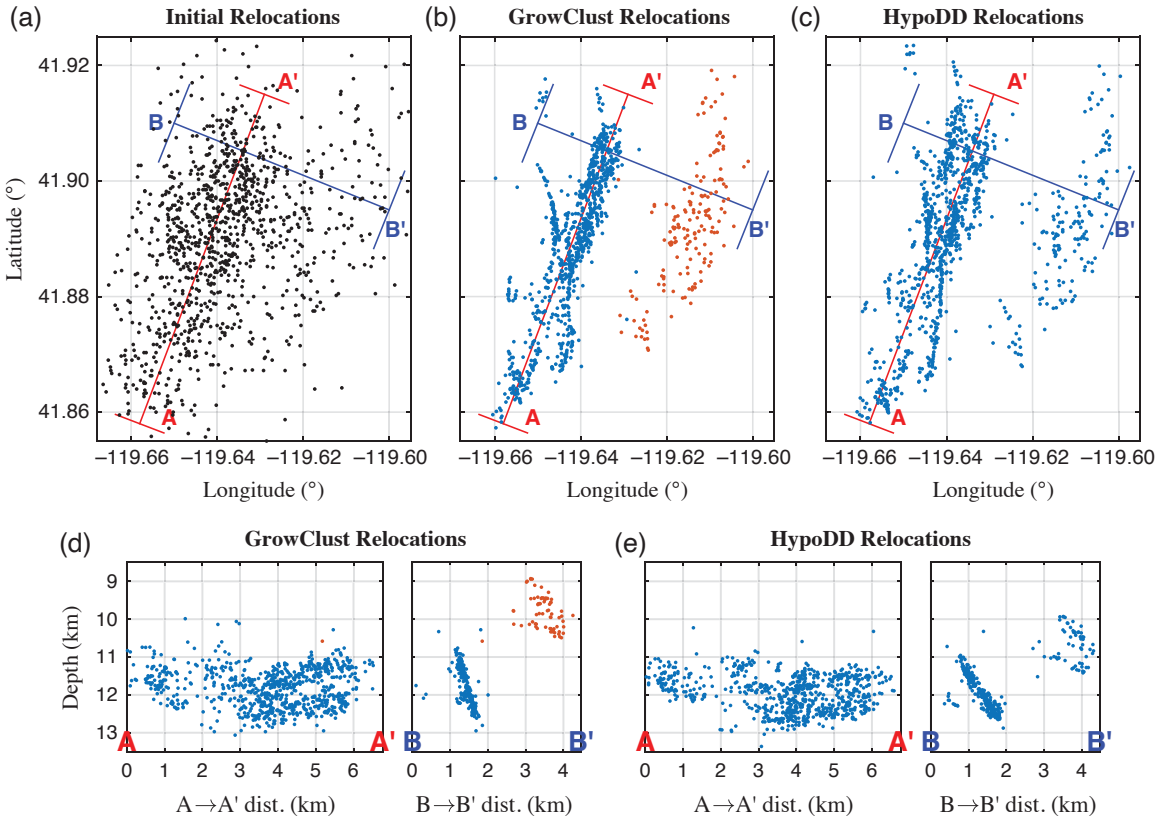

Figure 21: An example of relocations using two different relocation algorithms: GrowClust and HypoDD for the 2014 Sheldon sequence in the northwestern corner of Nevada. Figure 21a shows the initial locations of the events while Figures 21b and 21c show relocations carried out by GrowClust and HypoDD, respectively. The different colored events are events that have been clustered by the GrowClust algorithm Figures 21d and 21e show the cross sections of the relocated sequences produced by each algorithm.Figure from (Trugman & Shearer, 2017).

In the relocation process, the GrowClust algorithm runs through all event pairs per station and selects the event pair with the highest C_C and relocates those events to a new location based on the differential arrival times, and declares a cluster centroid at the midpoint between these two events (Trugman & Shearer, 2017) (Figure 22b, 22c). The algorithm then runs through each event pair with the next highest C_C (Figure 22d, 22e).

If two event pairs have a sufficient correlation value, but are located within two separate clusters, then the algorithm relocates both clusters in relation to each other by determining the midpoint of the two centroid clusters and adjusting the clusters in relation to the new centroid cluster (Figure 22g, 22h). These two clusters are now redefined as one single cluster (Figure 22f). Essentially, if two events within the same cluster have a high correlation value, then it is likely that these events occurred in close proximity as stated earlier in this chapter (Shearer, 1997). In addition to the newly relocated events, the GrowClust algorithm also calculates a root-mean-square (RMS) P-Phase residual differential time and an RMS S-Phase differential time, as well as horizontal and vertical location errors for the new locations based on these residual differential times. The residual differential time is the difference between the observed arrival times and the theoretical arrival times that are determined through the GrowClust algorithm.

As previously stated, this type of relocation is advantageous because it weighs event pairs with higher correlation values more than others and relocates all other events within the same cluster based on the next highest correlation value. This means that the centroid cluster is primarily determined by the event pair with the highest correlation value and is adjusted less and less with each successive relocation. Another advantage is that the cluster relocations are not as dependent on outliers as seen in Figure 22 where event B does not pair with any other event within the cluster, and thus is ignored in the relocation. (Trugman & Shearer, 2017). Through a series of bootstrap uncertainty iterations, the cross correlation data that was gathered prior to the GrowClust process are organized into arrays of length N_{ph}, where N_{ph} denotes the total number of combined P and S phase observations. With each successive bootstrap iteration, the algorithm then generates resampling vectors to perform random resampling of these input arrays (Trugman, 2017a). That is, the GrowClust algorithm will reorganize the event pairs, maintaining that the highest correlation values will be relocated first, and perform another relocation. The final relocation with the smallest errors will then be chosen as the optimal relocation results.

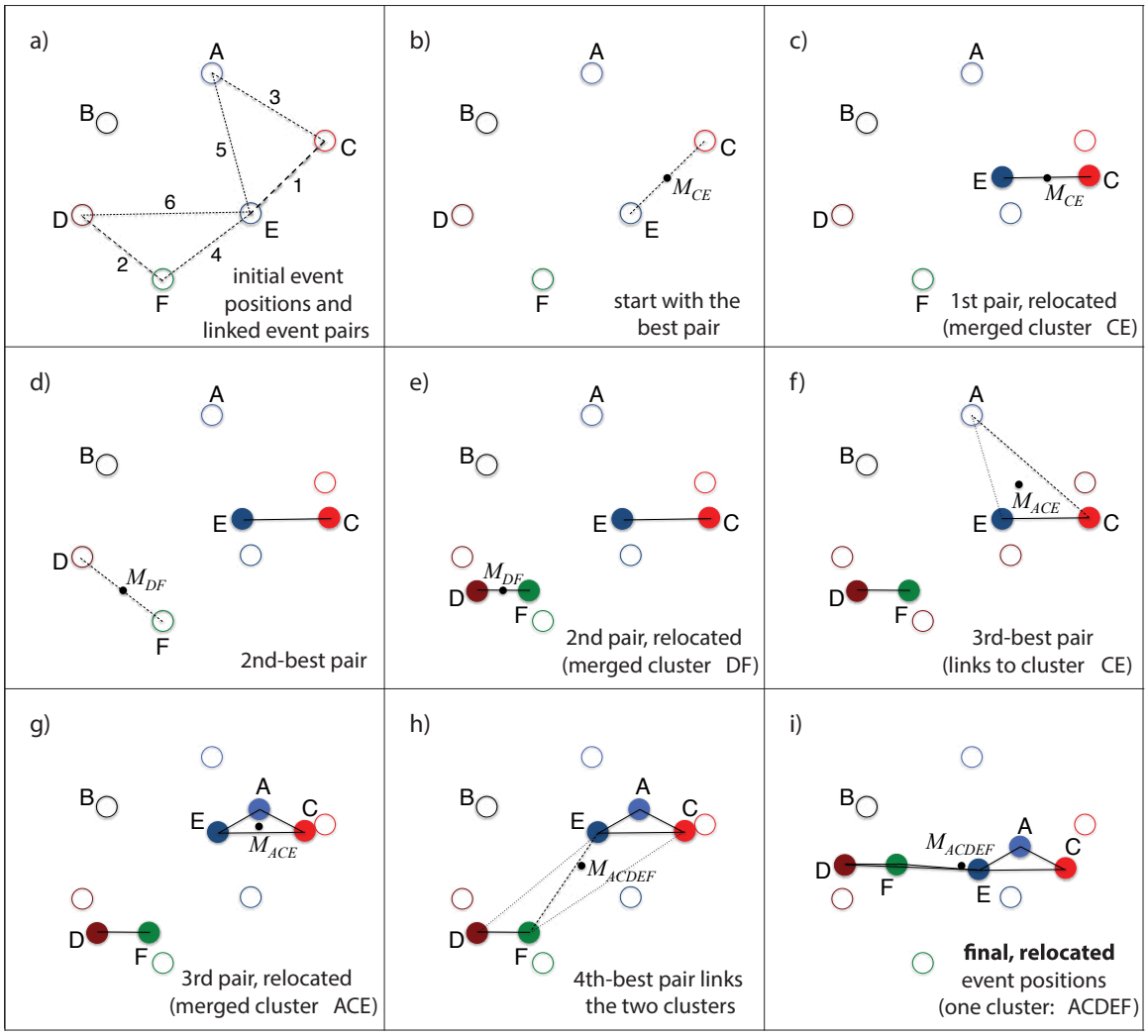

Figure 22: A schematic of the GrowClust relocation process. The boxes display the sequence of steps that are taken to relocate events within a cluster determined by the algorithm. Box (a) shows the location of each event in its original location as illustrated by the open circles denoted by a letter. The thickness of each dashed line denotes the level of similarity of events, with the thickest line showing events with the highest correlation. Each subsequent box shows the relocation of events of the highest correlation value, eventually leading to the final result shown in box (i). Event B is shown to not have been relocated at all because this event does not contain any links to other events, thus staying in place. Image from (Trugman & Shearer, 2017).

Along with the cross correlation coefficient and lag time measurements that were produced, we applied three different 1-D velocity models: the IASP91 Velocity Model (Kennett & Engdahl, 1991), a smoothed Southern California Velocity Model from an analysis of the 2008 Chino Hills Earthquake (Shao et al., 2012), and a velocity model of the LA Basin from an aftershock study of the 1987 Whittier Narrows Earthquake (Hauksson & Jones, 1989) (Figure 23). We limited the maximum distance for two events

to be merged into a cluster to 5 km. We required that in order for a cluster to be defined, a minimum of 8 events are needed. Various different distances have been used for cluster merging, ranging from 2 km to 15 km. We had chosen 5 km due to the small area with with the earthquakes within this research encompass. We also limited the amount of earthquakes must be considered a cluster to 8 events because a majority of other relocation studies had chosen 8 events to be the cutoff. We used different maxima for the root-mean-square (RMS) differential travel time residuals (0.1 s to 0.8 s) to obtain the best results.

The RMS differential travel time residual for a proposed cluster merger is a tolerance value that is entered by the user. This value is a parameter that determines whether an event combines with another event and forms a cluster. In essence, If an event is paired with another event, they are relocated and merged into a single cluster. The algorithm then calculates the RMS differential travel time residual for this newly merged cluster. However, if the RMS differential travel time residual exceeds the maximum RMS differential travel time residual that was chosen, this pair is ignored and these events are not relocated with respect to each other. Furthermore, if one of these events in an event pair is already part of a cluster and the addition of the other event in the pair results in the cluster RMS differential travel time residual exceeding the entered RMS differential travel time residual, then that event pair is ignored.

We only used correlation data from stations within a 60 km radius from the center of the research area in order to avoid any seismic wave reflections from the Mohorovii discontinuity, which could compromise the accuracy of the relocations (Figure 24). In addition to this, farther stations are generally lower in frequency and will have high correlations for events high correlations even when the events are not very similar because of the limited bandwidth of the records (Schaff & Waldhauser, 2005). Reflections from the mantle can complicate the relocation process, because it can introduce additional arrivals or compromise the accuracy of arrival times, i.e. if an S-wave arrives at a station

as a reflected P-wave arrives at the same time, it could lead to an incorrect measurement of the arrival time of the S-Wave.

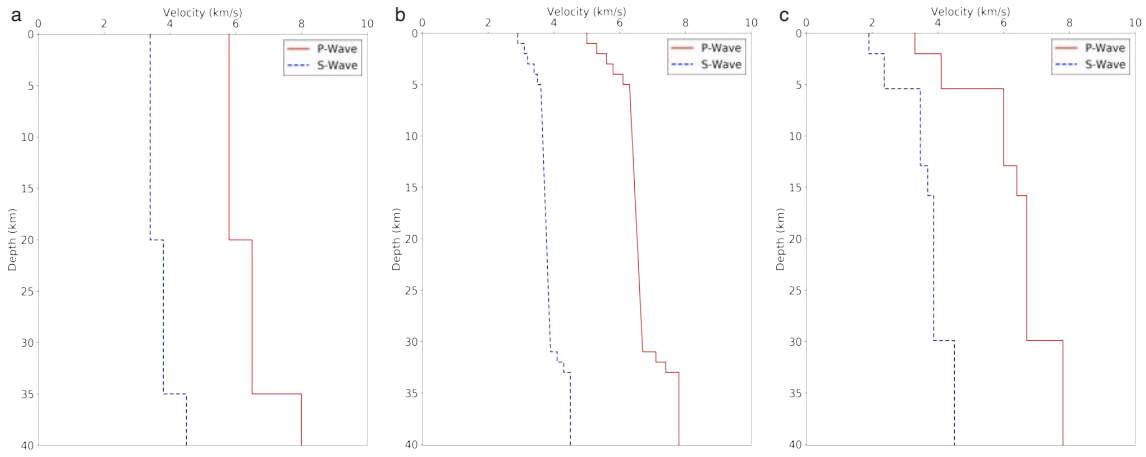

Figure 23: The various velocity models that were used in the GrowClust Relocation Algorithm. Figure 23a is the IASP91 velocity model provided by (Kennett & Engdahl, 1991). Figure 23b is the smoothed Southern California Velocity Model provided by (Shao et al., 2012). Figure 23c is the velocity model for the LA Basin from the analysis of the 1987 Whittier Narrows Earthquake provided by (Hauksson & Jones, 1989).

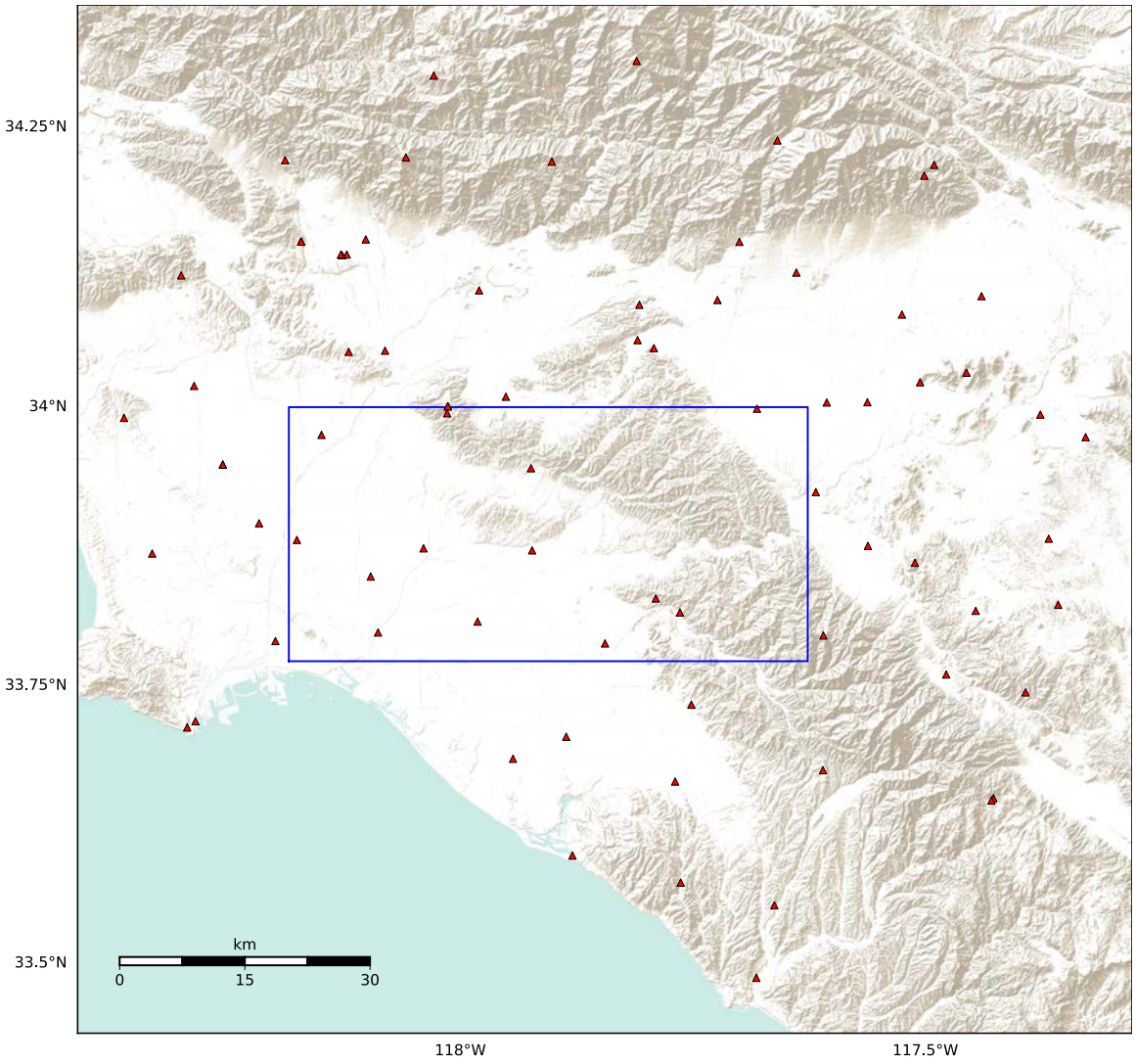

Figure 24: A map detailing the stations that were used in the relocation algorithm. Red triangles denote approximate locations of stations, while the blue box indicates the location of the research area.

3 Results and Interpretation

We found that, of the earthquakes within the research area, only events located near the eastern portion of the LA Basin were successfully relocated. The primary reason is that many of the not relocated events did not have any event pairs with other earthquakes. Over half of these events occurred before the 1980s. During this time, the station coverage was sparse and the available waveforms for these events were also sparse, resulting in an insufficient number of waveforms for relocation. In this chapter, we present the relocations produced from each velocity model: the IASP91 velocity model, the smoothed southern California velocity model, and the LA Basin velocity model determined from the 1987 Whittier Narrows Earthquake (Figure 23). In tandem with the velocity models, the results presented use a 0.2 s RMS differential travel time residual for a proposed cluster merger per recommendation of the GrowClust algorithm. We also show results for a 0.6 RMS differential travel time residual for comparison (Trugman, 2017b). If an event is paired with another event, they are relocated and merged into a single cluster. The algorithm then calculates the RMS differential travel time residual for this newly merged cluster. If the RMS differential travel time residual exceeds the maximum value that was selected, this pair is ignored and these events are not merged into a cluster and relocated with respect to each other.

3.1 Results for 0.2 RMS Differential Travel Time Residual

Table 2 shows the relocation statistics using a 0.2 RMS differential travel time residual parameter for all velocity models. The first column denotes which velocity model was used for that particular relocation attempt. The second and third columns show how many total events were used as input to the algorithm and how many of those events were relocated, respectively. The fourth and fifth columns indicate how many clusters with more than eight events were constructed and how many of the relocated events are situated within

them. The sixth and seventh columns (Input event pairs and Event pairs used) denote how many total event pairs were entered into the GrowClust algorithm and how many of them were actually used. And finally, the last two columns show how many P-wave and S-wave correlation sets were successfully used in the relocation process.

Determining which of the relocation results is the optimal result can be aided by multiple values listed within this table. The LA Basin velocity model relocation results have the most relocated events (Table 2). These relocation results also have the smallest amount of clusters with more than eight events as well as the highest number of relocated results within these clusters. This is preferred in that there are more relocated events that have more than eight event pairs that were used to relocate those events. A large number of event pairs used in the relocation process is preferred because this indicates that the results are constrained by more data. As expected with the higher number of relocated events, the LA Basin also possesses the largest number of event pairs used in the GrowClust algorithm.

While the smoothed southern California and LA Basin velocity model relocation results have the same amount of S-wave correlation data that was used, the latter uses more P-wave correlation measurements. An unusual feature to note is that among all velocity model relocation results, there are more S-wave correlation values used than P-wave measurements. This is unusual in that typically the S-wave of a waveform is more difficult to correlate.

Table 2: Table depicting the various relocation statistics of the results produced by the GrowClust algorithm for the three different velocity models. ”SoCal” represents the smoothed southern California velocity model and ”LAB” represents the LA Basin velocity model.

Velocity Model	Total events	Relocated Events	Clusters with ≥ 8 events	Relocated events within clusters	Input event pairs	Event pairs used	Xcor data (P-wave)	Xcor data (S-wave)
IASP91	4434	2149	58	1732	2396533	87299	247154	363400
SoCal	4434	2143	53	1725	2396533	93121	261983	386054
LAB	4434	2197	52	1758	2396533	101382	285314	386054

3.1.1 IASP91 Velocity Model Relocation Results

Of the 4434 total events within the research area, the GrowClust algorithm relocated 2149 events using the IASP91 velocity model (Figure 23a) under a maximum 0.2 RMS differential travel time parameter (Table 2). 87,299 event pairs were used to relocate the events plotted in Figure 26. The number of differential times used to calculate the new locations were 247,154 and 363,400 for the P-waves and S-waves, respectively (Table 2). As will be discussed later, larger magnitude events are more difficult to relocate, particularly due to the lack of waveform similarities with other events. This is due to larger events being more complex; they are longer in duration or possess source complexities, resulting in more complex waveforms and thus not having many event pairs. Original locations and relocated locations of every event relocated with respect to depth using this velocity model and RMS differential travel time residual can be viewed in Appendix A: Figure 103 and Appendix B: Figure 106, respectively.

Figure 25 shows the frequency of successfully relocated events. The average relocation distance was 1.637 km, while the majority of the events were shifted between 0.727 and 2.548 km from their original location. 32 events were relocated to distances exceeding 4.0 km from their original locations. Figure 26 has these relocated distances plotted for each respective event.

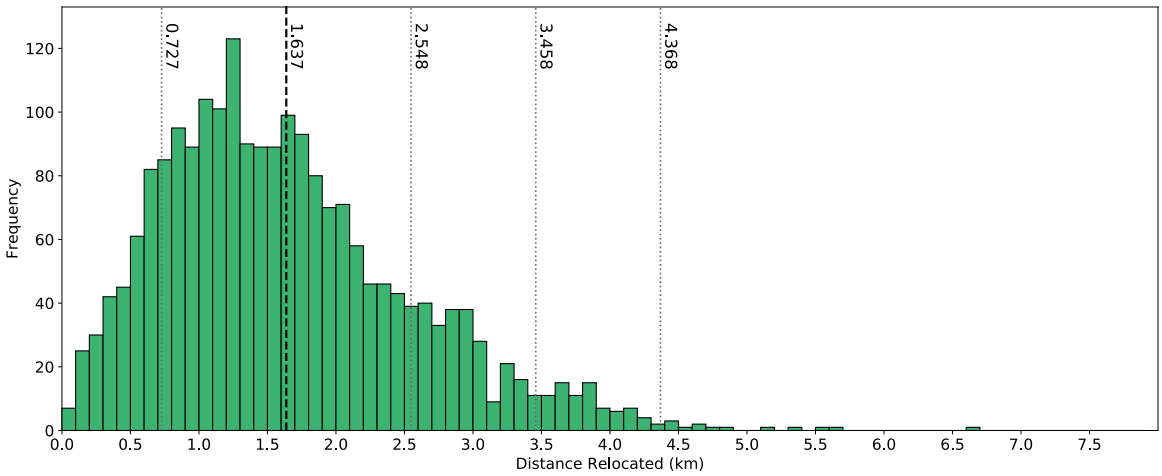

Figure 25: Histogram showing the frequency of events relocated using the IASP91 velocity model under a 0.2 RMS differential travel time residual parameter, as a function of distance between the original and relocated event location. The black dashed line denotes the average distance, while the dotted gray lines represent the standard deviations, up to 3σ.

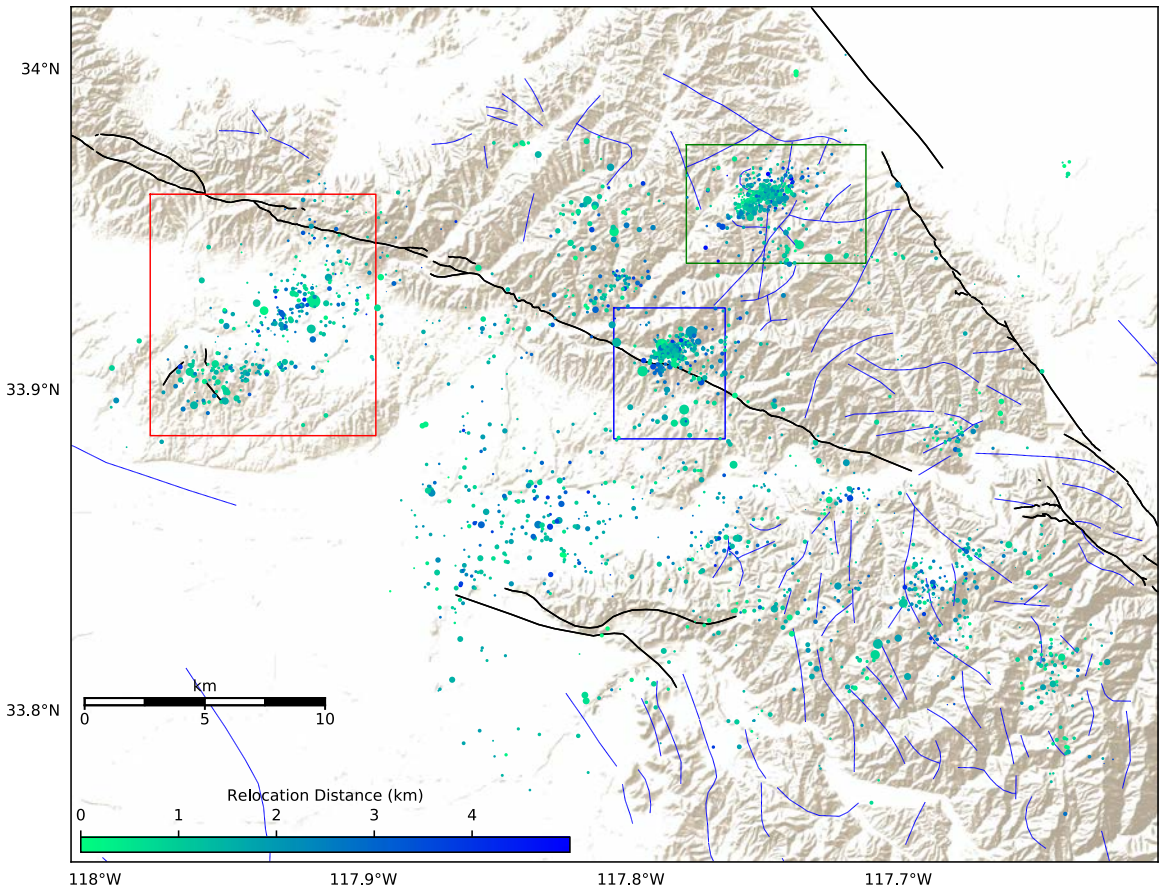

Figure 26: Map of relocated events, color coded by the distance each event was relocated compared to its original location, using the IASP91 velocity model with a 0.2 RMS differential travel time residual. The blue box outlines the Yorba Linda Sequence (Figure 55-i), the green box denotes the location of the Chino Hills Sequence (Figure 58-i), and the red box represents the La Habra Sequence (Figure 61-i).

The model relocation results revealed that there were a total of 357 clusters created. However, only 58 of these clusters contained more than eight events (Table 2). 1732 of the relocated events are within these 58 clusters, while the remaining relocated events are contained within clusters of $\leq$ two events. Figure 27 shows a map of all relocated events colored by whichever cluster they belong to, while Figure 28 depicts the centroid for each respective cluster, annotated with the cluster number. The largest of these clusters, Cluster 1, contains 301 events within it and represents one of three clusters forming the Chino Hills Sequence. The next largest cluster contains 230 events and is one of five clusters making up the Yorba Linda Sequence (Figure 27). The largest event within the La Habra Sequence, the 2014 La Habra Earthquake, is cataloged into a cluster of only 12 events, likely a major factor in its large location errors. The remaining clusters that were created are scattered throughout the area, with many of these clusters located throughout the Peninsular Ranges, east of the Peralta Hills Fault (Figure 27). Many of these clusters include only a small number of earthquakes.

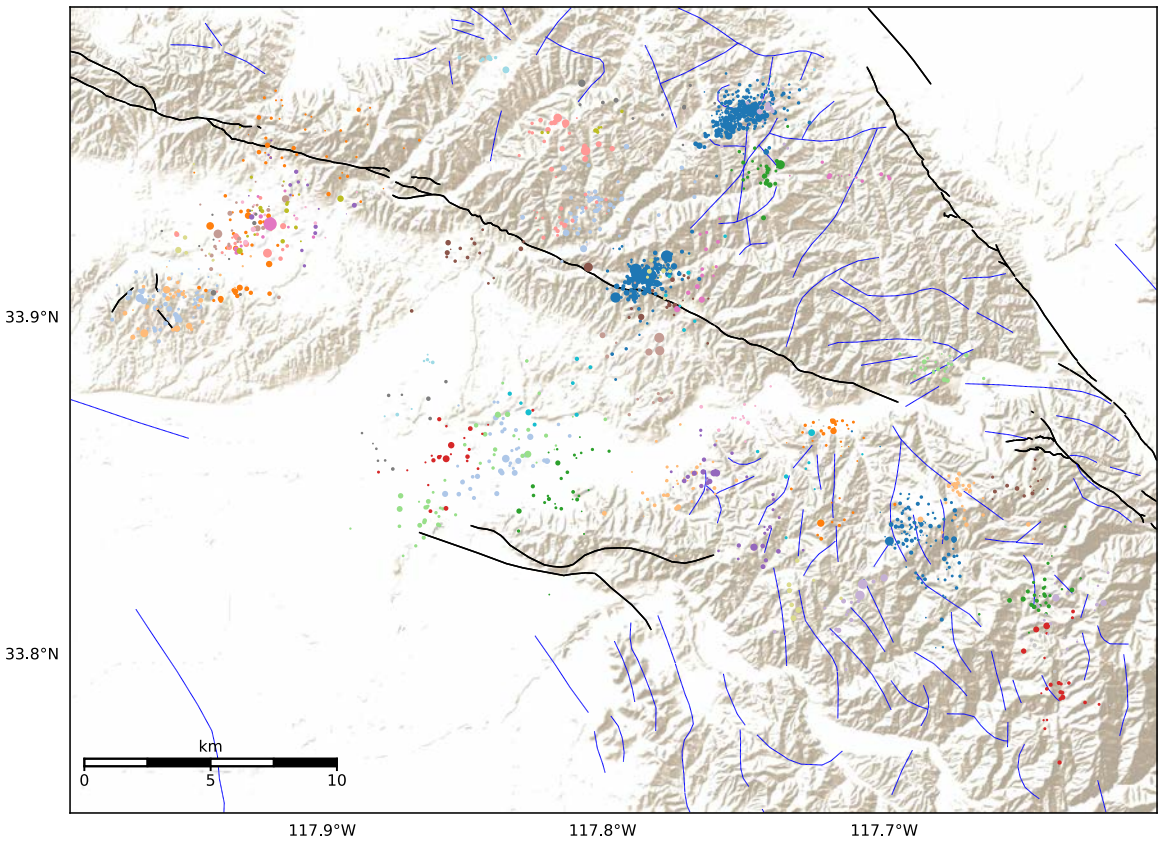

Figure 27: Map showing all major clusters of relocated events using the IASP91 velocity model with a 0.2 RMS differential travel time residual parameter. Only clusters that contained at least eight events are plotted. In total 58 different clusters are shown, while circulating through 20 different colors. Clusters that have the same color, but are at large distance from each other are unrelated. Cluster numbers and centroids are indicated in Figure 28.

Events within of each of the three sequences: The Yorba Linda Sequence, the Chino Hills Sequence, and the La Habra Sequence shown in Figures 7, 10, and 12, respectively, have become more condensed, particularly the Yorba Linda and Chino Hills sequences (Figure 26). As stated earlier, these two sequences are each dominated by a single cluster of events, with smaller clusters intermixed (Figure 27). These two sequences are not connected by seismicity between the two, thus bringing into question the presence of a single through-going fault connecting the two sequences. Both sequences also do not follow any known mapped fault traces with a similar orientation (Figure 26).

None of the clusters in the Chino Hills Sequence include the 2008 Chino Hills mainshock, which is relocated more east and at greater distance from those clusters. The

La Habra Sequence differs from the other two in that it retains its roughly linear orientation prior to relocation (Figure 26). This sequence is also dominated by many small sequences, in contrast to the Yorba Linda and Chino Hills Sequences (Figure 27). The events southwest of the Yorba Linda Sequence are now consolidated into multiple clusters (Clusters 6, 16, 18, 19, 43, 54 and 56) in an approximately 3 to 5 square kilometer area (Figure 27, Figure 28). It is interesting to note that these events have been relocated within the Richfield Oil Field, an area that has seen extensive seismicity as well as significant fluid injection, which may suggest that the events in this area are potentially anthropogenic earthquakes due to oil extraction (Hauksson et al., 2015) (Figure 27).

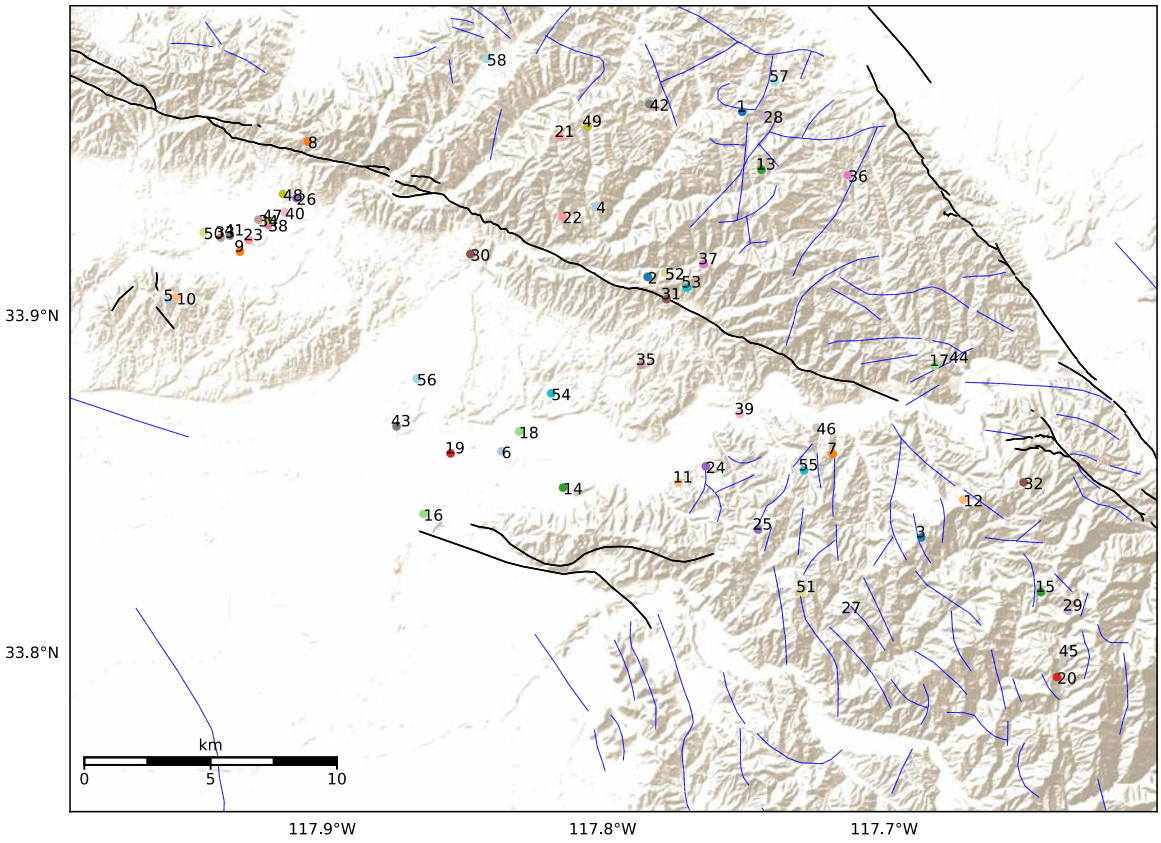

Figure 28: Map of the clusters of the IASP91 velocity model relocation results with a 0.2 RMS differential travel time residual parameter. Each cluster is shown by their respective cluster centroid location. Clusters are numbered according to size with 1 being the largest.

Figure 29 shows that the majority of the relocated event possessed RMS residual P-wave and S-wave differential times ranging from 0.2 to 0.3 seconds. Nearly all of the RMS

residual P-wave differential times for these events are distributed between 0 and 0.6 s, while the RMS residual S-wave differential times show, as expected, a much wider distribution, spanning from 0 s to 1.3 s (Figure 29). Figures 30 and 31 show these differential times for the RMS residual P-wave and S-wave respectively. If we compare the differential times for each event for both the RMS residual differential times to the location errors from Figures 33 and 34, we see that the events with a high horizontal and vertical error also possess larger differential times. These large errors correlate with these large differential times and the number of P- and S-wave differential times used to relocate these events.

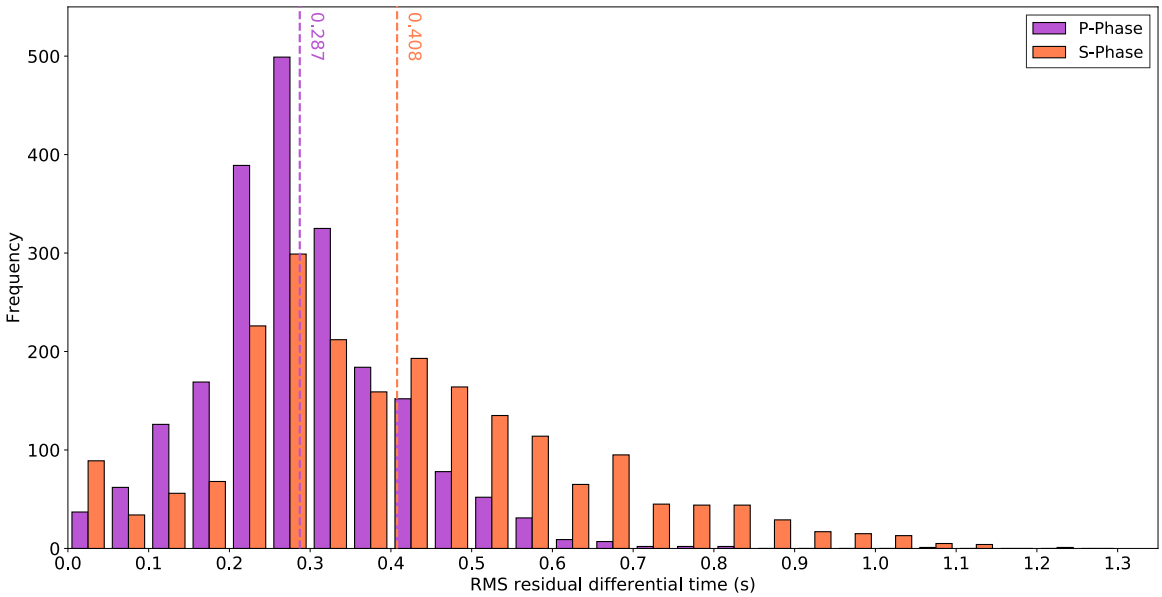

Figure 29: Histogram of the RMS residual differential times for the P-wave and S-wave for relocated events using the IASP91 velocity model under the 0.2 RMS differential travel time residual parameter. The purple dashed line denotes the average RMS P-wave residual differential time, while the orange dashed line denotes the average RMS S-wave residual differential time.

As stated previously, the relocations of the La Habra Sequence have relatively high RMS residual P- and S-wave differential times (Figure 30, Figure 31). In fact, the La Habra Sequence contains the highest RMS residual P- and S-wave differential times of all of the relocated events. The average RMS residual P-wave differential time for the La Habra Sequence is 0.38 s and the average for the RMS residual S-wave differential time is 0.71 s. The number of differential times used to relocate the events within the La Habra Sequence has an average of 127 for the P-wave and 199 for the S-wave. The 2014

La Habra mainshock has high RMS residual P- and S-wave differential times: 0.79 s and 1.08 s, respectively. If an event has high RMS residual P- and S-wave differential time values, then it is likely that it has been poorly located. The residual differential times are determined by the difference between the predicted arrival time and the measurement. The RMS residual differential time value is the root mean square of all residual differential times calculated in the GrowClust algorithm. The closer this value is to zero, the more robust this new location.

Contrarily, the Yorba Linda and Chino Hills Sequences both have smaller RMS residual P-wave differential times while only the Yorba Linda Sequence has a mixture of low and high RMS residual S-wave differential times (Figure 30, Figure 31). The Yorba Linda Sequence had average RMS residual P- and S-wave differential times of 0.25 s and 0.44 s, respectively. The average number of P- and S-wave differential timed used to relocate events within the Yorba Linda Sequence are 673 and 875, respectively. Three of the largest events (M 4.78, M 4.46, and M 4.45) within the Yorba Linda Sequence have low RMS residual P-wave differential times, but higher RMS residual S-wave differential times (Figure 30, Figure 31). This could be due to the S-wave arrival time predictions that are produced by this velocity model not being as good as the P-wave arrival times. Two of these events are located on each end of the Yorba Linda Sequence and one within the Sequence itself. The number of differential times used to relocate these events is quite large: 512, 944, and 1009 for the P-waves and 1398, 1773, and 1742 for the S-waves, respectively.

The Chino Hills Sequence has average RMS residual P- and S-wave differential times of 0.32 s and 0.31 s, respectively. The number of P- and S-wave differential times used for the relocation of these events is 629 and 1060, respectively. The clusters scattered throughout the northeastern region of the Peninsular Ranges consist of mainly low to medium RMS residual P-wave differential times and low RMS residual S-wave differential times. These clusters contrast with other clusters in the study area in that they have medium to high

location errors (Figure 30, Figure 31).

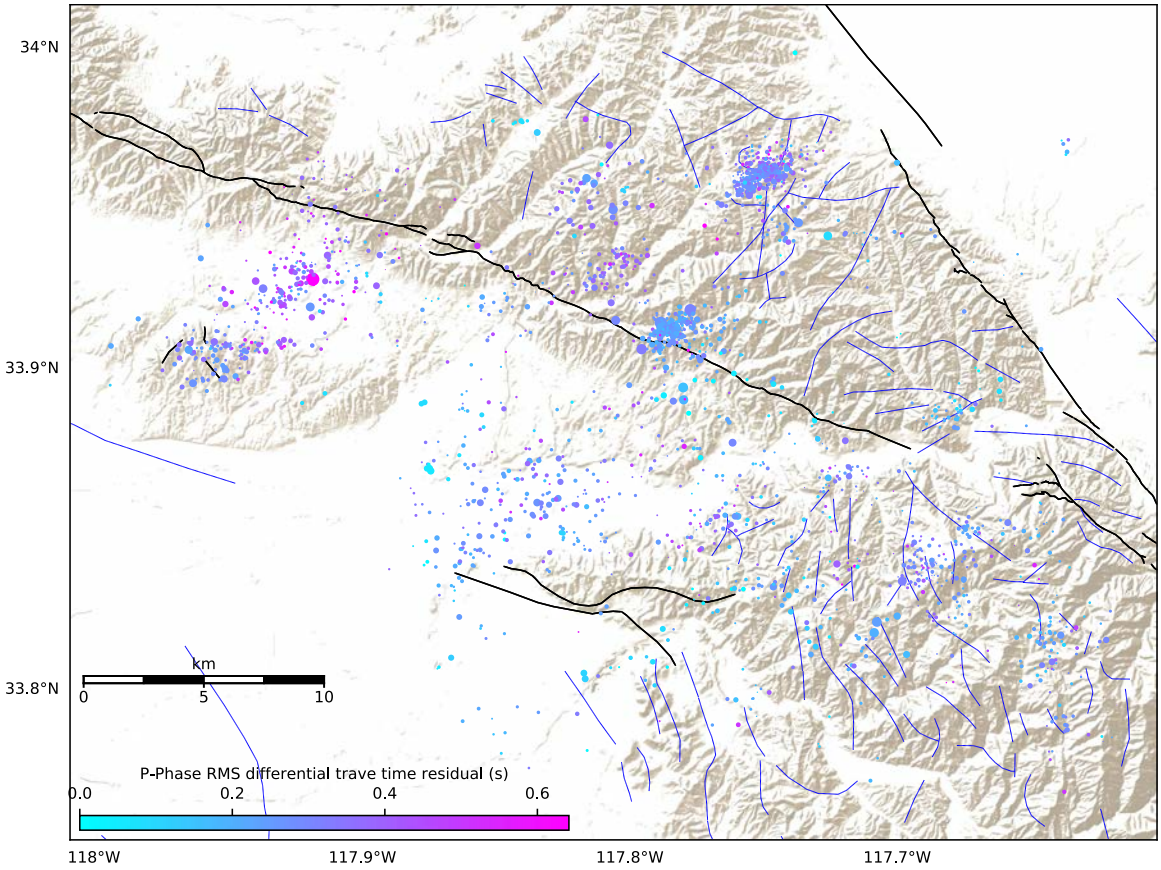

Figure 30: Map of relocated events color coded by their respective RMS residual P-wave differential time from the IASP91 velocity model relocation results under a 0.2 RMS differential travel time residual parameter.

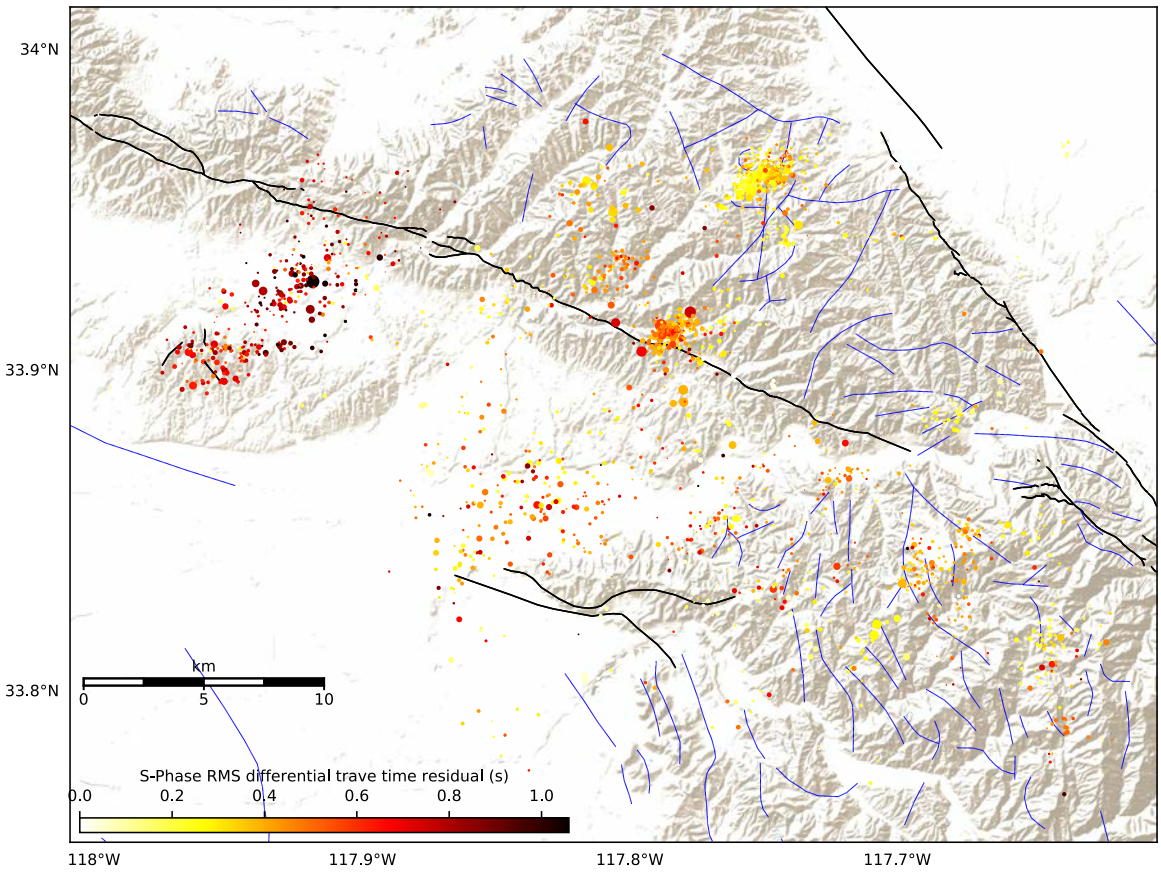

Figure 31: Map of relocated events color coded by their respective RMS residual S-wave differential time from the IASP91 velocity model relocation results under a 0.2 RMS differential travel time residual parameter.

Figure 32 shows the location errors for these relocation results. The majority of the events have a horizontal location error between 0.317 km and 1.260 km with an average horizontal error 0.789 km. In addition, the majority of events possess a vertical location error between 0.327 km and 1.190 km, while the average vertical error is 0.758 km. Figures 33 and 34 show these location errors based on the location of their respective events.

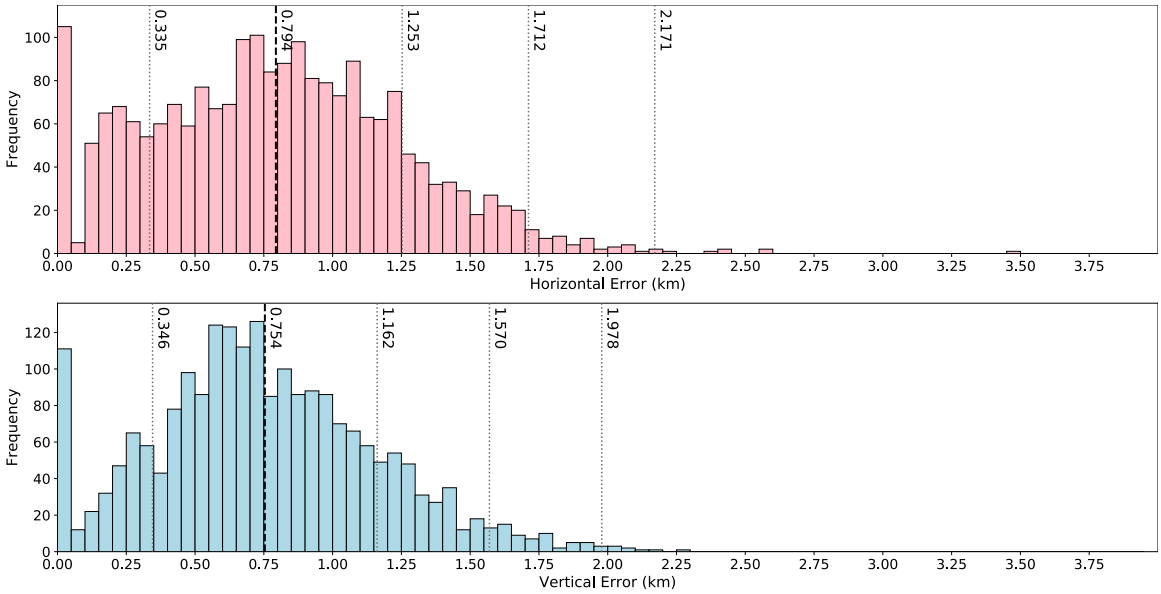

Figure 32: Histograms of the horizontal and vertical location errors for IASP91 velocity model relocation results under a 0.2 RMS differential travel time residual parameter.

As a result of the large number of arrival time measurements used and the relatively low RMS differential times for each event, the horizontal and vertical errors for The Yorba Linda and Chino Hills Sequences are minimal, with the Chino Hills Sequence with the smaller errors of the two (Figure 33, Figure 34). The large events within the Yorba Linda Sequence that had large RMS residual S-wave differential times contrast with the low location errors for these events.

The La Habra Sequence, however, possesses some of the highest horizontal and vertical errors throughout the region. Events making up the mixture of clusters towards the southwest end of the Yorba Linda Sequence show mainly of medium to high wave differential times with relatively high location errors, resulting in a reduced confidence in the quality of these locations, (Figure 33, Figure 34). Unexpectedly, the 2014 La Habra mainshock possesses unusually small horizontal and vertical location errors compared to the remainder of the La Habra Sequence.

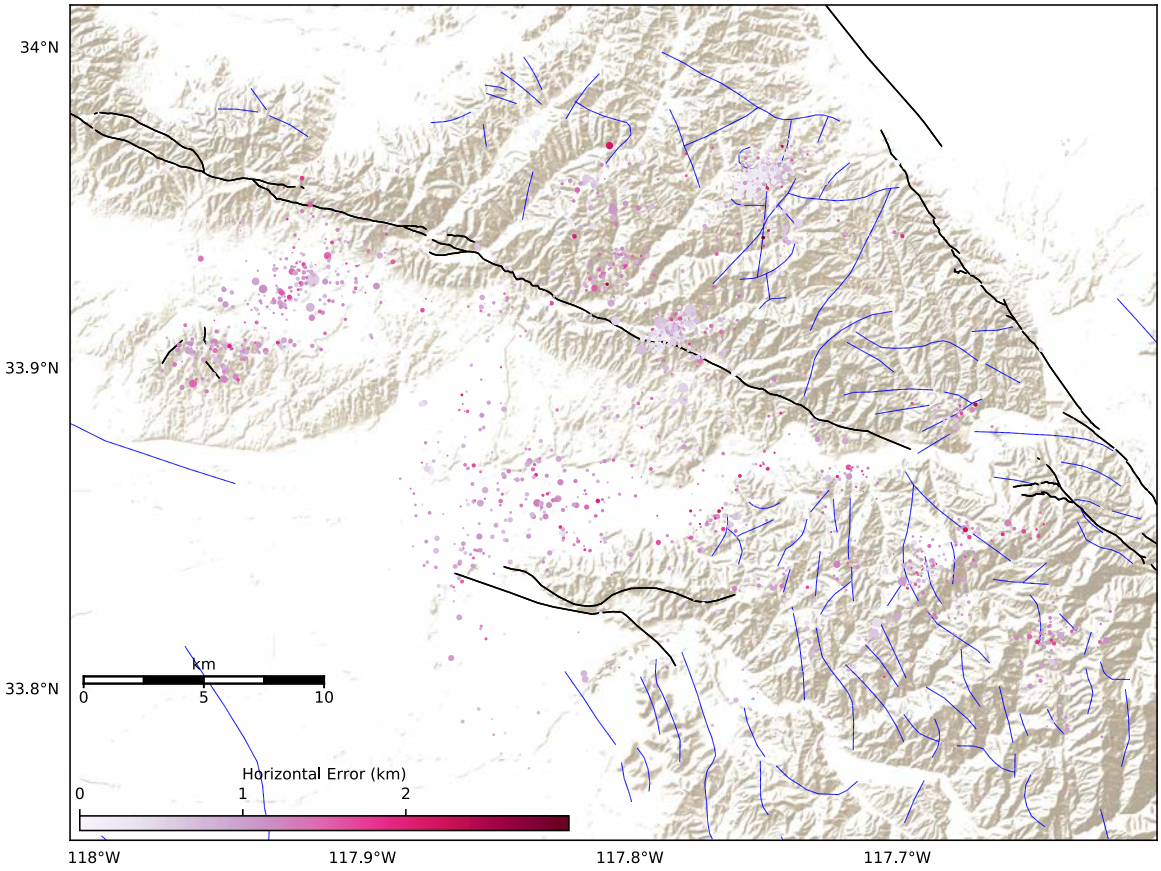

Figure 33: Map of the horizontal errors for of each relocated event using the IASP91 velocity model with a 0.2 RMS differential travel time residual parameter.

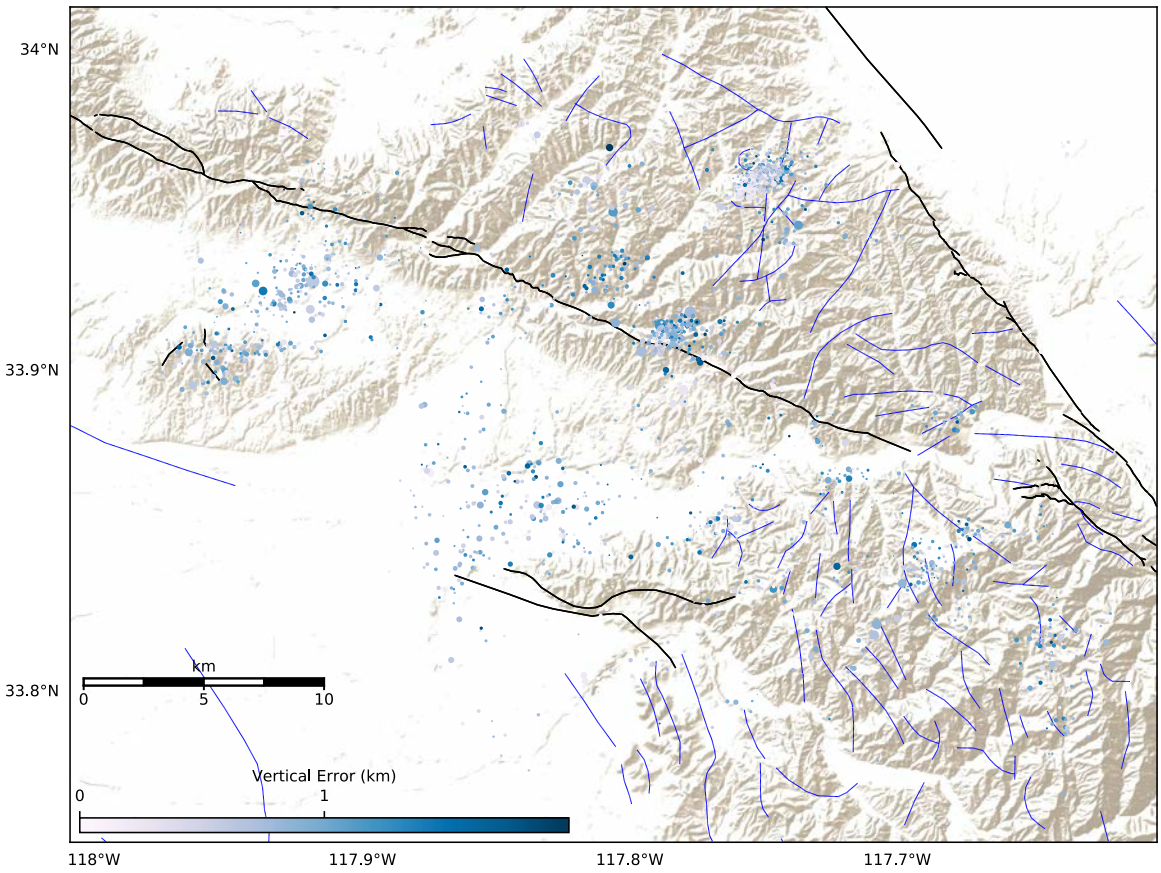

Figure 34: Map of the vertical errors associated of each relocated event using the IASP91 velocity model with a 0.2 RMS differential travel time residual.

3.1.2 Smoothed Southern California Velocity Model Relocation Results

The GrowClust algorithm successfully relocated 2143 events of the 4434 catalog events using the smoothed southern California velocity model under a 0.2 RMS differential travel time residual value. 93,121 event pairs were used to relocate the events plotted in Figure 26. The number of cross-correlations used to calculate the improved arrival times and thus the new locations for the P- and S-waves were 261,983 and 386,054, respectively (Table 2). Original locations and relocated locations of every event relocated with respect to depth using this velocity model and RMS differential travel time residual can be viewed in Appendix A: Figure 104 and Appendix B: Figure 107, respectively.

Figure 35 depicts the distance between the relocated and original location for each event, while Figure 36 shows these locations on a map colored by the distance. The

smoothed southern California model relocation distances have a wider distribution than that of the IASP91 model relocation results. The majority of the events were relocated between 0.733 and 2.650 km, with an average distance of 1.691 km (Figure 35). 69 events were relocated to distances more than 4.0 km from the original location, more than half of what is seen with the IASP91 model relocation results.

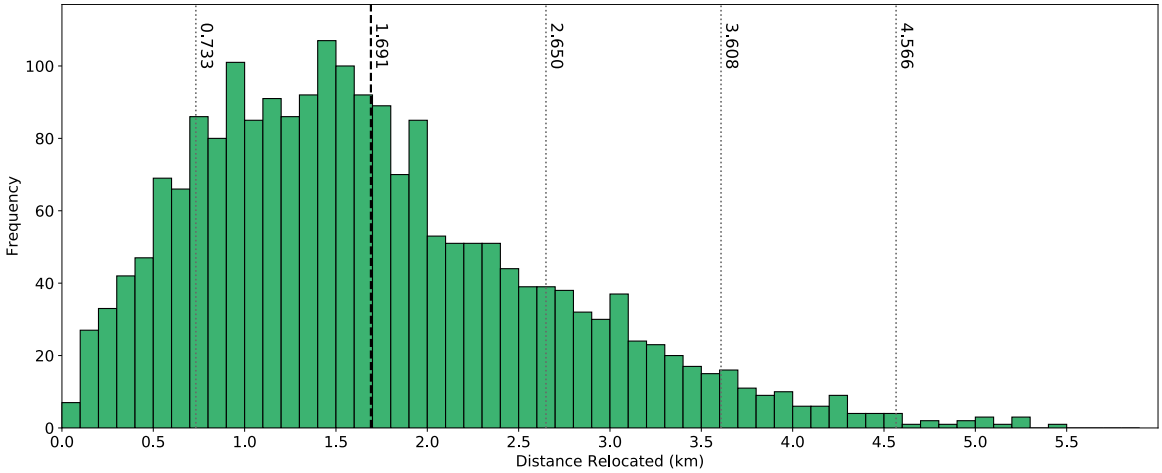

Figure 35: Histogram of the frequency of events relocated to their new locations using the smoothed southern California velocity model under a 0.2 RMS differential travel time residual parameter, as a function of distance between the original and relocated event location. The black dashed line denotes the average distance relocated, while the dotted gray lines represent the standard deviations, up to 3σ.

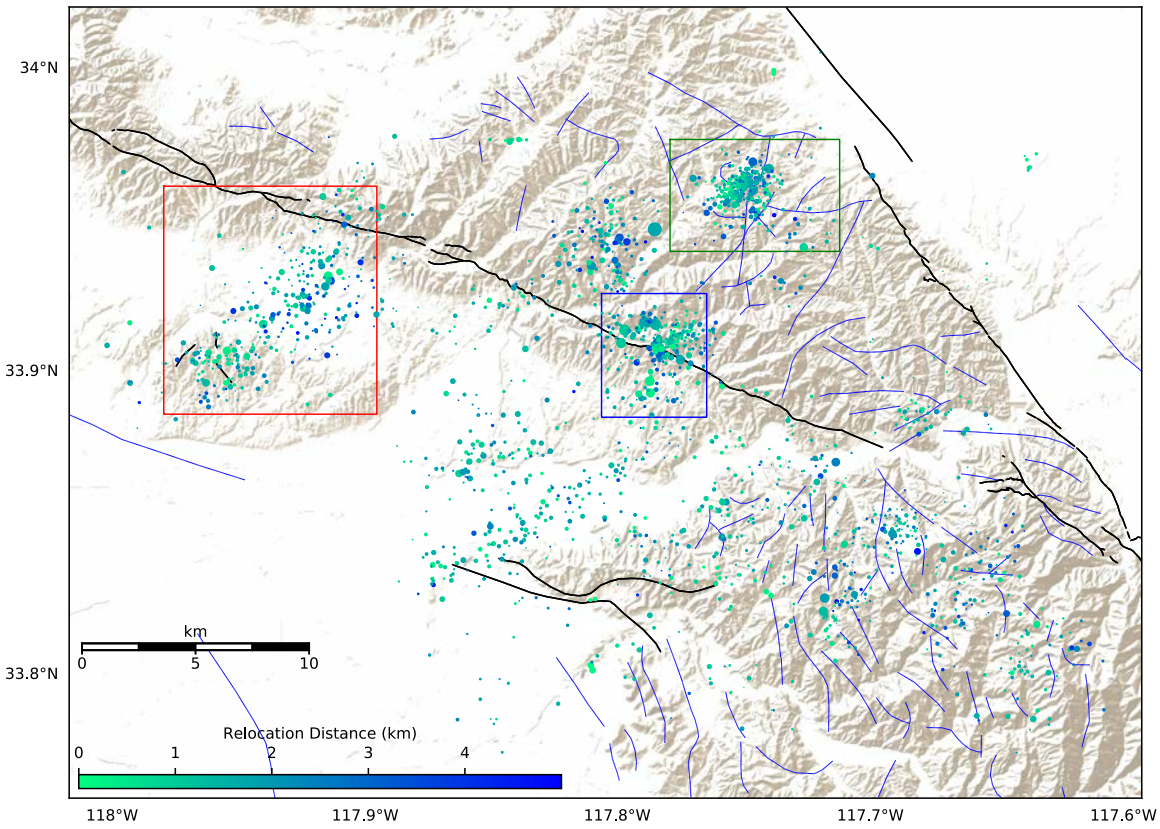

Figure 36: Map of relocated events color coded by the distance each event was relocated compared to its original location, using the smoothed southern California velocity model with a 0.2 RMS differential travel time residual. Boxes as in Figure 26.

The smoothed southern California velocity model relocated events have been consolidated into 340 clusters, however only 53 clusters contained more than eight events (Table 2). Of the 2143 events that were relocated, only 1725 events were assembled into these 53 events. These clusters are plotted in Figure 37. There are considerable differences between the cluster shapes of these results as compared to the IASP91 model relocated clusters, as discussed later.

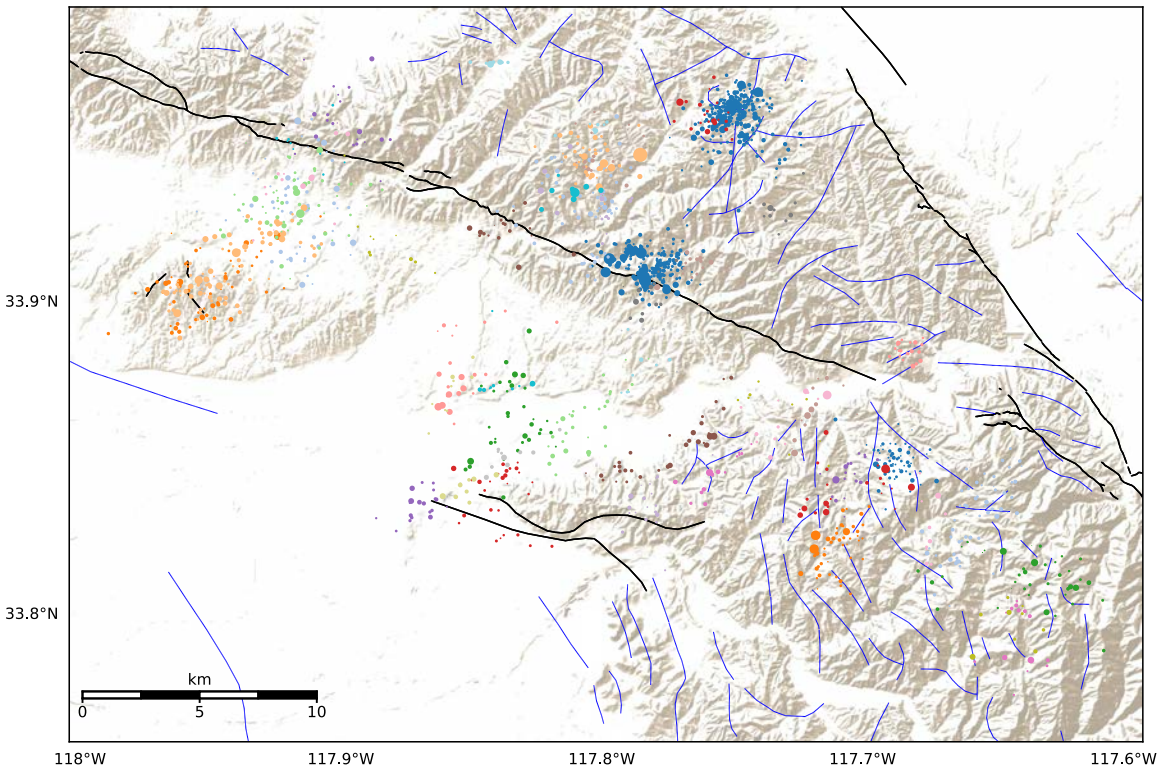

Figure 37: Map showing all major clusters of relocated events using the smoothed southern California velocity model with a 0.2 RMS differential travel time residual parameter. Only clusters that contained at least eight events are plotted. In total there are 53 different clusters shown, while circulating through 20 different colors. Clusters that have the same color, but are at large distance from each other are unrelated. Cluster centroids and cluster numbers are shown in Figure 38.

The Yorba Linda Sequence is made up of three clusters, with the main difference between these relocations and the IASP91 model relocations that the primary cluster has been separated into two distinct trends of earthquakes, both of which are oriented in the same direction (Figure 37, Figure 38). The Chino Hills Sequence is consistent with the previous relocation results in that it still is composed of one major cluster and two minor clusters. However, the consolidation of these events along a linear trend has decreased (Figure 37, Figure 38). A considerable difference with the smoothed southern California velocity model relocations in relation to the IASP91 velocity model relocation results is that the 2008 Chino Hills mainshock has been successfully relocated. However, it is not situated within any of the clusters that make up the Chino Hills Sequence. Rather, it is contained within Cluster 11, which just west-southwest from the the Chino Hills

Sequence, with some of these events within Cluster 11 identified as aftershocks based on their time of occurrence with respect to the Chino Hills mainshock. As was the case for the IASP91 velocity model relocation results, the smoothed southern California model relocations show no definitive connection between the Yorba Linda and Chino Hills Sequences.

The La Habra Sequence now includes seven clusters of similar sizes, each making up a segment of the overall Sequence, with slight overlap (Figure 37, Figure 38). These clusters have become more aligned along a northeast-southwest oriented trend, in comparison to the previous relocation results. The noticeable gap that was present within the La Habra Sequence in the previous results has been filled in slightly. Unlike the IASP91 model relocations, the 2014 La Habra mainshock was not relocated successfully.

Certain clusters throughout the region possess similar locations to the prior relocation results (Figure 37). Significantly different are Clusters 13, 15, 17, 20, 24, 41, 46, 47 and 48 (Figure 38). These clusters, located southwest from the Yorba Linda Sequence, have consolidated along two linear alignments with a similar orientation to the Yorba Linda Sequence. The alignment of these intermixed clusters could indicate that there are two geological structure causing the seismicity in this area (Figure 37). These clusters appear to extend from the Yorba Linda Sequence, potentially suggesting the existence of a through-going fault connecting these structures to the Yorba Linda Sequence. Unfortunately, the lack of events connecting these clusters makes this interpretation uncertain.

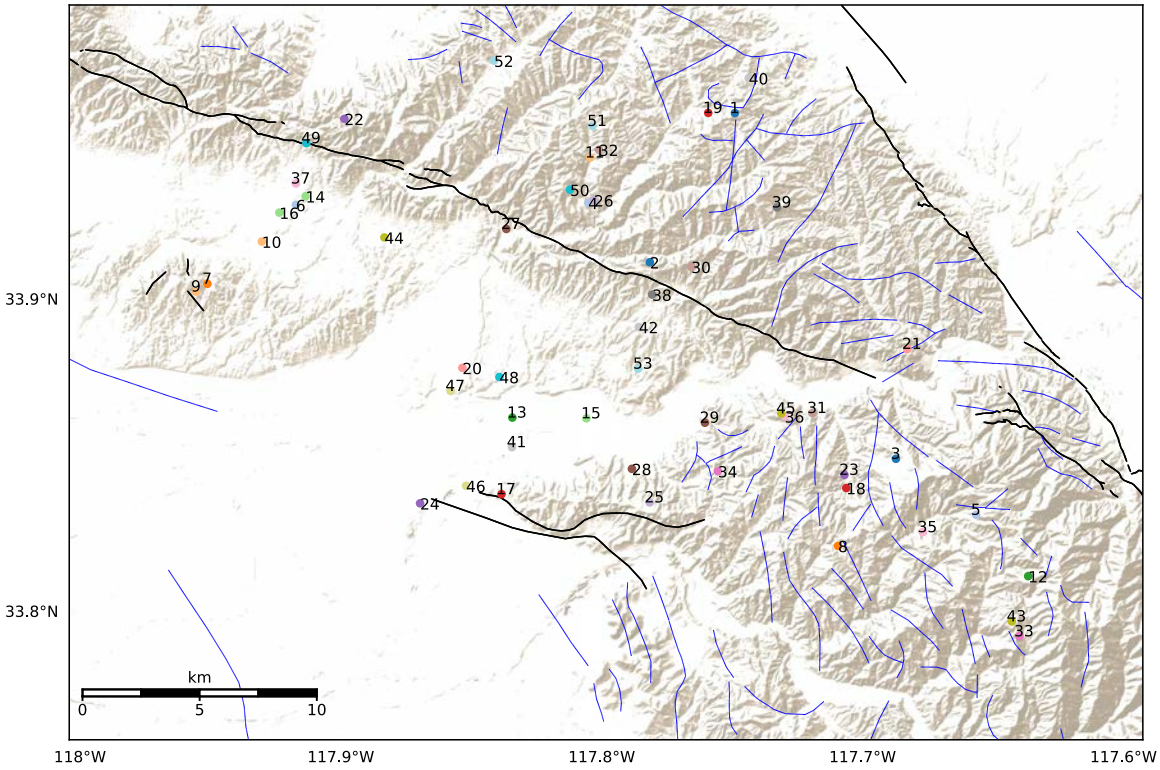

Figure 38: Map of the clusters of the smoothed southern California velocity model relocation results with a 0.2 RMS differential travel time residual parameter. Each cluster is shown by their respective cluster centroid location. Clusters are numbered according to size with 1 being the largest.

The RMS residual P- and S-wave differential times for the smoothed southern California velocity model relocation results show a similar distribution to that of the IASP91 model relocation results (Figure 39). There are more events that have smaller RMS residual P-wave differential time residuals than that of the previous results, with the majority of the differential times spanning from 0.2 s to 0.4 s. Figure 40 and 41 show each event colored by their respective RMS residual P- and S-wave differential time residuals. The 2008 Chino Hills mainshock, in particular, possesses large RMS residual P- and S-wave differential values.

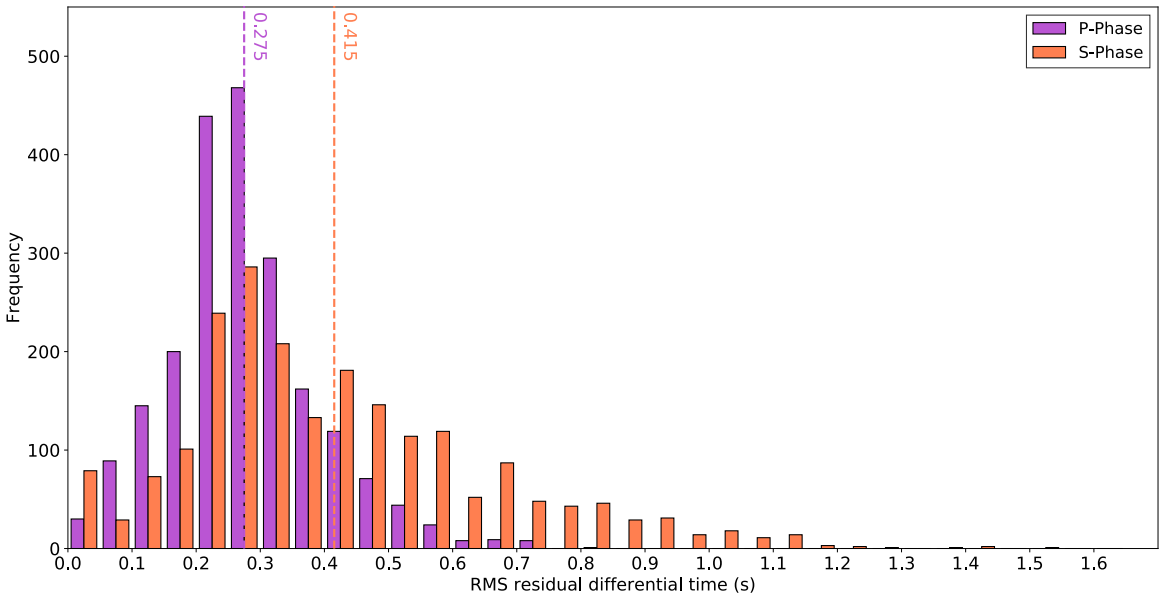

Figure 39: Histogram of the RMS residual differential times for the P- and S-wave for relocated events using the smoothed southern California velocity model under the 0.2 RMS differential travel time residual parameter. The purple dashed line denotes the average RMS P-wave residual differential time while the orange dashed line denotes the average RMS S-wave residual differential time.

Overall, the Yorba Linda Sequence had average RMS residual P- and S-wave differential times of 0.25 s and 0.44 s, respectively. An interesting feature is the two trends making up the main cluster of the Yorba Linda Sequence. The left conglomeration contains higher RMS residual P- and S-wave differential times than the right (Figure 40, Figure 41). Due to these high errors, the relocations of these events may be inaccurate, leading to questioning the validity of two separate collections of the Yorba Linda Sequence as opposed to one. The linear alignment of events southwest from the the Yorba Linda Sequence contains relatively small RMS residual P- and S-wave differential times (Figure 40, Figure 41). These low differential times imply that the locations of these events are better constrained than was seen with the IASP91 velocity model relocation results.

The Chino Hills Sequence consists mainly of small RMS residual P- and S-wave differential times, with averages of 0.28 s and 0.30 s, respectively (Figure 40, Figure 41). The number of P- and S-wave differential times used to relocate these events is 673 and 1074, respectively. Both of these values are higher than those for the IASP91 velocity

model relocation results. The Chino Hills Earthquake does not share similar RMS differential times as the rest of the sequence, nor does it have similar times as those events that it was clustered with (Figure 40, Figure 41).

While the smoothed southern California mode results show that the La Habra Sequence does have lower RMS residual P- and S-wave differential times than the IASP91 model relocations, they still possess characteristically high RMS residual P- and S-wave differential time residuals compared to the other relocations (Figure 40, Figure 41). These high RMS residual P- and S-wave differential times (0.38 s and 0.71 s, respectively) are likely related to the small number of P- and S-waves used for the relocation: 127 P-wave and 199 S-wave differential times.

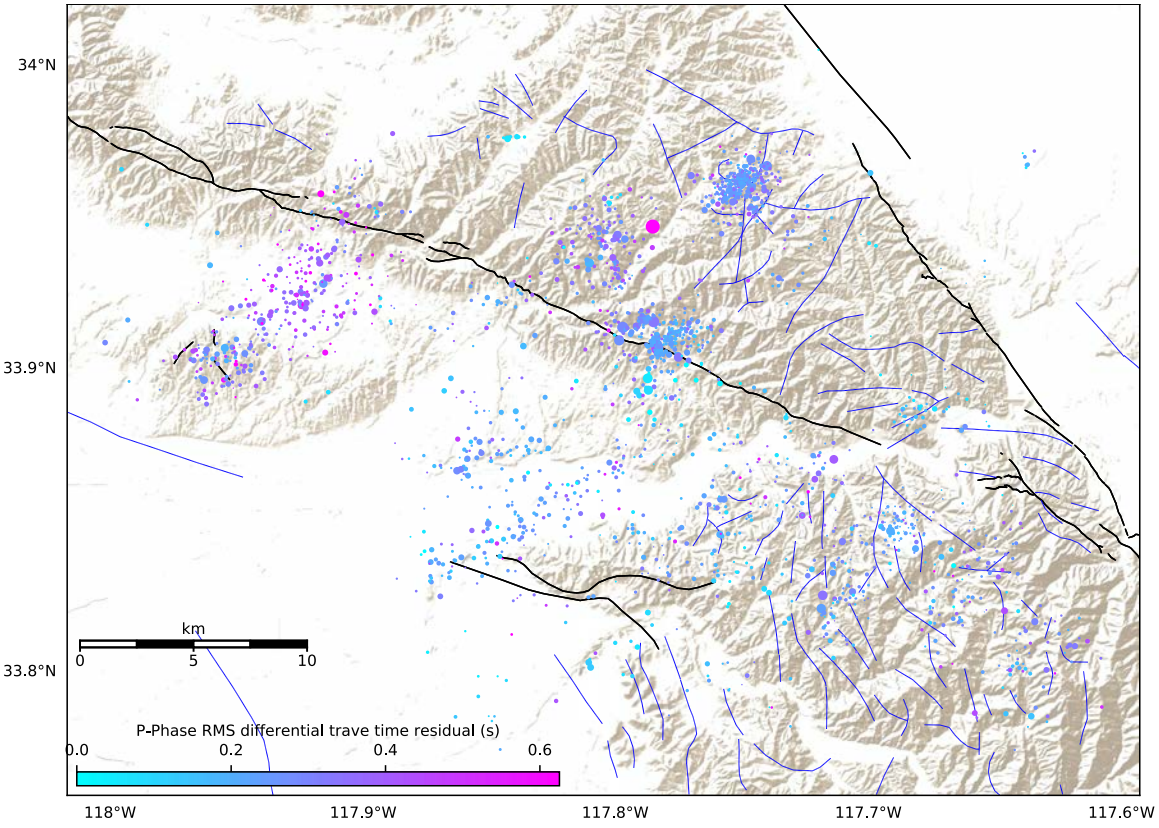

Figure 40: Map of relocated events color coded by their respective RMS residual P-wave differential time from the smoothed southern California velocity model relocation results under a 0.2 RMS differential travel time residual parameter.

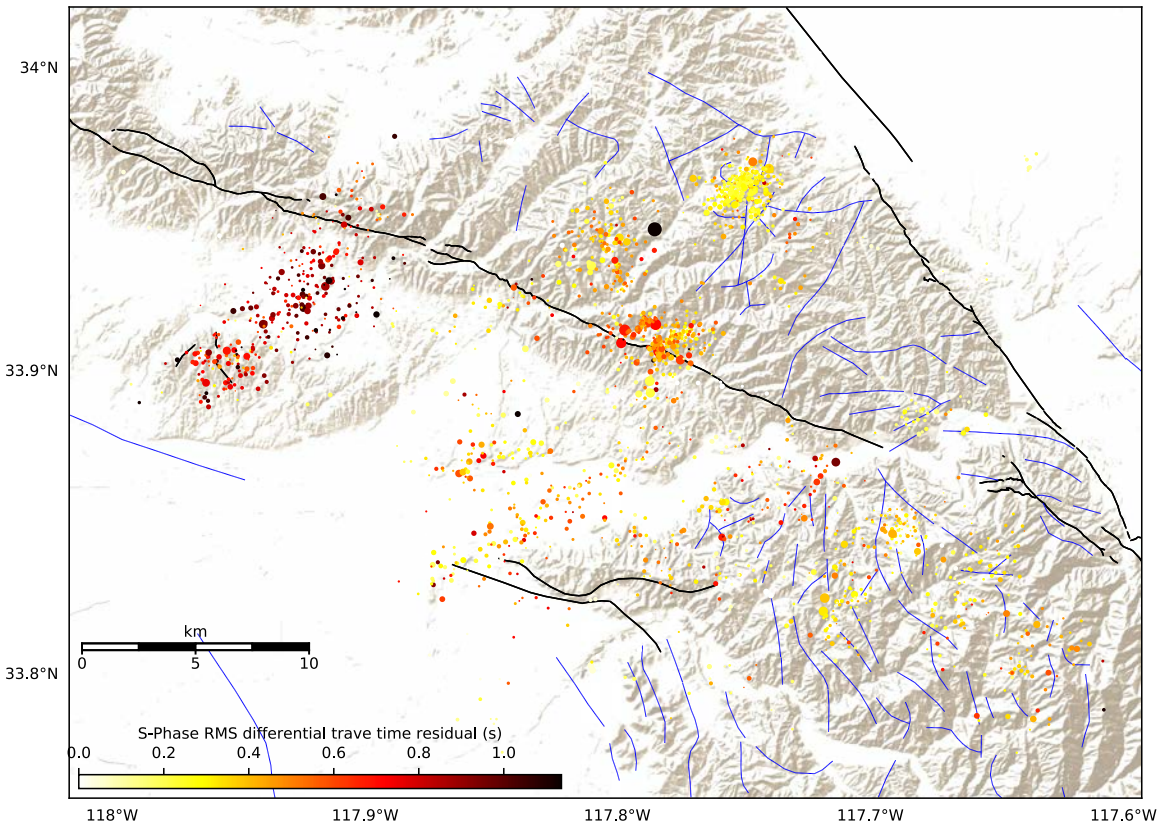

Figure 41: Map of relocated events color coded by their respective RMS residual S-wave differential time from the smoothed southern California velocity model relocation results under a 0.2 RMS differential travel time residual parameter.

In conjunction with the number of P- and S-wave differential times used as well as the RMS residual P- and S-wave differential times for each event, the location errors for each event are also considered an important component in the assessment of the quality of these relocations. Figure 29 shows that the majority of the relocated events possessed RMS residual P- and S-wave differential times ranging from 0.2 to 0.3 seconds. Most of the RMS residual P-wave differential times are distributed between 0 and 0.6 s while the S-wave differentials possess a much wider distribution, spanning from 0 s to 1.3 s (Figure 29). Figures 30 and 31 show these differential times for the RMS residual P- and S-wave respectively.

The smoothed southern California velocity model relocation results possess higher horizontal errors than the IASP91 velocity model results, with an average of 0.798 km

(Figure 32). The majority of the events have a horizontal location error between 0.340 km and 1.256 km. On the other hand, the vertical errors from these results are lower compared to those for the IASP91 velocity model. The average vertical location error for these results is 0.749 km, while a majority of the events have a vertical error between 0.339 km and 1.160 km.

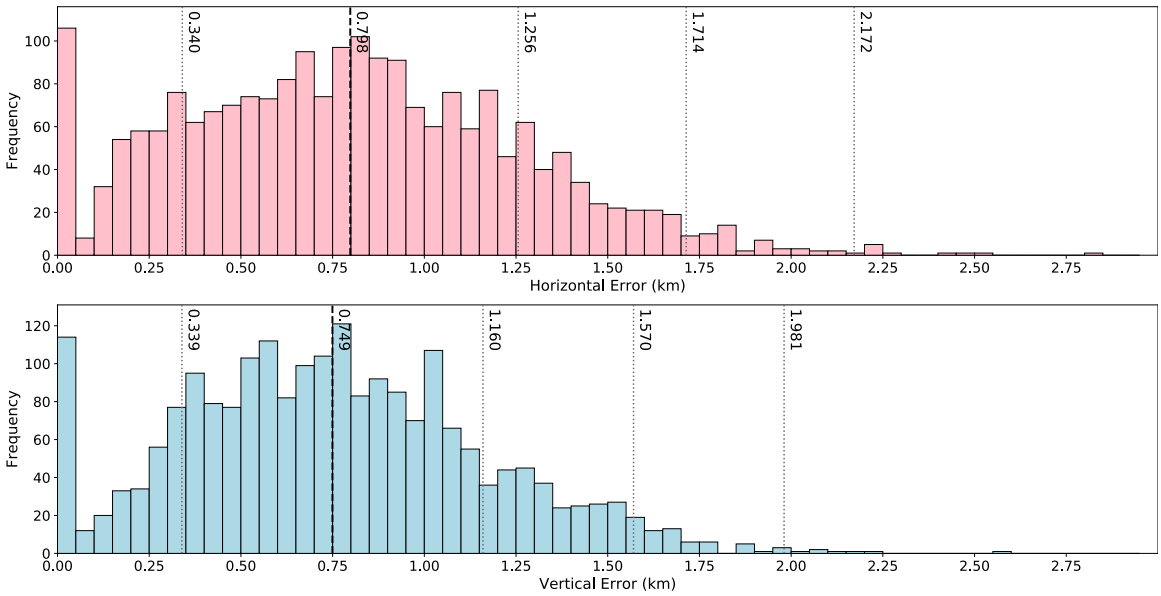

Figure 42: Histograms showing the horizontal and vertical location errors for smoothed southern California velocity model relocation results under a 0.2 RMS differential travel time residual parameter.

Along with the low RMS differential times and the large number of arrival time measurements used for the Yorba Linda Sequence, this sequence also contains mainly low location errors. The location of these events potentially indicate the presence of a fault structure here (Figure 36). The large magnitude events within the western collection of events do possess somewhat higher location errors. The same can be said about their vertical errors. Many of the relocated events within the Yorba Linda Sequence possess smaller vertical errors than the remainder of the relocations throughout the area. Unlike the horizontal errors, the large events within the western arrangement do have considerably higher vertical errors. One of these events, the M 4.46 earthquake, has an even higher vertical error (1.62 km) than the rest of this cluster.

Considering the large number of arrival times used for the relocation of the events

within the Chino Hills Sequence, it should come as no surprise that the Chino Hills Sequence possesses significantly smaller location errors than most of the relocations in these results (Figure 43, Figure 44). The 2008 Chino Hills mainshock, however, has extremely small horizontal and vertical errors, contrasting with the low number of P- and S-wave differential times used to relocate it: 44 and 18, respectively.

As expected, the La Habra Sequence contains some of the highest location errors throughout the smoothed southern California velocity model relocation results (Figure 43, Figure 44). The higher horizontal and vertical errors appear to be situated within the middle southeastern edge of the La Habra Sequence. These events with the higher location errors are not isolated to one single cluster, rather they span multiple clusters (Figure 37, Figure 43, Figure 44).

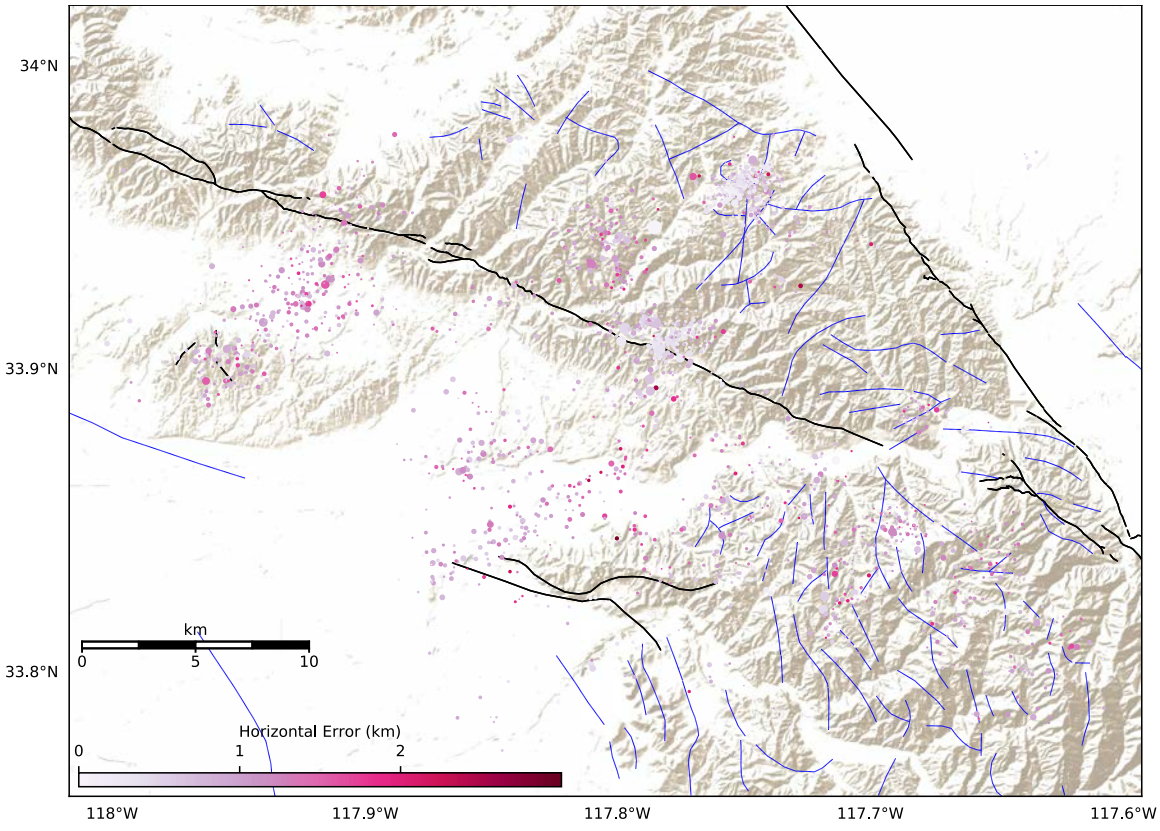

Figure 43: Map of the horizontal errors for of each relocated event using the smoothed southern California velocity model with a 0.2 RMS differential travel time residual parameter.

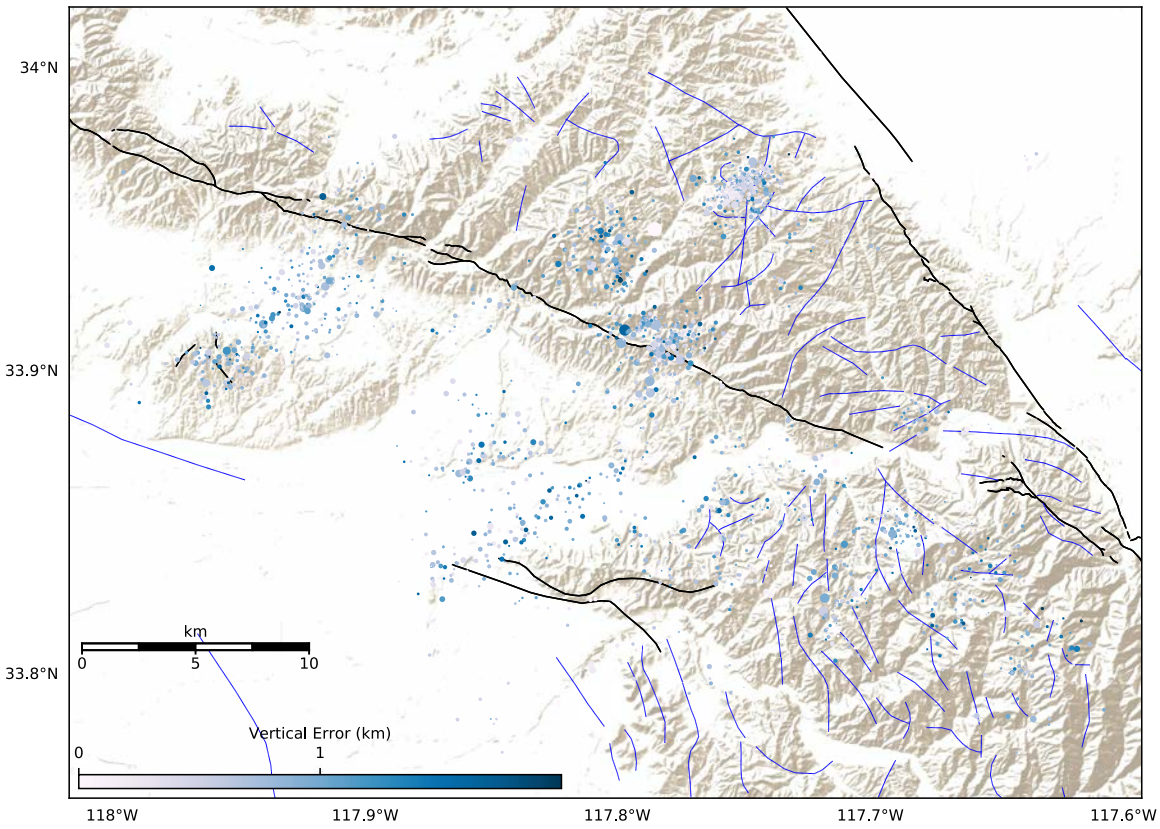

Figure 44: Map of the vertical errors for of each relocated event using the smoothed southern California velocity model with a 0.2 RMS differential travel time residual parameter.

3.1.3 Los Angeles Basin Velocity Model Relocation Results

The relocation results using the LA Basin velocity model with a 0.2 RMS differential travel times residual resulted in 2197 events being successfully relocated. The number of successful relocations using this model is higher than that seen in the other two velocity models (Table 2). The GrowClust algorithm used 101,382 event pairs to relocate the catalog events (Table 3). The total number of P- and S- wave differential times that were used were 285,314 and 415,189, respectively (Table 3). Original locations and relocated locations of every event relocated with respect to depth using this velocity model and RMS differential travel time residual can be viewed in Appendix A: Figure 105 and Appendix B: Figure 108, respectively.

Figure 45 shows the distribution of the distance that events were relocated from their

original location. Figure 46 shows the relocated events color coded by this distance. These model relocation results show an overall tighter consolidation of events within each of the major sequences than the other two model relocations. The average relocation distance for all of these events is 1.714 km, while the distribution of the relocated distances is smaller than that of the prior two model relocation results Figure 45). Despite this smaller distribution, the majority of events were relocated within a wider range of distances, between 0.731 and 2.697 km. In total, only 47 events were relocated at distances larger than 4.0 km, a smaller amount than the smoothed southern California velocity model relocations, but larger than that of the IASP91 velocity model relocation results.

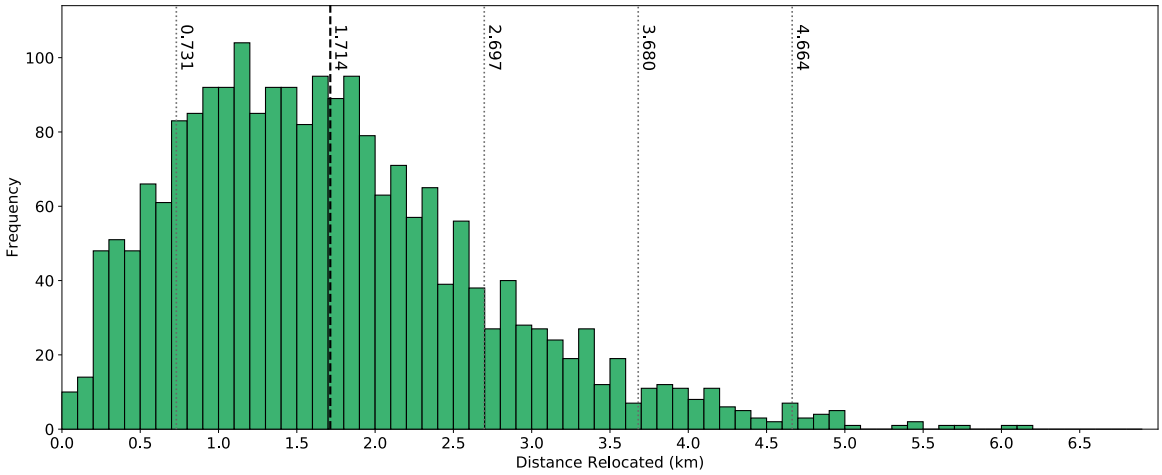

Figure 45: Histogram of the frequency of events relocated to their new locations using the LA Basin velocity model under a 0.2 RMS differential travel time residual parameter as a function of distance between the original and relocated event location. The black dashed line denotes the average distance relocated, while the dotted gray lines represent the standard deviations, up to 3σ.

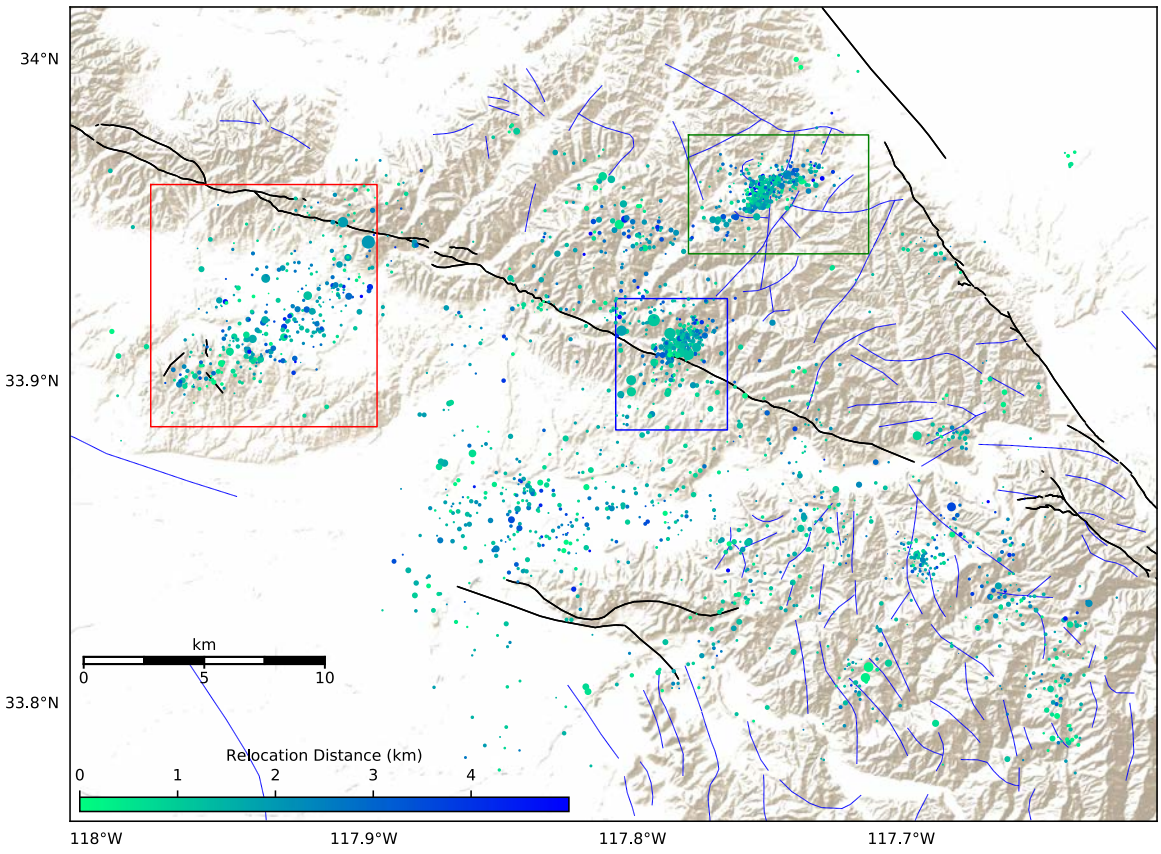

Figure 46: Map of relocated events color coded by the distance each event was relocated compared to its original location, using the LA Basin velocity model with a 0.2 RMS differential travel time residual. The blue box outlines the Yorba Linda Sequence (Figure 55-iii), the green box denotes the location of the Chino Hills Sequence (Figure 58-iii), and the red box represents the La Habra Sequence (Figure 61-iii).

The GrowClust algorithm compiled all of the relocated events into 348 clusters. However, only 52 of these clusters contained eight or more events (Table 2). Of the 2197 relocated events, only 1758 are compiled into these 52 clusters, more than for both of the previous velocity model relocations. The location of these clusters is plotted in Figure 47), while the location of the cluster centroid and the cluster identification number are shown in Figure 48). The Chino Hills Cluster and the Yorba Linda Sequence contain the largest and second largest clusters, an observation seen for all velocity model relocation results. The La Habra Sequence now possesses the third largest cluster, which is only observed for the relocation results for this velocity model (Figure 48). In the previous relocation results, the third largest cluster was located within the northeastern region of the Peninsular Ranges (Figure 47, Figure 48).

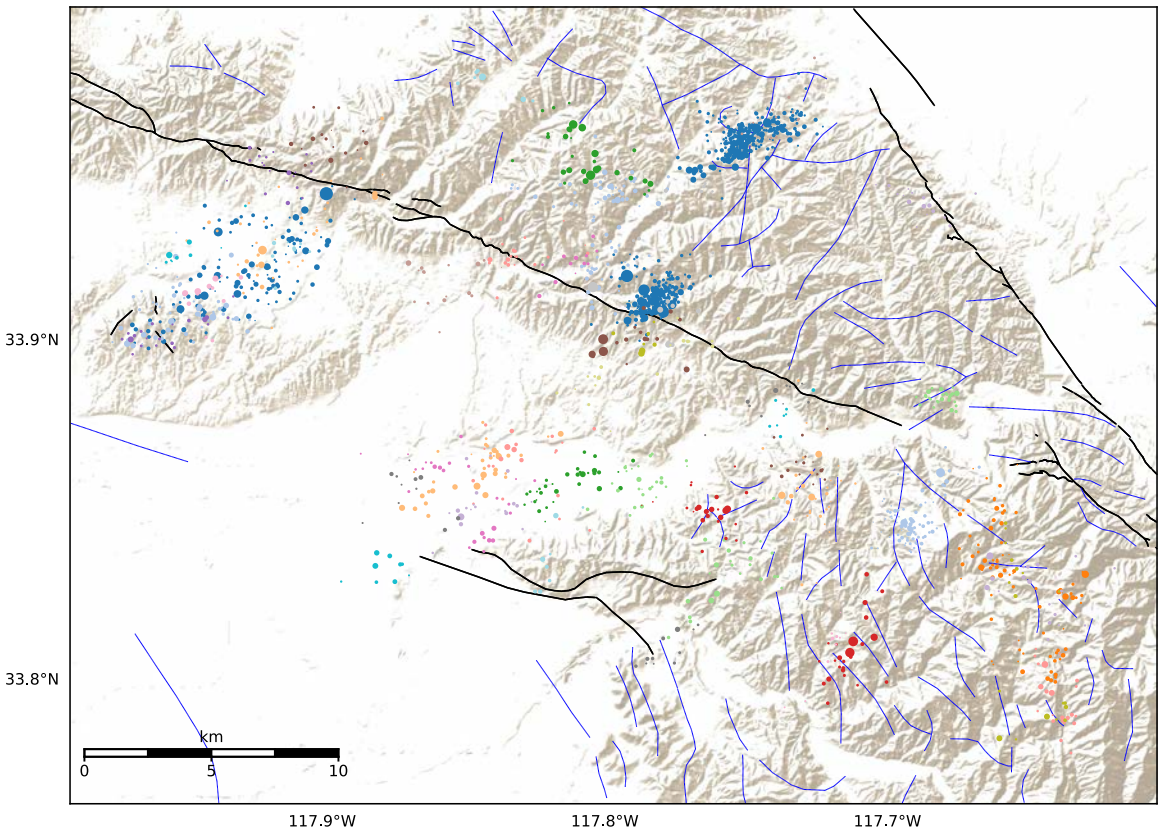

Figure 47: Map of all major clusters of relocated events using the LA Basin velocity model with a 0.2 RMS differential travel time residual parameter. Only clusters that contained at least eight events are shown. In total 52 different clusters are shown, while circulating through 20 different colors. Clusters that have the same color, but are at large distance from each other are unrelated.

The Yorba Linda Sequence displays a similar single linear alignment as was seen with the IASP91 velocity model relocation results (Figure 47, Figure 48). The events making up this sequence have been assembled into five different clusters, one of these containing the vast majority of these events. Of the larger earthquakes within this sequence, the M 4.14 earthquake is part of Cluster 40 as opposed to the primary cluster. While the cluster centroid of Cluster 40 is close to the centroid of Cluster 2, the location of this large event is a considerable distance away from the centroid and overall sequence (Figure 47, Figure 48). In addition to the M 4.14 earthquake, the M 4.78 earthquake, which is part of the primary cluster of the Yorba Linda Sequence, is also at noticeably great distance from the remainder of the cluster (Figure 47).

Unlike the prior two relocation results, the Chino Hills Sequence is now only composed

of two clusters, one of them significantly larger than the other. The shape of the Chino Hills Sequence has expanded along its trend orientation, while maintaining its condensed event distribution (Figure 47). The 2008 Chino Hills Earthquake is no longer one of the events that was relocated, unlike was the case for the smoothed southern California model relocations.

The La Habra Sequence now has a more consolidated shape along its trend. As previously mentioned, it contains the third largest cluster, assembled of 130 events, extending throughout the entire sequence (Figure 47). As was seen with the IASP91 velocity model relocations, these results include the 2014 La Habra mainshock. However, unlike the IASP91 velocity model relocation results, the 2014 La Habra Earthquake is a part of the largest cluster (Figure 47). Aside from the largest cluster, the La Habra Sequence also includes six other clusters, of varying size (Figure 48).

The events making up the clusters 10, 12, 15, 21, 24, 32, 33, 37, 48, and 51 are no longer situated in a linear fashion as was seen in the smoothed southern California velocity model relocations (Figure 47, Figure 48). These events have been relocated as a large round consolidation of events similar to that was observed in the IASP91 velocity model relocation results. The clusters located towards the southeast within the Peninsular Ranges have become more densely consolidated than what is seen in both of the previous models (Figure 47).

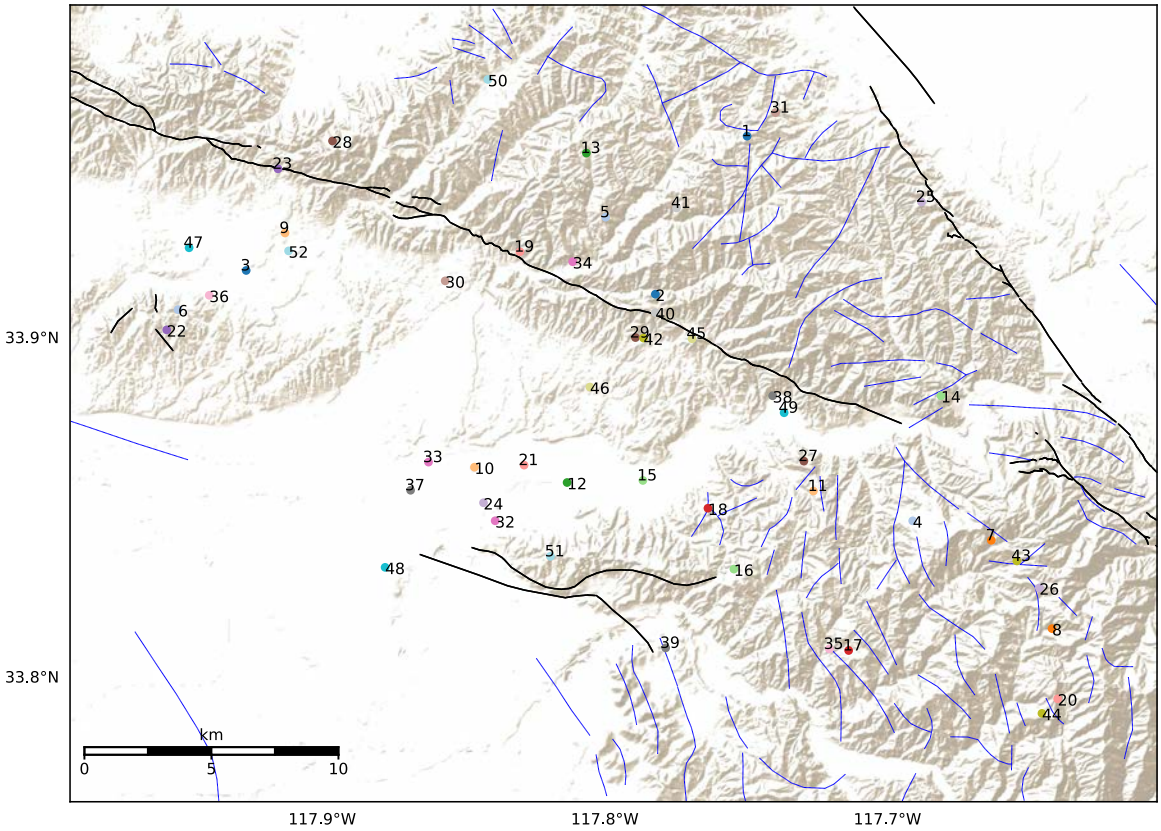

Figure 48: Map of the clusters of the LA Basin velocity model relocation results with a 0.2 RMS differential travel time residual parameter. Each cluster is shown by their respective cluster centroid location. Clusters are numbered according to size with 1 being the largest.

The distribution of the RMS residual P- and S-wave differential times for the LA Basin velocity model relocation results show a similar distribution to those seen in the prior two model results (Figure 49). The majority of the earthquakes have RMS residual P-wave differential times ranging from 0.2 to 0.35 km. Figures 50 and 51 have plotted events with their respective RMS residual P- and S-wave differential time values.

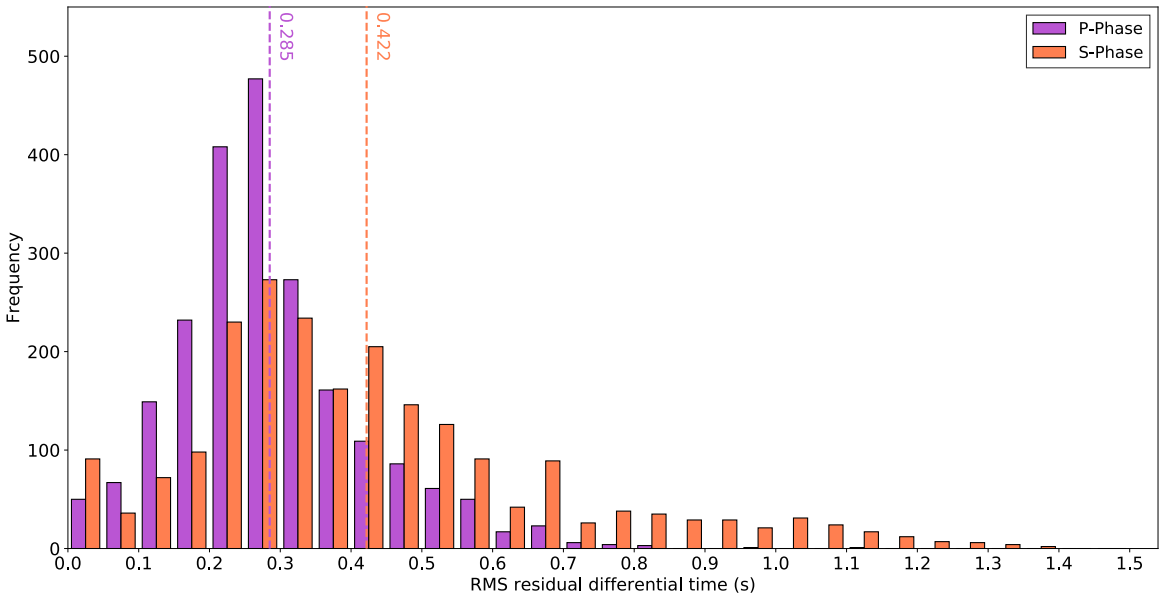

Figure 49: Histogram of the RMS residual differential times for the P- and S-waves for relocated events using the LA Basin velocity model under the 0.2 RMS differential travel time residual parameter. The purple dashed line denotes the average RMS P-wave residual differential time while the orange dashed line denotes the average RMS S-wave residual differential time.

As was seen in the prior two model relocation results, both the Yorba Linda and Chino Hills Sequences have low differential times for both the RMS residual P- and S-waves: 0.23 s and 0.37 s, respectively (Figure 50, Figure 51). The GrowClust algorithm used 679 P-wave differential times and 873 S-wave differential times to relocate the events within this sequence. A notable observation is the M 4.14 event located just outside of the Yorba Linda Sequence. As discussed previously, this event was not a part of the main cluster of the Yorba Linda Sequence, rather it was contained within a smaller cluster. If we examine the RMS residual P- and S-wave differential times of this event, we can see that this event has higher values than those of the main cluster of the Yorba Linda Sequence (Figure 50, Figure 51). The M 4.78 earthquake, an event that is part of the primary cluster of the Yorba Linda Sequence, has a distinctly high RMS residual P-wave differential time (Figure 50). Unlike the M 4.14 event, the M 4.78 event has a plentiful number of P- and S-wave differential times used to relocate this event.

Similar to the other relocation results, the Chino Hills sequence contains some of the smallest RMS residual P- and S-wave differential times of all the relocation results

(Figure 50, Figure 51). The average RMS differential times for this sequence are both 0.27 s for the P-wave and S-wave. The number of P-wave and S-wave differential times used to relocate these events are 727 and 1148, respectively. These are the largest number of differential times used out of the three velocity model relocation results for the 0.2 RMS differential travel time parameters. It therefore is as expected that these relocation results also contain the smallest average RMS residual P- and S-wave differential times of the three velocity model relocation results.

The La Habra Sequence again possesses distinctly high RMS residual P- and S-wave differential times, as was seen with the previous model relocation results, with particularly high RMS residual S-wave times (Figure 50, Figure 51). The average RMS residual P- and S-wave differential times for this sequence are 0.48 s and 0.90 s, respectively. These high differential times are due to the number of differential times used to relocate these events: 243 P-wave differential times and 330 S-wave differential times, lower than for the other two sequences. The largest event in this sequence, the 2014 La Habra Earthquake, contains the largest RMS residual P- and S-wave differential times, at 0.82 s and 1.53 s, respectively. The GrowClust algorithm used 101 P-wave differential times and 278 S-wave differential times to relocate this event. Compared to the other major sequences in the area, the number of differential times used to relocate these events is low.

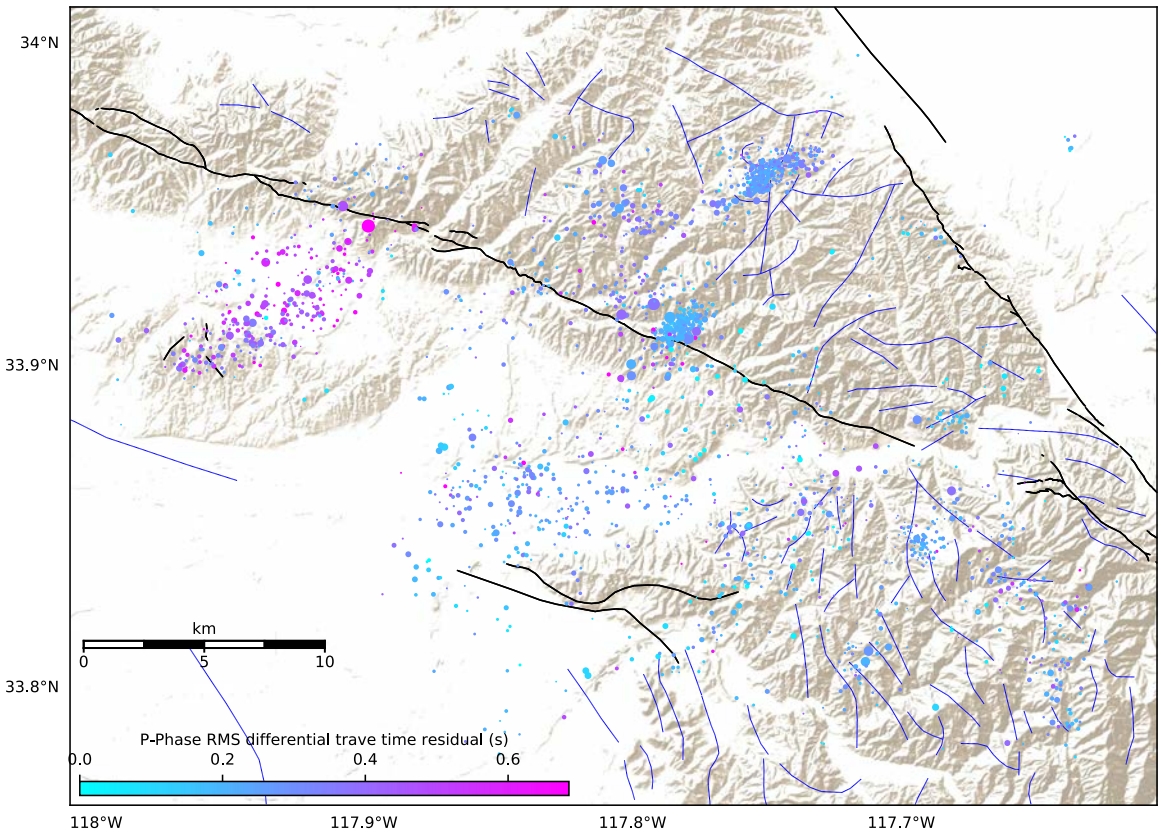

Figure 50: Map of relocated events color coded by their respective RMS residual P-wave differential time from the LA Basin velocity model relocation results under a 0.2 RMS differential travel time residual parameter.

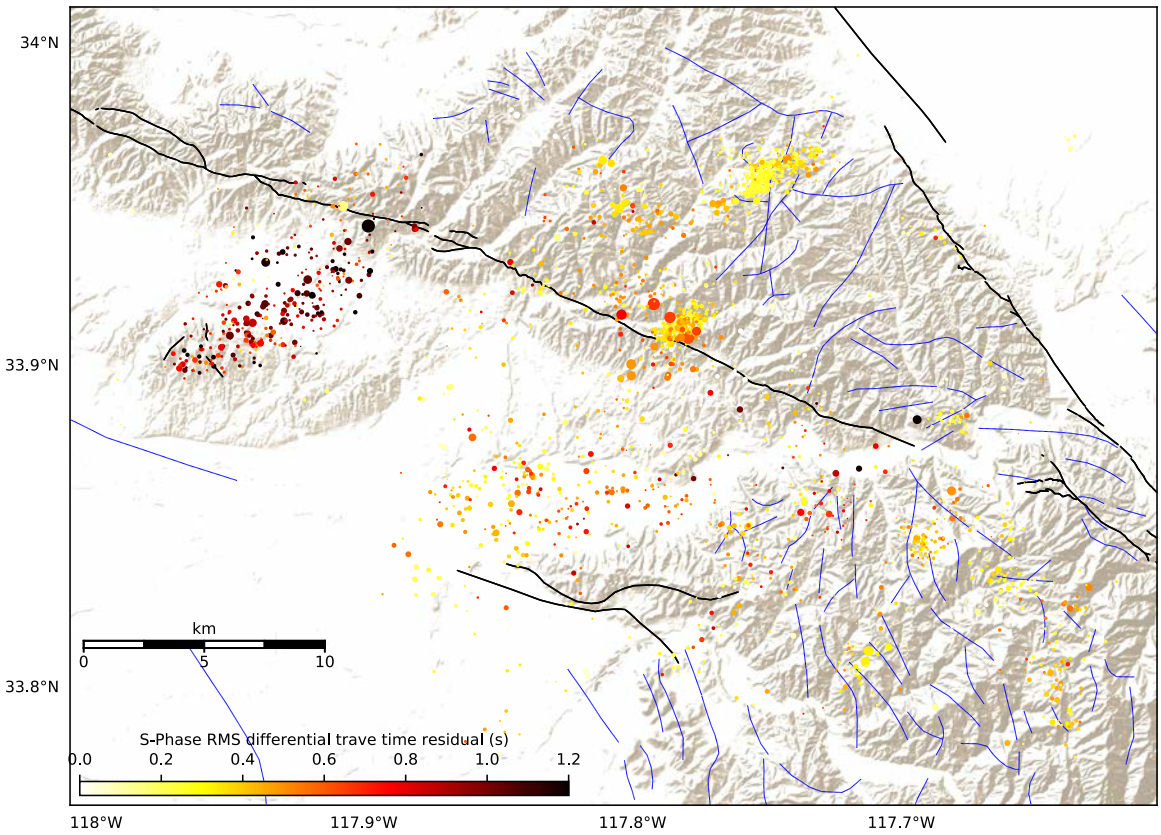

Figure 51: Map of relocated events color coded by their respective RMS residual S-wave differential time from the LA Basin velocity model relocation results under a 0.2 RMS differential travel time residual parameter.

The LA Basin velocity model relocation results possess the highest horizontal location errors of the three relocation results with a 0.2 RMS differential travel time residual (Figure 52). The average horizontal error for these results is 0.832 km. The majority of the events have a horizontal error between 0.360 km and 1.305 km. Despite the high horizontal errors, the vertical errors for these relocation results are the lowest of the three relocation results with a 0.2 RMS differential travel time residual. The average vertical error for these results is 0.742 km (Figure 52). The majority of the events have a vertical error between 0.328 and 1.155 km.

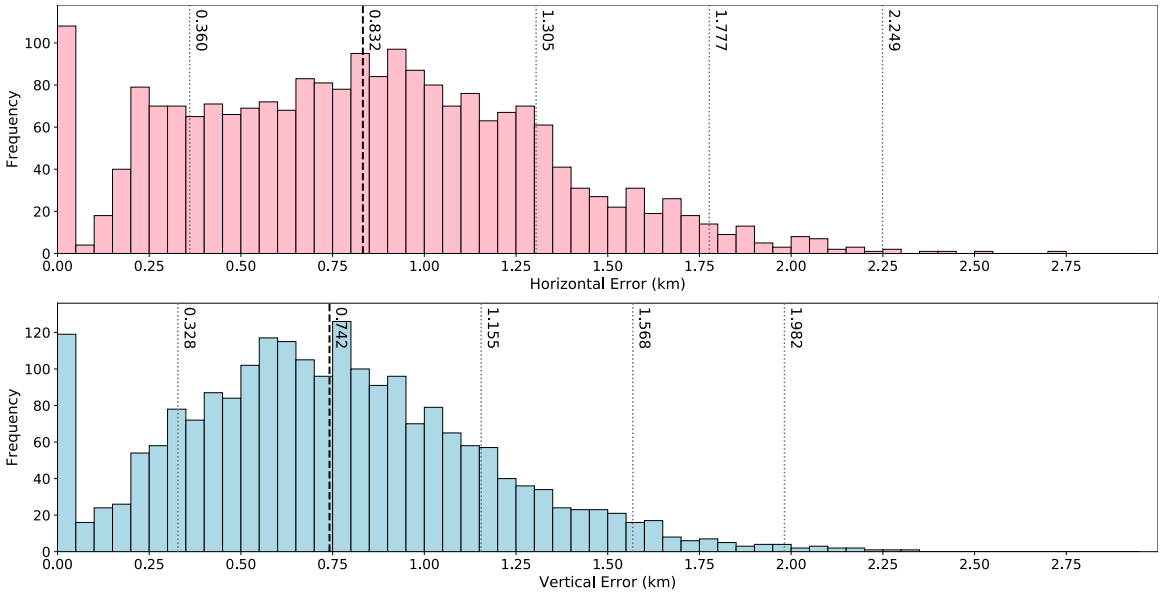

Figure 52: Histograms of the horizontal and vertical location errors for LA Basin velocity model relocation results under a 0.2 RMS differential travel time residual parameter.

Additionally, the horizontal error associated with this event is also considerably higher than the remainder of the Yorba Linda Sequence (Figure 53). This higher error is correlated with the higher RMS residual P- and S-wave differential times. It may also be contributed to what was discussed previously in terms of the low number of P- and S-wave differential times used to relocate this event. The vertical error, however, does have a similar value to that of the remainder of the Yorba Linda Sequence (Figure 54). Similarly The large amount of differential times used to relocate this event contributes to the low horizontal and vertical errors (Figure 53, Figure 54). Similarly to what is seen before, the horizontal error is surprisingly low compared to the remainder of the sequence (Figure 53). Unlike the IASP91 model relocation results, the amount P-wave and S-wave differential times used to relocate this event were 101 and 278, respectively. The high number of differential times used to relocate this event could contribute to the low horizontal error.

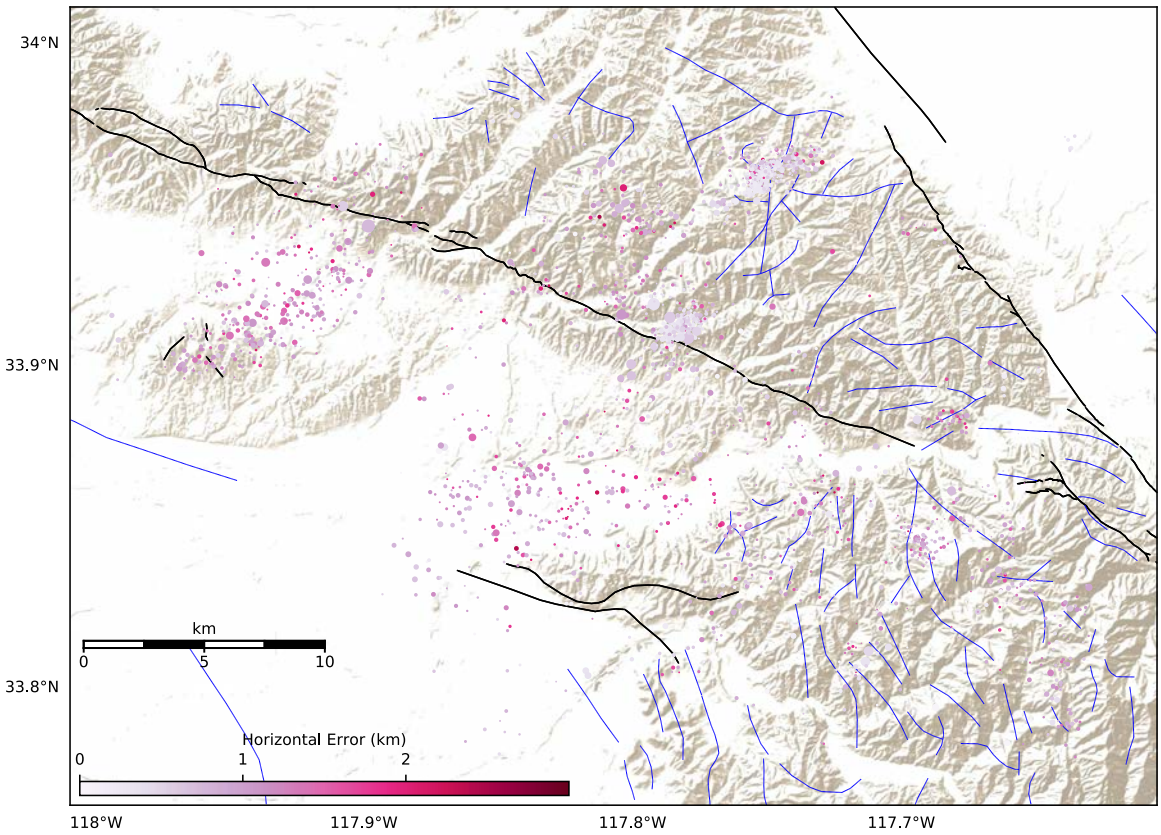

Figure 53: Map of the horizontal errors for of each relocated event using the LA Basin velocity model with a 0.2 RMS differential travel time residual parameter.

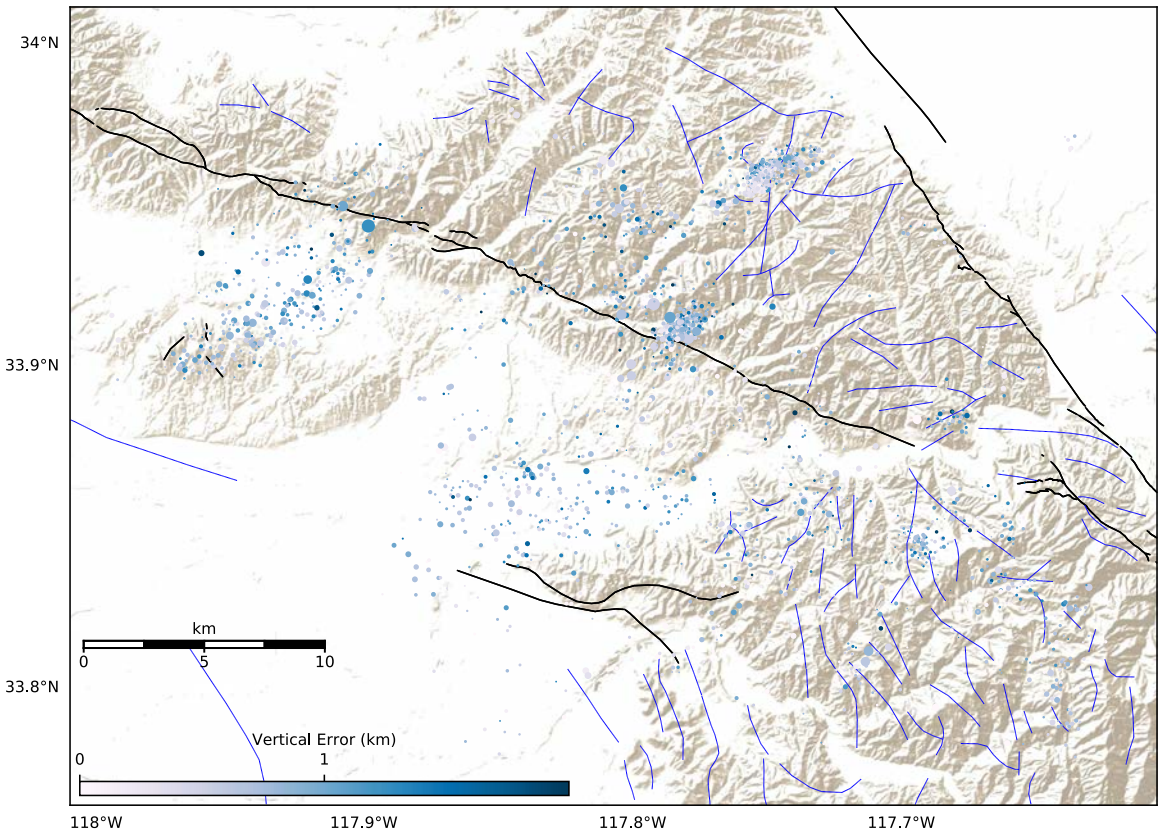

Figure 54: Map of the vertical errors associated with the relocation of events using the LA Basin velocity model with a 0.2 RMS differential travel time residual.

3.1.4 Yorba Linda Sequence Relocation Results for all Velocity Models

Relocations of the Yorba Linda Sequence for the various velocity models have differing results, while successfully relocating the same large events. The IASP91 velocity model relocated 294 events, the smoothed southern California velocity model relocated 290 events, and the LA Basin velocity model relocated 310 events (Figure 55). Despite these small differences in the number of relocated events for each velocity model, each of the resulting relocations has consolidated the Yorba Linda Sequence into a tighter cluster straddling the trace of the Whittier Fault. Two of the relocation results indicate that this sequence crosses the Whittier Fault along a northeast-southwest transect, oriented at approximately 75°from the Whittier Fault trace, with the exception of the smoothed southern California model relocation results (Figure 55-ii). This orientation would

indicate that the potential fault trace associated with these events would be a strike slip fault conjugate to the Whittier Fault. These relocation results suggest a fault structure crossing the Whittier Fault. This type of faulting is abundant throughout southern California, including the 2019 Ridgecrest Earthquake Sequence and areas within the Superstition Hills. Because each of the relocations of the Yorba Linda Sequence have become more consolidated around a feature close to the Whittier Fault and its extent has shortened overall, this would cast doubt into the presence of a single through-going fault connecting the Chino Hills and Yorba Linda Sequences.

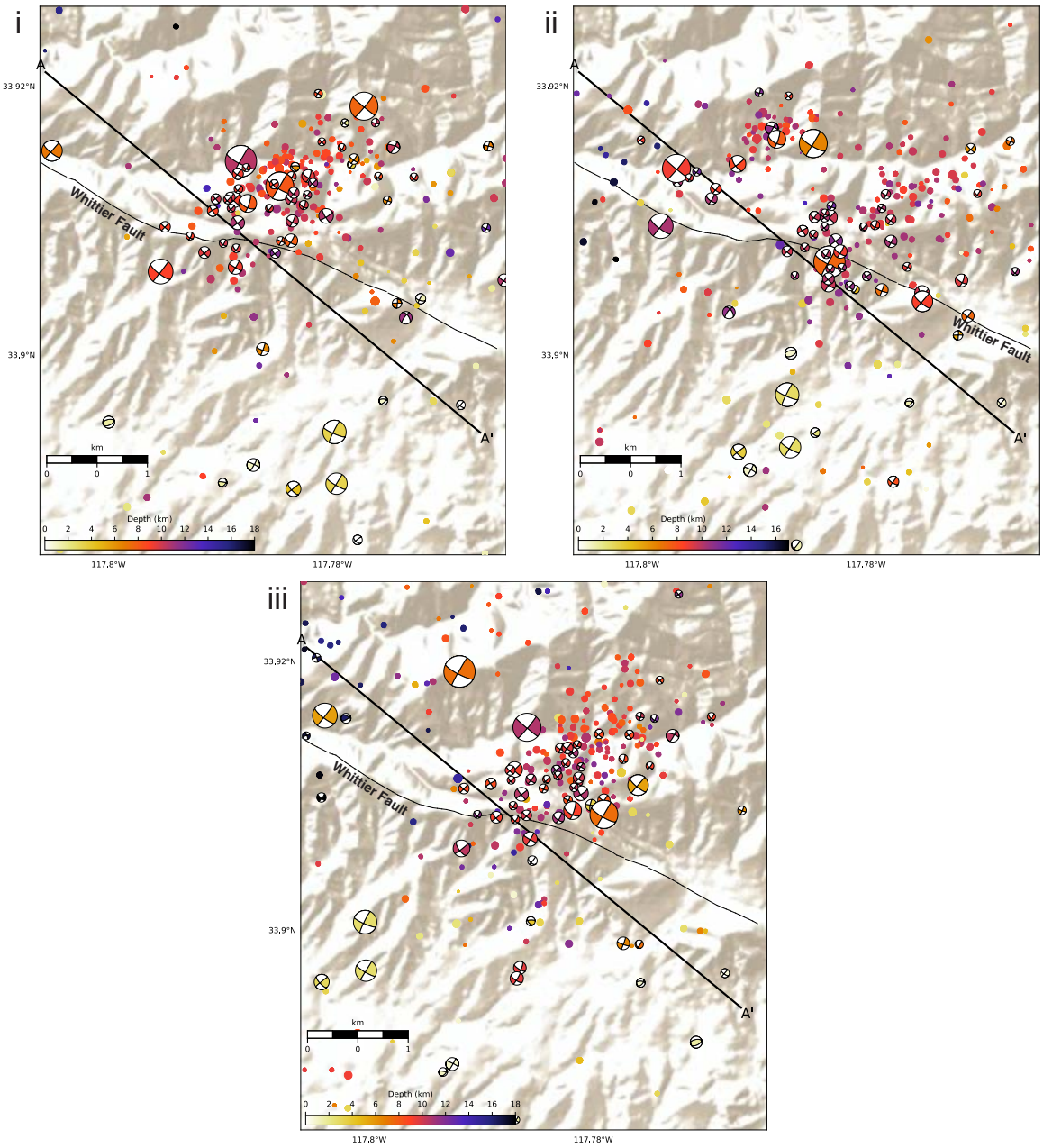

Figure 55: Maps of the relocations of the Yorba Linda Sequence using a 0.2 RMS differential travel time residual and the three different velocity models. Relocated events with available mechanisms and a magnitude greater than 2.0 are plotted as focal mechanisms. These focal mechanisms are plotted in their relocated location, but were calculated at their original location. Focal mechanism solutions from Yang et al. (2012). Figure 55-i shows the relocation results using the IASP91 velocity model. Figure 55-ii displays the relocation results using the smoothed southern California velocity model. Figure 55-iii are the relocation results from the LA Basin velocity model.

There are considerable differences between each of these results for the Yorba Linda Sequence. The quality of these relocations are discussed later in the section. For the

IASP91 velocity model, events have become consolidated within a singular trend that transects the Whittier Fault. Many of the focal mechanisms agree with the orientation of this trend (Figure 55-i). In contrast, the smoothed southern California velocity model relocations for the Yorba Linda Sequence produced two separate trends of looser consolidation than that of the IASP91 model relocations (Figure 55-ii). These events at depths also take on a near vertical alignment at a depth of around 10 km along two parallel planes (Figure 56-ii). While these results depict the Yorba Linda Sequence as two separate trends, the cluster analysis reveals that these trends are in fact part of the same cluster (Figure 37). Each of these trends possesses a similar orientation, extending out from the Whittier fault to the northeast. While the majority of the events are contained within the eastern trend, three of the largest events are held within the western trend. These separate clusters are further verified when looking at this sequence at depth (Figure 56-ii). Compared to the IASP91 model relocations, these events do not take on as clear a vertical alignment (Figure 56-ii).

The relocation results for the LA Basin velocity model show similar results to those seen with the IASP91 model, in that they show a single trend of events with a similar orientation (Figure 55-iii). The locations of the larger earthquakes, represented by focal mechanisms, however, are not situated along the trend as was the case for the IASP91 results, with the largest of these events relocated approximately 1 km towards the northeast of the main trend (Figure 55-iii). The remainder of the large earthquakes are located along the edges of the cluster, unlike the relocations of the IASP91 model (Figure 55-iii). The three large shallow events separated from the main sequence as seen in prior relocation results have aligned moderately well with the remainder of the sequence in these results, with a 1 to 2 km break between those and the main sequence (Figure 55-iii). A depth analysis of the LA Basin velocity model relocation results show a tight, near-vertical trend of earthquakes, similar to that is seen in the IASP91 velocity model relocations (Figure 56-iii). These relocations however, have a larger depth range

than that of the IASP91 relocations (Figure 56-iii).

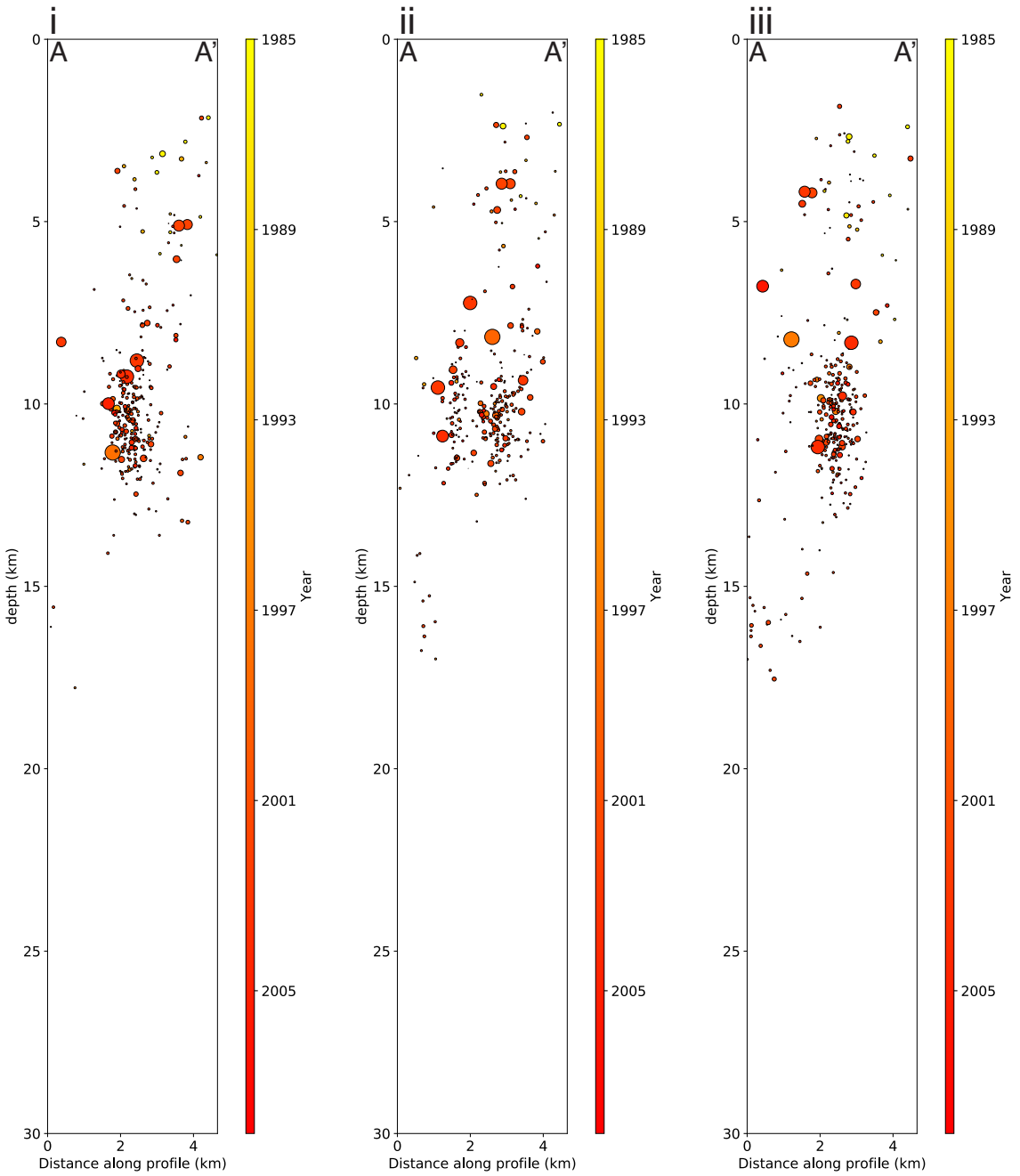

Figure 56: Cross sections illustrating each of the relocations of the Yorba Linda Sequence using a 0.2 RMS differential travel time residual and the three different velocity models. Figure 56-i shows the relocation results using the IASP91 velocity model. Figure 56-ii displays the relocation results using the smoothed southern California velocity model. Figure 56-iii are the relocation results from the LA Basin velocity model.

Each of the relocation results from the three velocity models has similar horizontal and vertical location errors (Figure 57). The smoothed southern California velocity model

relocations have the lowest average horizontal errors, as well as the largest number of events with smaller location errors (Figure 57-iii). However, the spread of these results are the largest, with some errors greater than 2.5 km. The IASP91 velocity model relocation results show similar errors and a slightly larger average error: 50 m difference in the averages. The distribution of smaller errors is larger than that of the smoothed southern California velocity model relocation results, while also having a smaller spread overall (Figure 57-i). The LA Basin velocity model relocations have the smallest spread of horizontal errors, while possessing the largest average errors of the three relocation results (Figure 57-v).

All of the relocation results for each of the models have similar averages and spreads for the vertical errors (Figure 57). The smallest of these errors is the smoothed southern California velocity model relocations (0.736 km), while the largest are the IASP91 velocity model relocation results (0.787 km). Each of the results has a similar number of events with small to average vertical location errors. However, the IASP91 velocity model relocation results also obtain the largest overall spread for the vertical errors, while the smoothed southern California velocity model relocation results have the smallest spread (Figure 57).

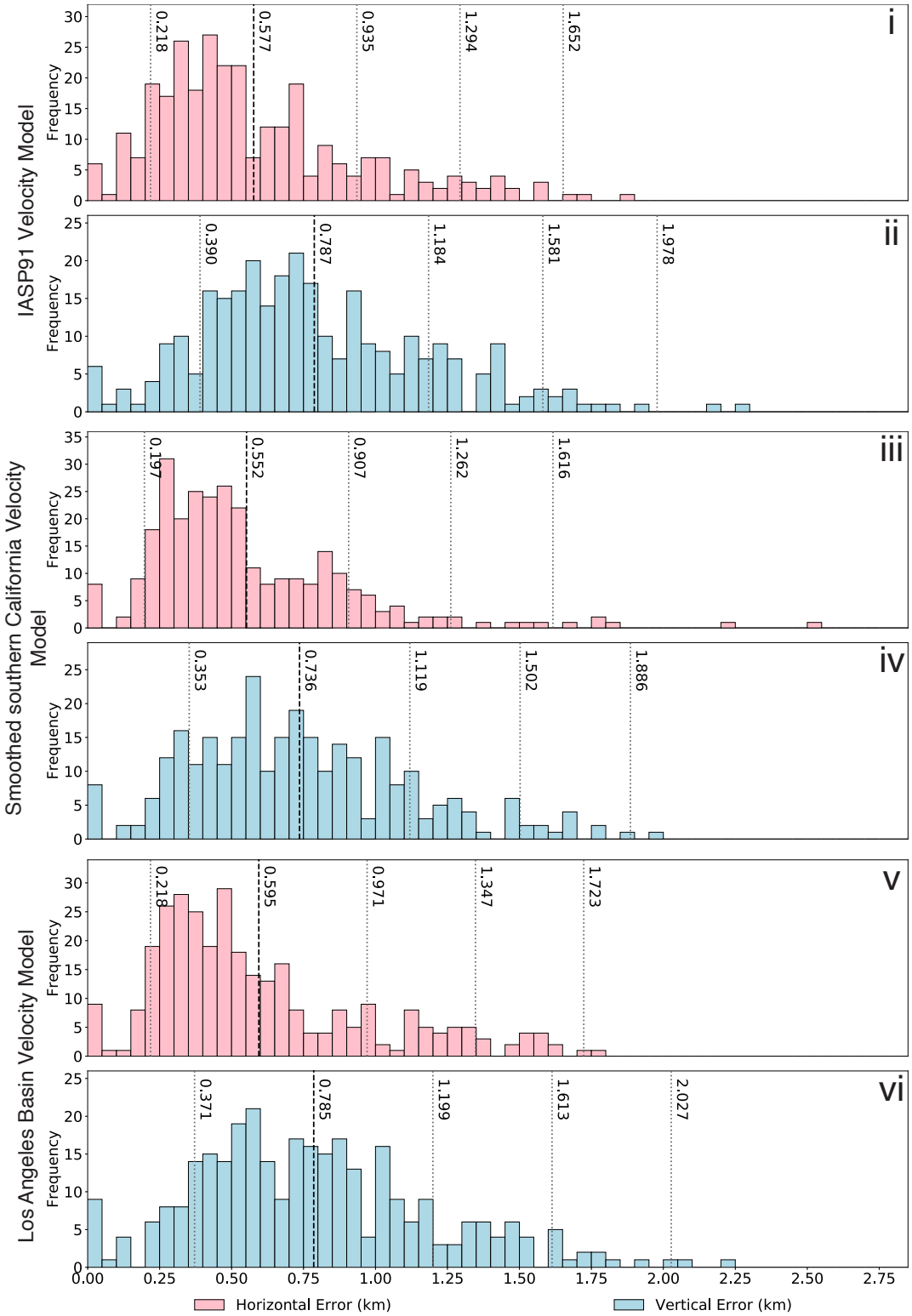

Figure 57: Histograms of the horizontal and vertical errors of the relocations of the Yorba Linda Sequence for each velocity model. The black, dashed line indicates the average location error while the gray, dotted lines denote the standard deviations. Figure 57-i and 57-ii present the errors for the IASP91 velocity model. Figure 57-iii and 57-iv present the errors for the smoothed southern California velocity model. Figure 57-v and 57-vi present the errors for the LA Basin velocity model.

We would expect any of the three velocity models to be a potentially appropriate velocity model to use for the Yorba Linda Sequence. The smoothed southern California velocity model would be fitting to use due to it representing southern California. Conversely, the LA Basin velocity model would also be appropriate based on the sequence's location along the eastern edge.

It is difficult to determine which of these relocated catalogs is the best of the three. The IASP91 model relocations have the best appearance: the relocated events produce a clearly defined near-vertical trend both in map view and cross section view. The IASP91 model relocations, however, have the largest vertical errors of the three model relocations. The smoothed southern California has the smallest location errors for both the horizontal and vertical errors. However, the relocation produced two separate trends instead of one and successfully relocated the smallest number of earthquakes. The IASP91 velocity model relocations produced the largest number of relocated events within the sequence, but the largest horizontal errors of the three. The LA Basin velocity model relocation results possess a singular trend like the IASP91 velocity model relocation results, but appear more scattered. The location of the larger earthquakes are also of particular concern, in that they are located outside the main sequence trend. The errors for the LA Basin velocity model results also possess the highest horizontal errors as well as a larger spread.

Previous studies regarding the Yorba Linda Sequence have postulated that this sequence occurred on a left lateral fault structure conjugate to the Whittier Fault (Chen et al., 2005). Whereas the smoothed southern California velocity model relocation results have the smallest location errors, the presence of two parallel structures as opposed to a single fault structure contrasts with these previous studies (Figure 55-ii) and no corresponding mapped fault traces exist. Our other two relocation results show the sequence at higher angles to the Whittier Fault compared to the former relocation results, which is in agreement with previous studies (Chen et al., 2005). These relocations are

more dispersed, whereas the IASP91 relocation results are more consolidated (Figure 56-i).

3.1.5 Chino Hills Sequence Relocation Results for all Velocity Models

Each of the relocations of the Chino Hills Sequence forms a tight consolidation of events along a northeast-southwest trend that does not follow any known fault traces within the area (Figure 58). Each of the velocity model relocations results in the successful relocation of more than 350 events in this area: 386 earthquakes with the IASP91 velocity model, 375 earthquakes with the smoothed southern California velocity model, and 373 earthquakes using the LA Basin velocity model (Figure 58). The original locations of these events showed three different trends of events (Figure 105). After relocation, these three trends of events were relocated into a single trend. This tight, northeast-southwest oriented series of events may indicate the presence of a previously unknown fault.

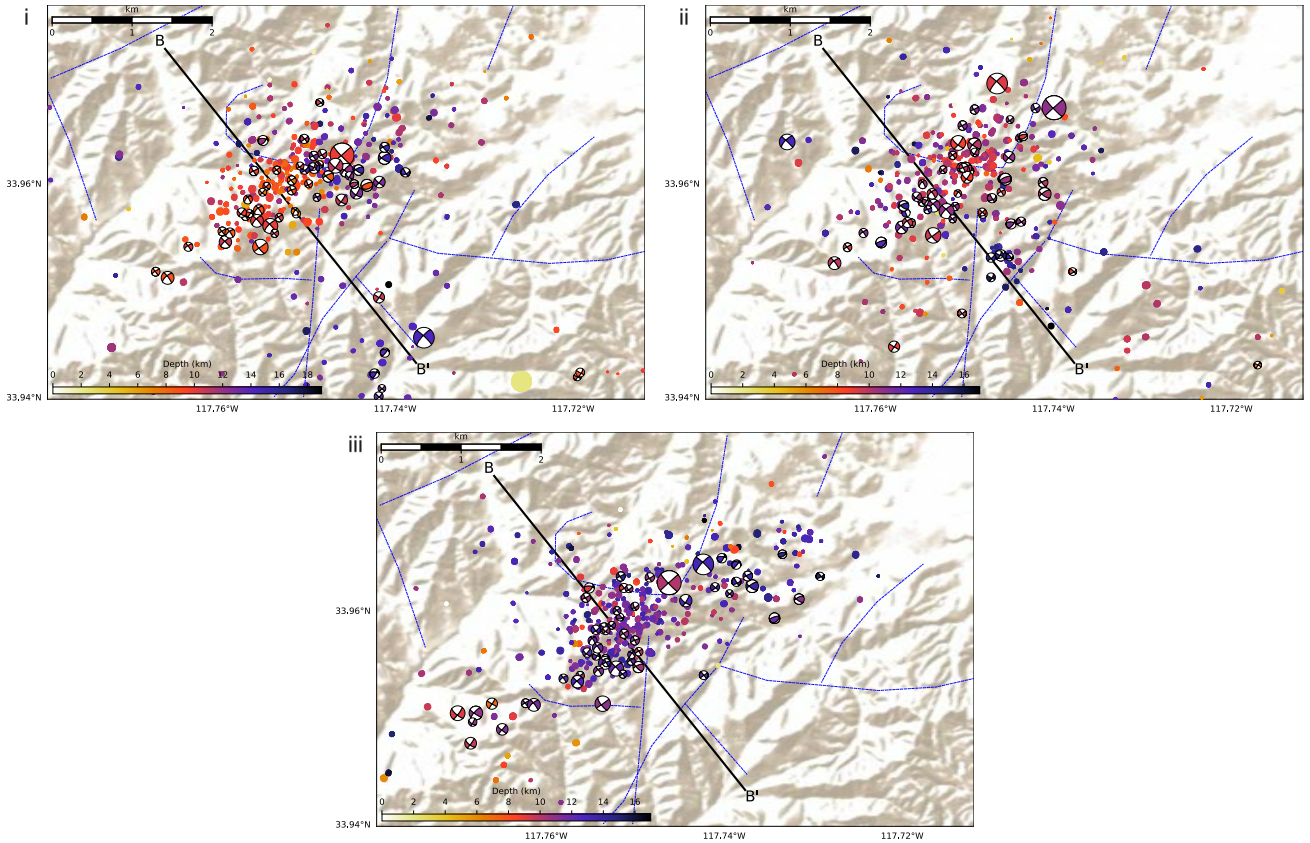

Figure 58: Maps of the relocated Chino Hills Sequence using a 0.2 RMS differential travel time residual and the three different velocity models. Figure 58-i shows the relocation results using the IASP91 velocity model. Figure 58-ii displays the relocation results using the smoothed southern California velocity model. Figure 58-iii are the relocation results from the LA Basin velocity model. Symbols as in figure 55.

Independently, these relocation results do show minor variations. The IASP91 model relocation results show earthquakes along the southwestern segment have shallower depths, increasing in depth towards the northeast (Figure 58-i). The majority of the large earthquakes fall within the sequence itself, apart from a few earthquakes towards the southeast. A large portion of the earthquakes within this series are strike-slip based on their focal mechanisms, with the northwest-southeast nodal plane lining up with the overall trend of the relocated seismicity (Figure 58-i). The few reverse motion earthquakes are noticeably found along the perimeter. The lack of reverse motion events within this cluster, where there were a noticeable number of reverse motion events within the original Chino Hills Sequence as seen in Figure 10, is likely due to the fact that these events were sufficiently sparse that they did not have any correlated pairs, and thus were not successfully relocated. An examination of the events in cross-section further solidifies the interpretation that events making up the Chino Hills Sequence fall along a tightly constrained near vertical feature (Figure 59-i). As previously mentioned, these events occur across a large depth range, with many falling between 10 and 15 km in depth (Figure 59-i).

The relocations produced using the smoothed Southern California velocity model show slight differences compared to the other two relocation results. The event consolidation appears to be less defined compared to the previous model relocations; the event density is less than that of the IASP91 relocated seismicity (Figure 58-ii). The sequence still maintains its characteristic northeast-southwest oriented trend, however. In the case of the smoothed southern California model relocation results, there is no gradual increase in depth from the southwest towards the northeast, rather these events all occur at relatively similar depth (Figure 58-ii). An interesting note is the variation in the location of the deeper large earthquake in the northeast. Within the prior relocation results, this event was initially southeast of the trend, disconnected from the remainder of the cluster. The cross section shows a more consolidated depth distribution compared to the IASP91

model cross section relocations. While it does show these events are situated along what appears to be a near vertical feature, the horizontal distribution of these events is not as tight as those of the other relocation results (Figure 59-ii).

The LA Basin velocity model has produced relocations that have visually the best results. Nearly all of the events within the area have situated themselves within the this main cluster (Figure 58). These results show a tighter clustering than that of the smoothed southern California model relocations and a more extended northeast-southwest trend than the IASP91 model relocations. These relocations also reveal a more consistent depth throughout the entire cluster (Figure 58). The two largest events for all of the relocation results were relocated to the northeast end of the cluster along the same orientation of the overall sequence. The cross section of this sequence reveals a tighter horizontal distribution than that of both of the other relocation results, while possessing a similar depth distribution as the smoothed southern California model relocation results (Figure 59-iii).

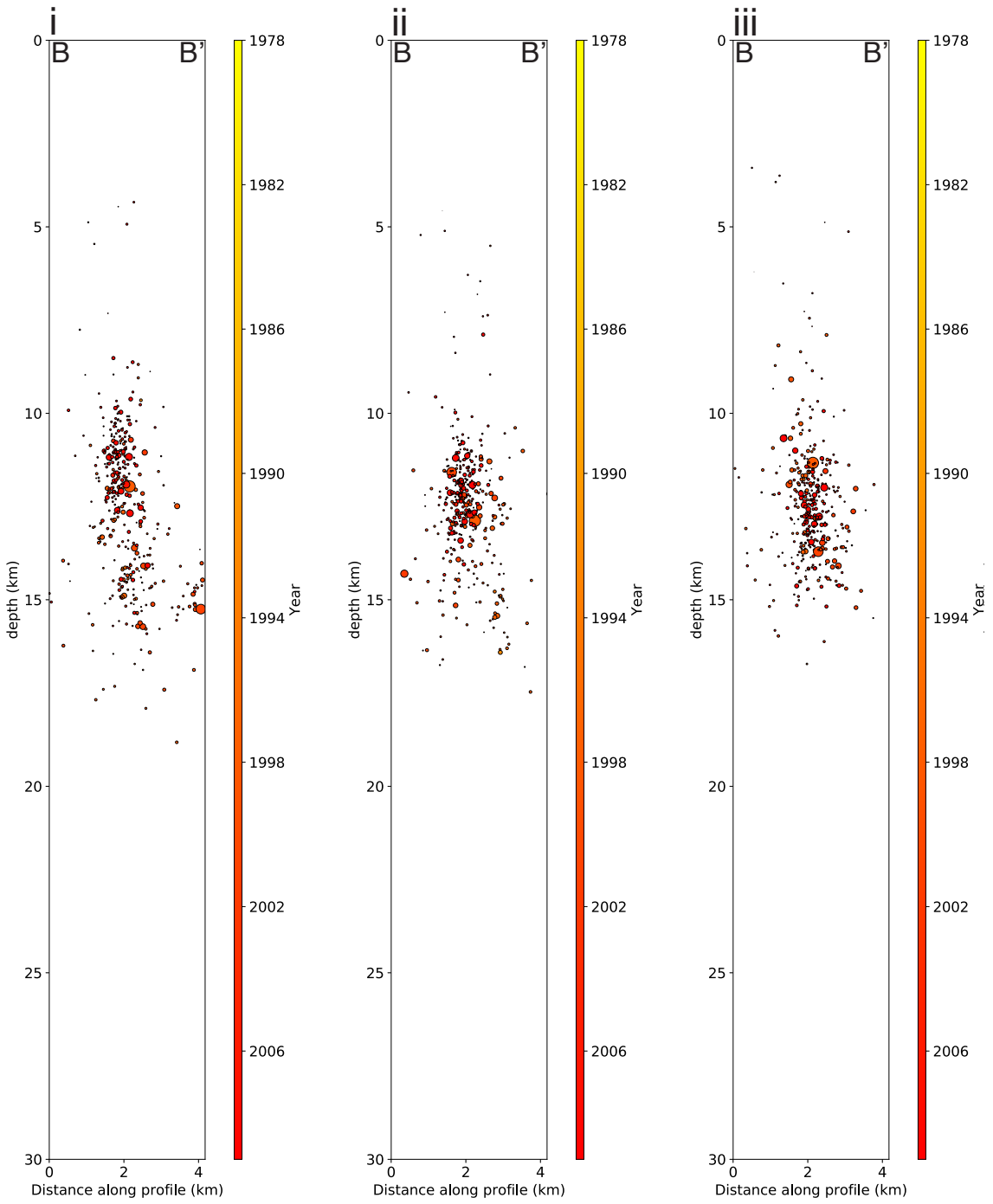

Figure 59: Cross sections illustrating each of the relocations of the Chino Hills Sequence using a 0.2 RMS differential travel time residual and the three different velocity models used. Figure 59-i shows the relocation results using the IASP91 velocity model. Figure 59-ii display the relocation results using the smoothed southern California velocity model. Figure 59-iii are the relocation results from the LA Basin velocity model.

The errors for each of the relocation results have similar characteristics (Figure 60). Each of the models results in large numbers of relocated earthquakes that have small

horizontal errors. Regarding the average horizontal errors for the models, the smoothed southern California velocity model has the lowest errors followed by the relocations based on the IASP91 velocity model. The distribution of each of the horizontal errors is relatively similar, with events based on the IASP91 model possessing the largest errors (Figure 60). The smoothed southern California does possess the most gradual decrease in the amount of events with increasing errors, whereas the results for the LA Basin model has the most drastic variation, with many events with small errors and few earthquakes with larger relocation errors (Figure 60-ii, Figure 60-iii). The relocations for this model also contain the smallest spread of each of the model relocation results (Figure 60-iii).

The vertical errors all have similar average values, ranging from 0.645 km (LA Basin velocity model) to 0.694 km (IASP91 velocity model). The earthquakes relocated using the LA Basin velocity model possesses both the smallest location error and the smallest spread, while the IASP91 model relocation results have both the largest average and spread (Figure 60).

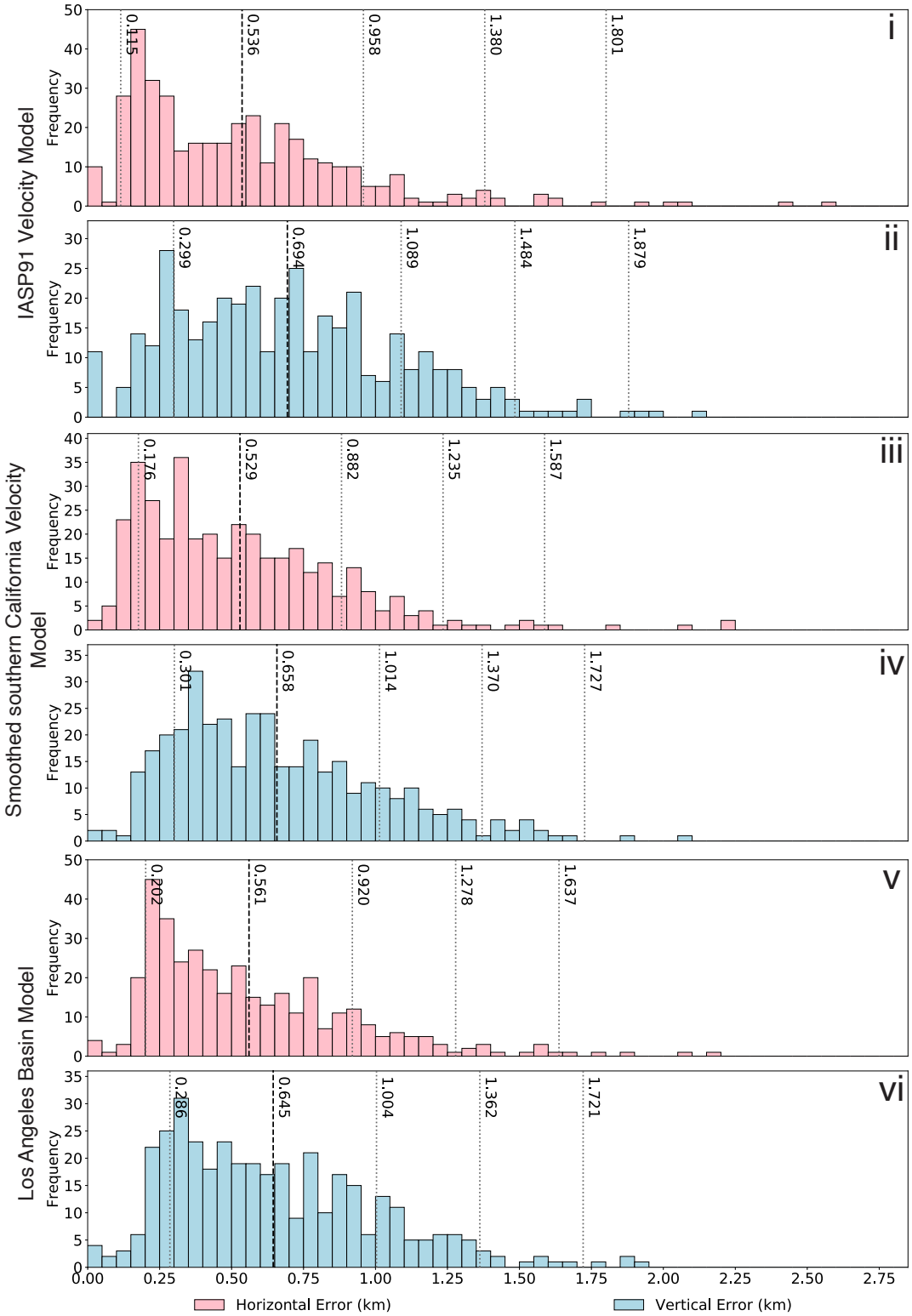

Figure 60: Histograms of the horizontal and vertical errors of the relocations for each velocity model of the Chino Hills Sequence, respectively. The black, dashed line indicates the average location error while the gray, dotted lines denote the standard deviations. Figure 60-i and 60-ii represent the IASP91 velocity model. Figure 60-iii and 60-iv represent the smoothed southern California velocity model. Figure 60-v and 60-vi represent Whittier Narrows velocity model.

Based on its location, the smoothed southern California velocity model should be the optimal velocity model to use to relocate the events within the Chino Hills Sequence. This is in part due to the smoothed southern California velocity model being representative of the entire southern California region (Shao et al., 2012). Similarly to the relocation results for the Yorba Linda Sequence, it is difficult to ascertain which of the relocations has produced the optimal results for the Chino Hills Sequence. The IASP91 model has resulted in the largest number of successfully relocated events, but these events have the largest average vertical errors and the widest horizontal error distribution. The smoothed southern California model again has the smallest location errors of the three, but lacks the tighter event consolidation that the other two relocation results possess. The LA Basin model relocations have the best visual results, with nearly all events relocated to a single northeast-southwest trending cluster that is near-vertical in dip. However, these results possess the largest horizontal error of the three models.

Previous analyses of the Chino Hills Sequence and 2008 Chino Hills Earthquake have contrasting conclusions (Hauksson et al., 2008; Shao et al., 2012). Egill Hauksson's analysis on the 2008 mainshock and aftershocks state that the rupture of the mainshock likely occurred along a left-lateral strike slip fault, while Guangfu Shao's analysis implies that the Chino Hills Earthquake ruptured along the right-lateral Whittier Fault. While none of our relocation results for the Chino Hills Sequence contain the 2008 Chino Hills mainshock in any of the clusters making up the sequence, the orientation of the trend and the focal mechanisms agree with Hauksson's conclusion, in that these events occurred along a left-lateral strike slip fault with a reverse component of motion. The smoothed southern California velocity model relocation results of the Chino Hills Sequence also agree with this conclusion, in that the relocated hypocenter of the 2008 Chino Hills Earthquake lines up with the orientation of the Chino Hills Sequence (Figure 36).

3.1.6 La Habra Sequence Relocation Results for all Velocity Models

The IASP91 model relocation successfully relocated 309 events, including the 2014 La Habra Mainshock, the smoothed southern California model relocation relocated 323 events, and the relocations using LA Basin model encompassed 330 events, including the 2014 La Habra Mainshock. Each of the relocations show a linear trend extending from the Whittier Fault to the Coyote Hills Fault System (Figure 61). For each velocity model, the relocated earthquakes are relatively shallow and loosely consolidated around a single trend. Each of the models shows seismicity that occurs within the Coyote Hills Fault System. Each of the model relocations show both strike-slip and reverse events, indicating that there is a mixture of motion occurring on this fault or motion on several faults. Aside from these similarities, each of the model relocations show different levels of continuity of the trend of the La Habra Sequence, with two of the model relocation results with breaks in the trend. (Figure 61).